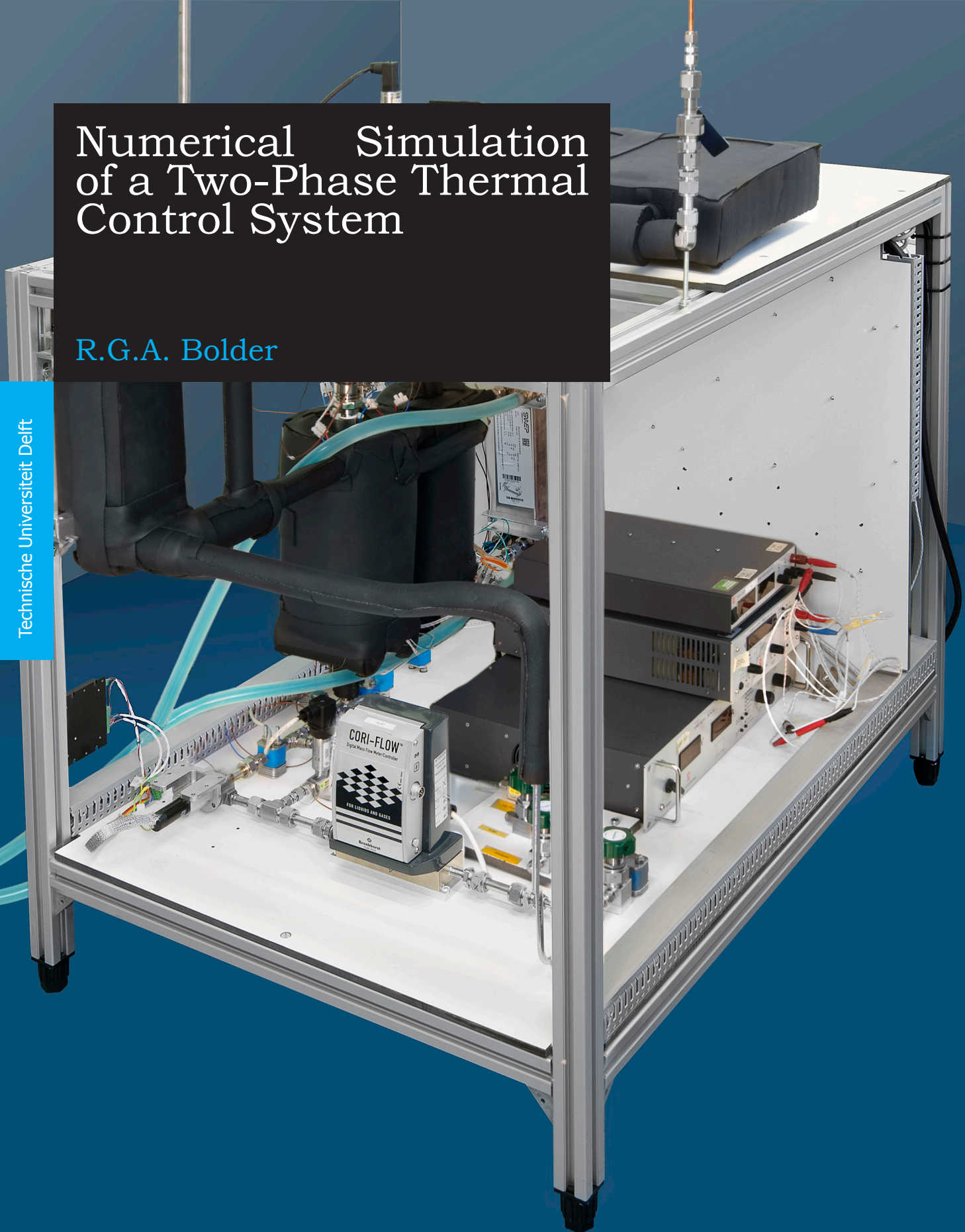


Numerical Simulation of a Two-Phase Thermal Control System

R.G.A. Bolder

Technische Universiteit Delft



Numerical Simulation of a Two-Phase Thermal Control System

by

R.G.A. Bolder

in partial fulfillment of the requirements for the degree of

Master of Science
in Aerospace Engineering

at the Delft University of Technology,
to be defended publicly on Thursday October 5, 2017 at 10:00 AM.

Supervisor:	Dr. A. Cervone,	TU Delft
Thesis committee:	Ir. B. T. C. Zandbergen,	TU Delft
	Dr. Ir. M. Pini,	TU Delft
	Dr. Ir. H. J. van Gerner,	NLR

An electronic version of this thesis is available at <http://repository.tudelft.nl/>.

Abstract

Two-phase thermal control systems are used for payloads that require temperature stability under high and fluctuating heat output. However, the complex interaction between the two phases in a flow makes it hard to predict the performance of such a system. The goal was to develop a numerical model able to predict the transient behaviour of such a system within a 30% error margin. An existing explicit one-dimensional finite-difference simulation was expanded using new correlations from literature. The performance of this model was validated using experimental measurements gathered with the NLR¹ two-phase demonstrator setup. The resulting numerical simulation can predict the transient behaviour of the pressure drop and liquid level in the accumulator with a mean error of 7.7% and 1.3% respectively. The goal therefore has been reached. While room remains for further improvement and validation, this model can significantly shorten the development time of new two-phase systems.

¹Netherlands Aerospace Centre

Summary

Two-phase, pumped loop thermal control systems have several unique capabilities that differentiate them from other thermal control systems. Such a system uses the latent heat of evaporation to store heat, which means that it can support large heat fluxes with relatively small amounts of fluid. Because evaporating liquids maintain a constant temperature, there are no thermal gradients across the interface surface area like many other systems have. It is also able to keep a steady payload temperature with fluctuating heat inputs. The major disadvantage of these systems is that when the heat input changes, it affects the amount of vapour created, resulting in fluctuations in the heat transfer coefficient, pressure and flow speed. This makes it much harder to predict the exact behaviour of the system.

To solve this, the NRL is been developing a numerical simulation program. this explicit one-dimensional finite-difference model is based upon a simplified subset of the one-dimensional Navier-Stokes equations. The original model was built for CO₂ as a working fluid and assumed homogeneous flow throughout the system. The focus of this thesis is on expanding that computer model for broader use, especially using R134a working fluid, with a goal of reaching an accuracy to within a 30% error margin in relation to real-world measurements.

This is achieved by both improving the accuracy of the existing simulation and expanding it to include more factors that can influence the system behaviour. The improvements to the existing model mainly focus on determining the most accurate equations for calculating the frictional pressure drop and heat transfer coefficients. A selection was made containing both unproven recent models and older well-established equations for these parameters during the literature study. The accuracy of these correlations is then determined empirically by comparing the results of the full simulation to measurement data gathered using a real-world experimental setup at the NRL.

The largest expansion of the model is the implementation of void fraction correlations, which can be used to calculate non-homogeneous flows. This is expected to increase the simulation accuracy for fluids such as R134a. Further expansions include adding calculation of the gravitational and momentum pressure effects as well as a lot of minor improvements and additions to the code for an easier workflow and better control of the settings.

Concurrently, the NRL Two-Phase Demonstrator setup was calibrated and prepared to produce the reference measurements. This included measuring the geometry and recreating it numerically, wrapping the setup in thermal insulation, calibrating a sensor and adjusting some of the control software.

During the verification phase, a number of tests were run on both the numerical model and the experimental setup. The results were analysed to check for any unexpected behaviour and errors in the preparation. Two errors were found in the simulation. The first of which was a reversal in the flow direction that happened under certain circumstances. The model assumes a constant flow direction and negative values for the velocity parameter will lead to a cascade of errors. It was not expected for the flow to change direction and this effect did only happen for a select number of correlations, but the exact cause of this effect could not be found. Solving the error by enabling the model to deal with negative velocity values would require a significant rewrite of major parts of the model. Instead, it was decided to exclude the correlations that cause this effect.

The second error found was in the adaptation of the state equations to include non-homogeneous flow models. This produced unexpected results when using the void fraction correlations. Finding the source of the error took some time. The results of the homogeneous-flow version were unaffected and therefore the non-homogeneous flow options were initially excluded and the validation procedure was started. Once the source of the error was found, it was easily fixed and the void fraction correlations were tested at a later stage of the validation process.

Once both the model and the setup were verified the validation process was started. This included running the simulation using every possible combination of the implemented correlations and checking their results against two baseline tests performed on the demonstrator setup. The accuracy of each configuration was checked against a series of parameters. Once the void fraction models were verified, these were tested as well, but without success. Another error was found that traced back to a fault

in the underlying theory used to implement non-homogeneous flow elements in the equations of state which were originally based upon the homogeneous flow assumption.

The configuration that produced the most accurate results overall was selected and underwent further testing for a broader envelope of test conditions. These results were compared to an equally extended set of experimental measurements to determine the accuracy of the final numerical model. The selected equations are: Friedel [1] for the two-phase fictional pressure drop, the Gungor-Winterton [2] correlation for two-phase evaporating flow heat transfer coefficient and maintaining the homogeneous flow assumption instead of the newly implemented non-homogeneous void fraction models.

The mean absolute percentage error of this configuration was 7.71% for the pressure drop and only 1.34% for the accumulator level. This falls well within the 30% error margin set by the first research question. This means that the model is working well and can be verified, albeit with a few limitations. Most important of these are that the non-homogeneous void fraction functions cannot be used and should either be removed or replaced in further development and that under certain conditions, reversal of the flow direction can still occur, which will break the simulation. Finally, further testing is required to determine the full validity range of the numeric model.

Contents

Abstract	iii
Summary	v
Nomenclature	ix
List of Symbols	xii
1 Introduction	1
2 Literature study	3
2.1 Basics of two-phase thermal control systems	3
2.1.1 Typical layout of a two-phase system	3
2.1.2 Evaporator and condenser	4
2.1.3 Pump and flow meter	4
2.1.4 Heat exchanger	4
2.1.5 Accumulator	5
2.1.6 Typical responses in a two-phase system	5
2.2 Pressure drop	6
2.2.1 Minor pressure loss	6
2.2.2 Frictional pressure loss	6
2.3 Heat transfer coefficient	8
2.4 Void fractions	8
2.5 Literature study conclusions	9
3 Research setup	11
3.1 Research Objective	11
3.2 Research Questions	11
3.3 Research Plan	12
3.4 Two-Phase Demonstrator setup	12
3.5 Numerical model	14
3.5.1 Structure	14
3.5.2 Mathematical basis	14
3.5.3 Assumptions	16
3.6 conclusion	17
4 Numerical implementation of the demonstrator geometry	19
4.1 Tubing	19
4.2 Special components	19
4.3 Simplified geometry	19
5 Numerical model adaptation	23
5.1 Local Pressure	23
5.1.1 Minor pressure loss	23
5.1.2 Pressure drop in restrictions	23
5.1.3 Frictional pressure drop	24
5.1.4 Gravitational and momentum pressure change	26
5.2 Heat Transfer Coefficient	26
5.2.1 Heat transfer in Evaporators	26
5.2.2 Heat transfer in Condenser and Heat exchanger	27
5.3 Void fraction	27
5.3.1 Implementation	28
5.3.2 Issues	28

6	Experimental setup	31
6.1	Hardware adjustments	31
6.2	Software adjustments	32
6.3	Calibration.	32
6.4	Test plan and procedures	35
7	Testing and verification	37
7.1	Accumulator temperatures	37
7.2	Negative flow velocity	38
7.2.1	Implications	39
7.2.2	Solution	39
7.2.3	Potential cause	39
7.3	Void fraction.	40
7.3.1	Error found	41
7.4	Heat transfer coefficient.	41
7.5	Conservation of mass	42
8	Model performance and validation	45
8.1	Method of validation	45
8.2	Pressure drop correlation	46
8.2.1	Total pressure drop	46
8.2.2	Local pressures	47
8.2.3	Pressure drop over evaporators	47
8.3	Accumulator liquid level.	50
8.4	Temperature.	52
8.5	Void fraction.	52
8.5.1	Accumulator liquid level.	53
8.5.2	Pressure drop	54
8.6	Final Correlation selection	54
9	Conclusions	57
10	Recommendations	59
A	Hardware used in demonstrator	61
A.1	Evaporator.	61
A.2	SWEP heat exchangers	62
A.3	Accumulators	63
B	Implemented correlations	65
B.1	Pressure drop	65
B.2	Heat transfer coefficient.	67
B.3	Void fraction.	67
C	Numerical code	69
C.1	CalcTimeLoop structure.	69
C.2	Frictional pressure drop calculations	70
D	Sensitivity analysis	75
D.1	Pipe roughness	75
D.2	Pipe diameter	75
E	Final correlation validation	77
	Bibliography	81

Nomenclature

Accu	Accumulator
HCA	Heat Controlled Accumulator
HTC	Heat Transfer Coefficient
MAPE	Mean Absolute Percentage Error
NIST	National Institute of Standards and Technology
NLR	Nederlands Lucht- en Ruimtevaartcentrum (Netherlands Aerospace Centre)
PCA	Pressure Controlled Accumulator
REFPROP	Reference Fluid Thermodynamic and Transport Properties Database
RPM	Revolutions Per Minute

List of Symbols

Symbol	Explanation	Unit
<i>Latin</i>		
A	Area	[m ²]
Bd	Bond number (same as Eötvös number)	[-]
Bo	Boiling number	[-]
C_0	Distribution parameter	[-]
c_{CFL}	Courant-Friedrich-Lewy parameter	[-]
c_l	Latent heat	[J/kg]
c_p	Specific heat	[J/(kg·K)]
d	Channel/tube (hydraulic) diameter	[m]
Eo	Eötvös number (same as Bond number)	[-]
Fa	Facilitation number	[-]
Fr	Froude number	[-]
f	Darcy-Weisbach friction factor	[-]
G	Mass flux	[kg/(m ² ·s)]
g	Gravitational acceleration	[m/s ²]
H	Enthalpy	[J]
h	Heat transfer coefficient	[W/(m ² ·K)]
h_{lat}	Latent heat of evaporation	[J/kg]
j	Volumetric flux	[m ³ /(m ² ·s)]
K_p	Control stiffness	[W/K]
k	Thermal conductivity	[W/(m·K)]
L	Length	[m]
M	Molecular mass	[g/mol]
m	Mass flow	[kg/s]
M_i	Measured value	any
Nu	Nusselt number	[-]
P	Power	[W]
P_F	Wetted perimeter	[-]
P_H	Heated perimeter	[-]
Pr	Prandtl number	[-]
p	Pressure	[Pa]
p_r	Reduced pressure	[-]
Q	Volume flow	[m ³ /s]
q''	Heat flux	[W/m ²]
Re	Reynolds number	[-]
S_i	Simulated value	any
Su	Suratman number	[-]
s	Distance	[m]
t	Time	[s]
u	Fluid velocity	[m/s]
V	Volume	[m ³]
We	Weber number	[-]
X	Martinelli factor	[-]
x	Vapour quality (vapour mass fraction)	[kg _g /kg _{tot}]

Symbol	Explanation	Unit
<i>Greek</i>		
ε	Void fraction (vapour volume fraction)	$[\text{m}_g^3/\text{m}_{\text{tot}}^3]$
ζ	Smoothing factor	[-]
θ	Inclination angle	[rad]
μ	Dynamic viscosity	$[\text{kg}/(\text{m}\cdot\text{s})]$
$\mu_{l,f}$	Liquid viscosity at mean fluid temperature	$[\text{kg}/(\text{m}\cdot\text{s})]$
$\mu_{l,w}$	Liquid viscosity at inner wall temperature	$[\text{kg}/(\text{m}\cdot\text{s})]$
ξ	Minor pressure loss factor	[-]
ρ	Density	$[\text{kg}/\text{m}^3]$
σ	Surface tension	$[\text{N}/\text{m}]$
τ_i	Integration time	[s]
ϕ	Two-phase friction multiplier	[-]
<i>Subscripts</i>		
a	Acceleration	
atm	Atmospheric (pressure)	
c	Cross-sectional (area)	
c	Corrector	
cb	Convection boiling	
di	Dryout incipience	
f	Friction	
g	Gas (Vapour)	
go	Gas-only (Assuming that the complete mass flow is in gaseous form; $x = 1$)	
h	Hydrostatic	
i	Current element	
l	Liquid	
lo	Liquid-only (Assuming that the complete mass flow is in liquid form; $x = 0$)	
n	Current timestep	
nb	Nucleate boiling	
p	Predictor	
s	Superficial	
s	Surface (area)	
tot	Total (liquid + vapour)	

1

Introduction

Thermal control systems are used to keep the temperature of an environment or the equipment within it between certain boundaries. This can be everything from the heating and cooling systems in a large office building to the fans in a computer. While thermal control systems in general encompass both heating and cooling equipment, heating an object is usually relatively simple, while removing heat from an environment is often much harder to accomplish (due to the second law of thermodynamics). Therefore, the emphasis in research on thermal control systems is usually on the cooling aspect.

While heat can quite easily be 'generated' using other types of energy such as electricity, exothermic reactions (such as fire) or mechanical work, 'coldness' is much more difficult (again, due to the second law of thermodynamics). Therefore, most cooling systems work by transporting heat away to a place where it can be dissipated more easily.

There are many types of heat transport systems in existence and under development that are each able to cater to a specific set of requirements, such as the temperature range, the amount of heat to be transported, the distance over which it has to be transported, and the temperature stability. One such system is the 'two-phase pumped-loop' thermal control system. This is a relatively complex type of system but it has several characteristics that make it ideal for some specific implementations.

In two-phase pumped loop thermal control systems, the latent heat of a fluid (the amount of energy required to evaporate a given mass of liquid) is used as a method of absorbing heat. This way, a large amount of heat can be stored in a relatively small amount of fluid, which can be transported over long distances. Another advantage is that evaporation happens at a constant temperature, so the fluid temperature remains constant independent of the amount of heat that is added, meaning that there are no thermal gradients along the cooling surface and it limits temperature fluctuations when the amount of heat input is changed. This makes it ideal for applications with high heat fluxes across small surface areas or systems that require very stable conditions (both minimum vibrations and temperature changes), as lower required mass flows also mean less pump vibrations [3].

While there are many possible applications for such a system, one important opportunity lies in the space industry. Satellite designs are becoming more and more complex, with a lot of steps being taken both in miniaturisation of components and designing more sensitive instruments. Miniaturisation means that components will be packed closer together, leading to higher heat fluxes and smaller interface areas. While more sensitive instruments will require an increase in the temperature stability and limits on the induced vibrations. A two-phase system provides solutions to both of these challenges.

The disadvantage of using two-phase flows is that its behaviour is much harder to predict. Not only does each phase interact with the channel walls in a different way, the phases will also interact with each other, often in very complex ways. This causes the amount of relevant parameters to increase significantly, making it much harder to accurately model its behaviour and the performance of such a system as a whole.

The NLR is working on the development of these systems for both the space sector and other industries. To help the design of a product for a client, a numerical simulation model was built. Such a model makes it faster, easier and cheaper to evaluate the initial design and sizing of loops or to work out innovations. The goal of this thesis is to expand the existing code in order to create a general all-encompassing numerical model for predicting the behaviour of two-phase pumped loop thermal

control systems. This is part of a broader in-house project within the NLR focusing on expanding their knowledge in and experience with this type of system.

In chapter 2, a summary of the literature study [4] will be presented. Followed by chapter 3, which explains the research setup and the main resources that will be used. Chapter 4 describes how the geometry of the experimental setup was determined and implemented numerically. The process of adjusting and expanding the numerical model, using the conclusions of the literature study, is recounted in chapter 5. Chapter 6 explains the preparation and calibration of the experimental setup for testing.

The verification and validation of the model is described in chapters 7 and 8 respectively. The first one explains the tests performed to find and solve any issues in order to verify that the model works as expected, while the numerical simulation is validated by comparing its results to the real-life test data obtained using the experimental setup in the latter. Following this, the conclusions on the performance and validity of the model will be presented in chapter 9. Finally, any recommendations for further study will be presented in chapter 10.

2

Literature study

As mentioned in the introduction, the goal of this thesis is to create a general all-encompassing numerical model for predicting the behaviour of two-phase pumped loop thermal control systems. This will be done by improving and expanding an existing computer program developed at the NLR. After discussion with the engineers at the NLR, the most inaccurate parts of the model are probably the equations that calculate the parameters in the two-phase sections of the flow. Based on that information, an extensive literature study was performed. The research questions for this literature review are presented below.

1. Which correlations for two-phase void fraction, pressure drop and heat transfer coefficient are relevant for developing and improving the numerical model at NLR?
2. What is the difference between the correlations in terms of applicability and results for the conditions encountered in the demonstrator setup?
3. Which of the evaluated correlations is best suited for implementation in the numerical model, both for the best general applicability and for use with R134a in the Demonstrator?

The results of this study have been published as a separate report [4]. In this chapter, a summary of that report will be given and the most important results discussed. This starts with a basic overview of what a two-phase control system is and how its major components work. Then, the equations found for each of the parameters named in the first research question are discussed in sections 2.2, 2.3 and 2.4. Finally, the conclusions of the literature study report will be summarised in section 2.5.

2.1. Basics of two-phase thermal control systems

In this section, a general overview of the functioning of a two-phase system and its most important elements is given. This begins with a basic overview of all elements in section 2.1.1. Then, some further explanation of the most important elements is given. The two most basic elements of the loop, the evaporator and the condenser in 2.1.2. Next the function of the pump and flow meter are discussed in 2.1.3. The heat exchangers are discussed in 2.1.4. The last component to be discussed is the accumulator in 2.1.5. Finally, a few 'responses' of such a two-phase system are discussed in 2.1.6 to get a better insight into the typical effects of certain operating conditions or design choices. For a reference to the different elements and how they are connected, see figure 2.1.

2.1.1. Typical layout of a two-phase system

Figure 2.1 shows the basic elements that make up a typical two-phase pumped loop thermal control system. The 'payload' or object that needs to be cooled would be connected to the evaporator, on the left side of this drawing. Here the heat enters the system and it is rejected again in the condenser on the opposite side. The pump provides circulation (clockwise in this diagram). The heat exchanger pre-heats the flow to improve the evaporator performance and the accumulator is used to control the saturation temperature (basically the set-point temperature of the cooling system).

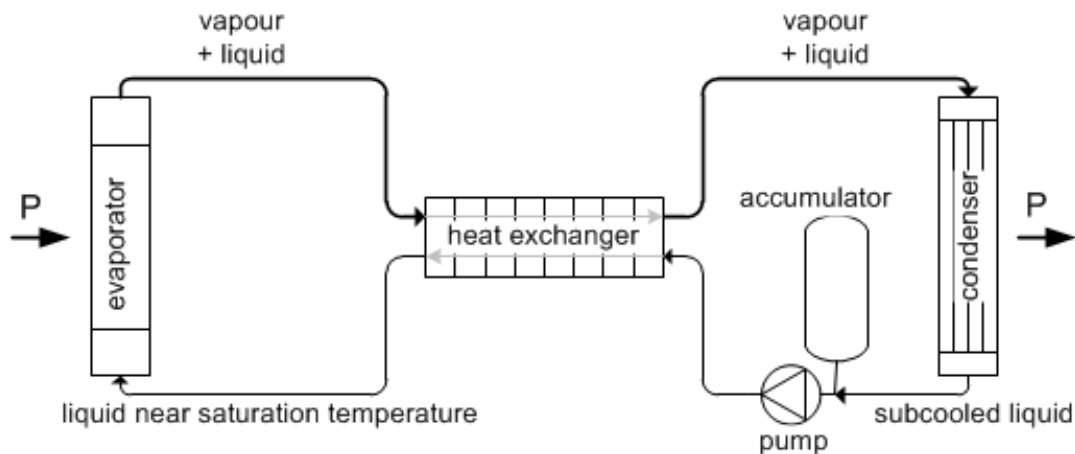


Figure 2.1: Schematic drawing of a basic two-phase loop [5].

2.1.2. Evaporator and condenser

The evaporator is the element where heat is introduced in the system, converting the liquid refrigerant into a two-phase flow. In most cases it is connected directly to the payload or heat source of the instrument it needs to cool. Since the ability to maintain a very accurate and stable temperature is usually the reason that a two-phase system is chosen, this element is the most important 'design driver' of the system.

The condenser is the system element where the heat is rejected, converting the fluid back to single-phase (subcooled) liquid. The heat can be rejected directly to the environment using a radiator, as is usually employed on spacecraft. Or the heat can be transferred to a secondary cooling system such as a single-phase water loop, as is often applied in larger Earth-based systems. This secondary system will be larger and less precise, but the exact condenser temperature does generally not matter for the total system performance.

2.1.3. Pump and flow meter

The pump is used to circulate the fluid through the system. In simple systems, the pump is set to a constant speed in Revolutions Per Minute (RPM). In that case the volume flow is determined purely by the pump specifications and the pressure difference between the pump inlet and outlet. Larger pressure differences will give lower volume flow, as more energy is used to raise the pressure. More advanced systems use a flow meter at the outlet of the pump to measure the flow and control the pump RPM to keep the volume flow constant, as is the case in the demonstrator loop which will be discussed in chapter 3.4.

One major limitation of a pump in two-phase systems, is that the fluid flowing through the pump must be *subcooled* (single-phase) liquid. If the liquid would be at saturation temperature or even partially evaporated, cavitation would occur in the pump, damaging it. For this reason, the condenser is always slightly 'over-designed' to guarantee subcooled flow.

The relation between pressure difference and delivered mass flow for a given RPM of a pump is generally known. Usually this relation is defined by the manufacturer in what are called "pump curves." Figure 2.2 shows such a pump curve for a pump that is very similar to the pump used in the demonstrator setup, only using a different fluid (Galden). The blue lines indicate the different RPM settings, while the black contour lines (isolines) show the hydraulic efficiency regions.

2.1.4. Heat exchanger

To keep the payload at a stable, constant temperature, the evaporator should have a uniform temperature. Therefore the liquid flowing into the evaporator should already be at saturation temperature. However, the liquid flowing out of the pump is subcooled as explained in section 2.1.3. To increase the efficiency of the evaporator, a heat exchanger is added between the evaporator and the rest of the system (as illustrated in figure 2.1). Here the subcooled liquid from the pump is heated to (near) saturation temperature using heat from the fluid flowing out of the evaporator.

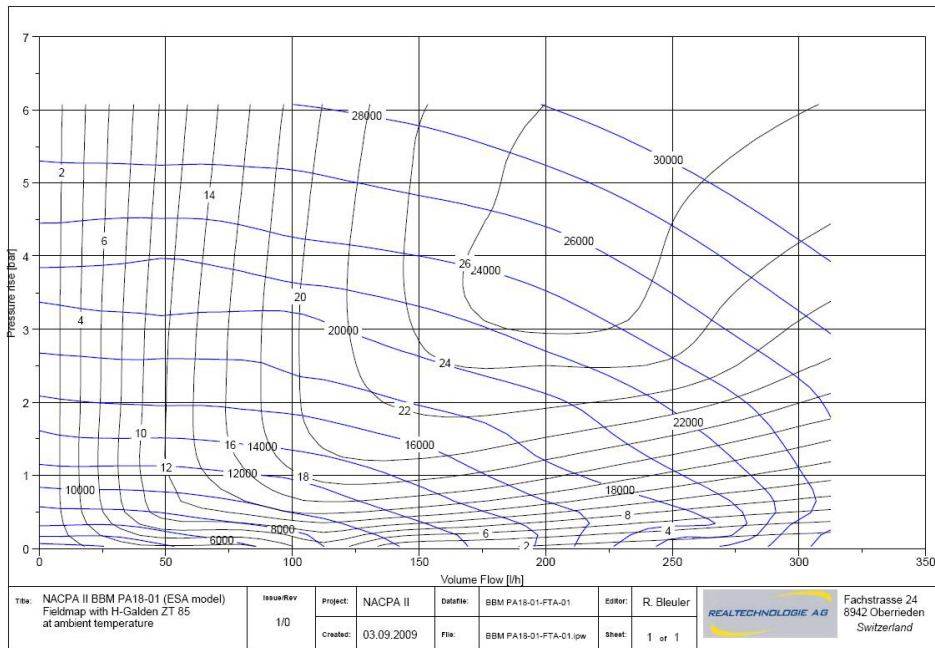


Figure 2.2: Pump curve of the NACPA II pump, using 'Galden' fluid at ambient conditions.

2.1.5. Accumulator

The performance of a two-phase cooling system is highly dependent on maintaining the correct saturation temperature. In the real-world application of these systems, the cooling system is unable to directly control the power/heat input on the evaporator (it works 'in service of' the payload that needs to be cooled and is not supposed to influence it), nor is it able to exactly control the amount of power that can be dissipated through the condensers. Therefore the easiest way to ensure that the fluid in the evaporators is maintained at the correct (saturation) temperature is by controlling the system pressure. Ideally, the pressure inside the evaporator should always remain constant. This is the main role of the accumulator.

There are multiple ways to control the pressure inside the accumulator. The most direct way to do this is by changing the internal volume of the accumulator. If the volume of the accumulator (and thereby the total volume of the system) is decreased, the pressure will rise. If the volume increases the pressure will fall. The volume of the accumulator can be controlled for example by using a bellows or piston system inside the accumulator. This can be done actively (using some sort of electromechanical system) or passively (using a spring-loaded piston or a secondary pressuriser gas). While this sounds rather simple, it requires a lot of extra heavy and/or complex equipment, so it is only usable for large scale systems on Earth. This type of system is called a Pressure Controlled Accumulator (PCA).

Another method of controlling the pressure inside the accumulator is by heating or cooling the fluid inside the accumulator (called a Heat Controlled Accumulator, HCA). When the fluid is maintained at the saturation temperature, the pressure can be controlled by adding or removing heat from the fluid. When heat is added, some of the liquid will evaporate, increasing the gas fraction and thereby increasing the pressure. When the gas is cooled slightly, some of it will condense, decreasing the pressure. This is a much simpler system to build and control, since it only requires a small heater and a cooling element. It does, however, have a much lower reaction time to sudden pressure changes (such as payload suddenly switching on).

2.1.6. Typical responses in a two-phase system

The sections above described how each of the subsystems works individually. The complexity of a two-phase system, however, lies in the interaction between these subsystems and how the system as a whole reacts to changing heat loads (one of the most important applications of a two-phase system

and the 'raison d'être' of the accumulator). When the heat load on an evaporator suddenly increases, (more) liquid starts to evaporate. As the vapour has a much lower density than the liquid, it expands to take up more volume and the flow velocity increases to maintain mass flow. This results in a density 'front' or wave, that pushes everything in front of it forward. Figure 2.3 gives a simplified, schematic overview of this process in the worst-case scenario.

In this drawing, the power is switched from 0 to maximum, meaning that the fluid leaving the evaporator changes from 100% liquid to 100% gas. The expanding vapour pushes the front forward, increasing the liquid velocity and thus the local mass flow. Since the pump will maintain a constant mass flow, the excess fluid will start flowing into the accumulator until a new steady-state has been reached and the mass flow throughout the entire system is again constant. When more power is added in the evaporator and the amount of vapour in the system increases, the pressure will also rise. As explained before, the system compensates for this pressure change by controlling the accumulator (either by changing the internal volume in a PCA, or the gas-to-liquid ratio in a HCA). In reality, power switching is not instantaneous and the flow should never reach a state where only vapour is leaving the evaporator. Rather a two-phase mixture is created, making the density difference across the 'vapour/liquid front' smaller. Thus the amount of liquid flowing into the accumulator would always be smaller than this.

When the heat load suddenly decreases, the opposite happens. Less vapour is created, thus the volume flow out of the evaporator suddenly decreases and liquid starts flowing out of the accumulator. The accumulator will need to reduce its internal volume, or start heating (creating more vapour) to keep the saturation pressure constant.

2.2. Pressure drop

Fluid flowing through a system will never have a constant pressure. In a circulating flow, some amount of energy will be lost due to friction. There are several other effects that can both increase and decrease the local pressure, but in a closed loop, there will always be a net pressure drop.

The pressure influences several other important parameters. In a numerical simulation such as the one under investigation, it is therefore important to know the local pressure for each location throughout the system. The pressure change from location to location is split up in several factors.

The hydrostatic, or gravitational, pressure drop is the easiest to calculate. It is the result of changes in hydrostatic pressure due to the gravitational acceleration on the fluid. The momentum pressure change is caused by a change in velocity or a change in the (total) density of the fluid, such as happens in the evaporator, condenser and heat exchangers. The other two factors are called minor pressure loss and frictional pressure drop. These will be discussed in the next sections.

The loss of pressure throughout the loop is counteracted by the pump, which maintains the fluid flow and raises the pressure. The total pressure drop is usually measured 'over the pump', referring to the pressure difference between the outlet and the inlet of the pump.

2.2.1. Minor pressure loss

The minor pressure loss is a collective name for all pressure changes caused by loss of kinetic energy in the flow. Any discontinuities in the tubes, such as sudden changes in tube diameter, sharp corners, manifolds, and other obstructions can create vortices, inducing pressure losses. While the literature always refers to this as 'minor' pressure drop, in some setups all these small effects can add up to be a major contributor to the total pressure drop.

The minor pressure drop throughout the system will be calculated using the standard set of simple, empirical correlations. Therefore, these correlations will be used for both the single-phase and two-phase flow. No literature could be found that discusses minor pressure drop in two-phase systems. While the empirical correlations are probably not as exact for the two-phase flow, the error is assumed to be small enough so that it can still be used.

2.2.2. Frictional pressure loss

In contrast to the previous parts, the frictional pressure loss of two-phase flows is well-researched and extensively documented. However, it is a very complex subject and a purely analytic solution has not been found for neither the single phase, nor two-phase flows.

The frictional pressure drop of single-phase flows is calculated using the so-called friction factor. For laminar flows (where the Reynolds number is below 2400), a very simple derivation of Poiseuille's

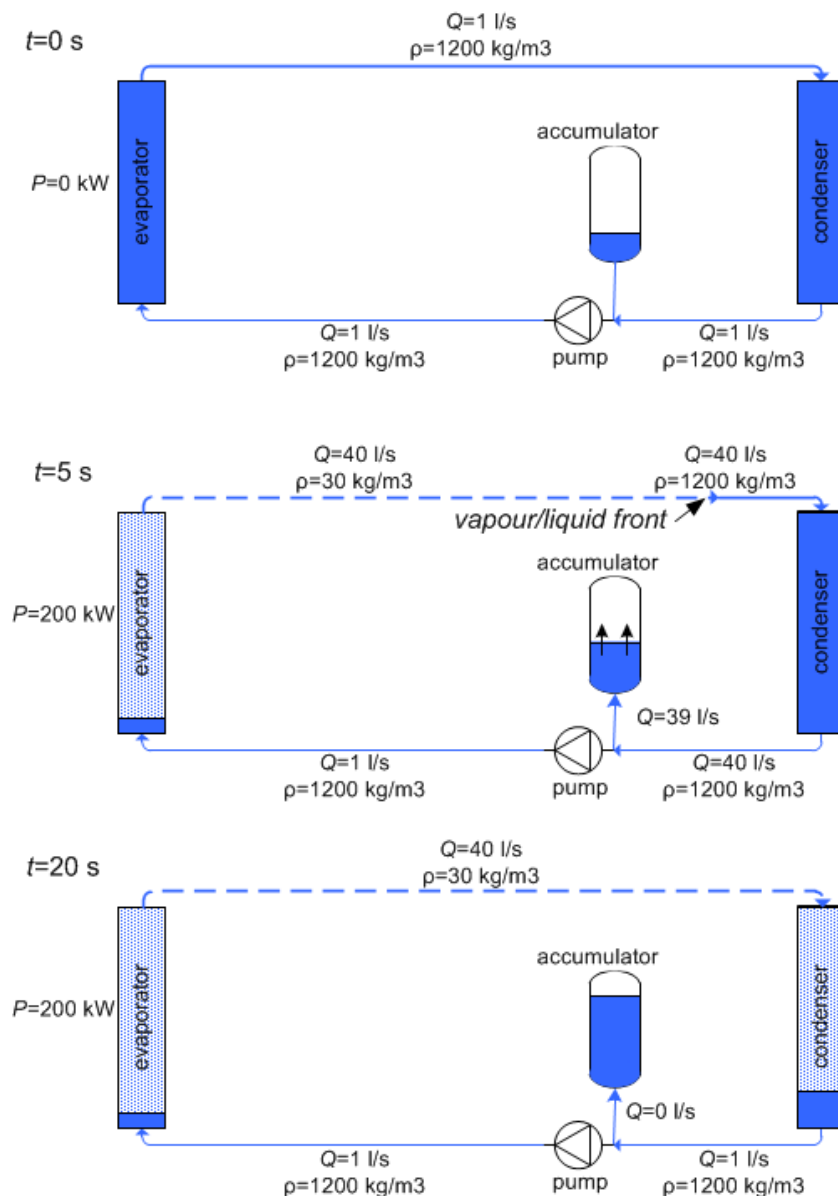


Figure 2.3: Responses of a simplified setup to evaporator power switching, using R134a at a saturation temperature around 25 °C (adapted from a drawing by Van Gerner). Q is the local volume flow, values are rounded for clarity.

law is used [6]. For turbulent flows (Reynolds numbers above 4000), the empirical Haaland equation [7] will be used, as it appears to be the most reliable in literature. Between the laminar and turbulent flows, there is a large discontinuity. This gap is bridged to form a continuous curve using a smoothing function commonly used at the NLR [8].

For calculation of the two-phase pressure drops, a combination of single-phase friction factor and a two-phase 'multiplier' is used. Several different two-phase friction factor correlations have been selected from the available literature that are stated to perform well within the boundaries of the experimental setup. These correlations are developed using specific single-phase friction factors and therefore, the implementation in the numerical model should allow for the friction factor to be changed in accordance with the selected two-phase friction correlation.

The correlations found in the literature study, along with their corresponding single-phase friction factor equations can be found in table 2.1. All of these use the Poiseuille friction factor for laminar flows and the indicated equation for turbulent flows. The Kim and Mudawar correlation [3] additionally uses the Incropera friction factor [6] for turbulent flows with very high Reynolds numbers (above 20000).

In contrast to the other two-phase pressure drop correlations Xu and Fang [9] do not use Blasius, but instead employ two new single-phase friction factor equations developed by Fang, Xu and Zhou [10]. One is specially developed for tubing with rough internal structure, while the other is for smooth channels. All of the equations can be found in appendix B and are more fully explained in the literature study report [4].

Table 2.1: Selected two-phase frictional pressure drop correlations and their corresponding friction factors

Two-phase correlation	Turbulent single-phase Friction factor
Muller-Steinhagen & Heck [11]	Blasius [12]
Friedel [1]	Blasius
Kim & Mudawar [3]	Blasius and Incropera [6]
Lockhart & Martinelli [13]	Blasius
Xu & Fang [9]	Fang (smooth) [10]
Xu & Fang [9]	Fang (rough) [10]

2.3. Heat transfer coefficient

The heat transfer is another important element in the development of a complete two-phase simulation model. This value determines the temperature difference between the payload and the fluid as well as the amount of heat that can be transferred in the condensers. For the single-phase portion of the flow, the Gnielinsky correlation [14] will be used. This is a well established model with a proven accuracy.

For the two-phase portion of the flow, multiple correlations are selected. These correlations were developed and tested for simple tubing layouts in isolated laboratory environments, but not verified to work in the complex geometry of a real-world system. Three different correlations were selected: The Gungor-Winterton correlation [2] one of the most used and verified equations for two-phase flows. Kim and Mudawar, who have also developed correlations for two-phase pressure drop as discussed above, developed a correlation that tries to incorporate the effect of dryout in the calculation. Finally, there is a model developed by Fang [15] (who also worked on a pressure drop equation discussed before), that is developed for the R134a coolant specifically.

As can be seen in figure 2.4, the predicted behaviour of each of these correlations differs significantly. Therefore, extensive testing with the final model will be required to find the best performing equation. This figure shows the results for the fluid R134a and conditions expected in the experimental test setup.

2.4. Void fractions

The final parameter that was examined is the void fraction. The void fraction (or vapour volume fraction) signifies how much of the volume or cross-section of the tubing is taken up by vapour. This number can change independently of the vapour mass fraction, as the two phases can move at different velocities [18]. This value has little to no influence on the steady-state simulation of a system and is very hard to measure directly, but it influences the local density and mass flow inside the system and therefore determines the amount of liquid that will flow in or out of the accumulator. Therefore, it will likely have a significant impact on the transient responses of the system and drives the accumulator design [19].

The current model uses the homogeneous flow assumption, meaning that the two phases are assumed to travel at identical velocities. However, in reality, this is usually not the case [20]. Over the years there has been a lot of research into finding an accurate correlation to predict the void fraction, but there is no independent validation and little consensus on the actual best performing correlation. Therefore, six different void fraction models will be implemented and tested. As part of the verification and validation phases, their performance will be compared and the best one selected.

The Zivi [21], Baroczy [22], Butterworth [23], and Smith [24] correlations make a direct prediction of the velocity ratio between the liquid and the vapour flows. The Woldesemayat & Ghajar [18], and Rouhani & Axelsson [25] models both use a prediction of the 'flux' of the individual phase velocities relative to the 'total' flow velocity as a basis to determine the void fraction. Figure 2.5 shows a comparison

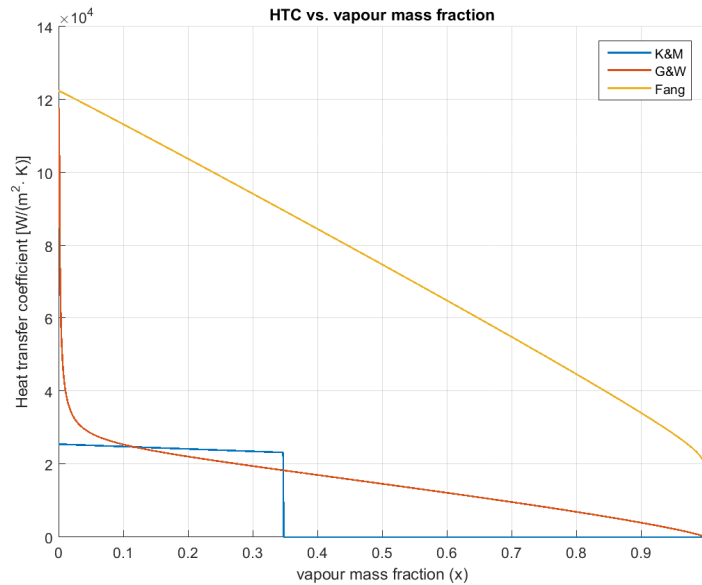


Figure 2.4: Heat transfer coefficients for evaporating flow, as predicted by the Kim & Mudawar [16, 17], Gungor & Winterton [2] and Fang [15] models for R134a at a saturation temperature of 25 [°C] and a mass flux of 700 [kg/(m³·s)] and a hydraulic diameter of 1.2 [mm]

between the proposed correlations. Especially at low vapour mass fraction, a significant difference can be seen between. This is expected to result in significantly different simulated the transient behaviours.

2.5. Literature study conclusions

The literature study clearly showed that it is extremely difficult to accurately model the behaviour of two-phase systems. There are so many variables that influence the flow patterns of a two-phase flow that it is impossible to account for them all. This shows in the fact that most of the papers found in this study evaluate the performance of these correlations with regards to 30% error margins, with the best correlations only barely staying within these margins as shown for example in figure 2.6.

Each of these models is tuned to a different set of conditions and data points. Therefore, it is hard to truly compare them and predict purely based on the literature study which of them will produce the most accurate result in the numerical simulation. Since the conditions inside a two-phase system differ depending on the location and can change with time, there is no single correlation that works for the whole system. Moreover, these correlations were developed to calculate the steady state behaviour in relatively simple setups, so it is unknown how well they will work in predicting dynamic behaviour in a complex system. This is why for each parameter, multiple correlations were selected for further study and implementation in the thesis.

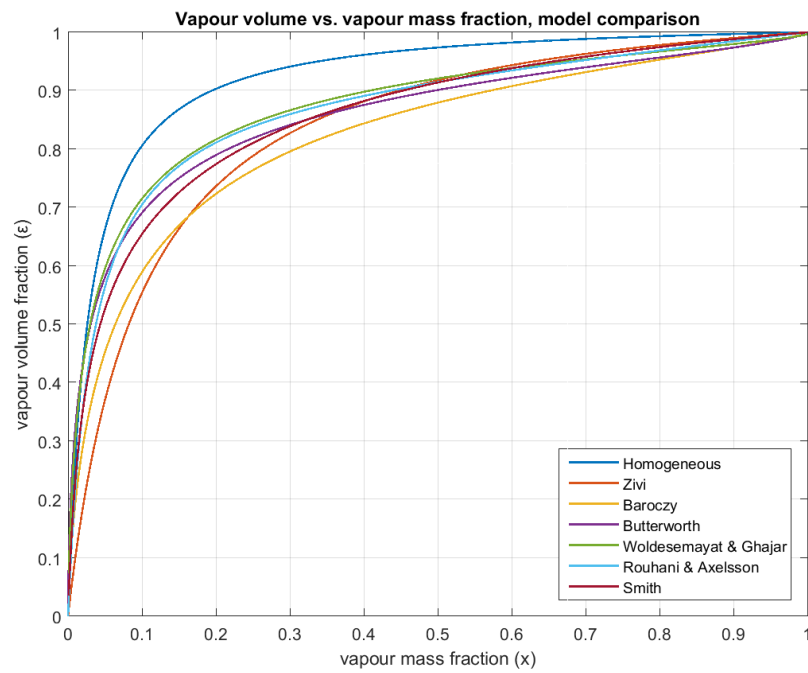


Figure 2.5: vapour volume fraction versus vapour mass fraction for R134a at a saturation temperature of 25 [°C] and a mass flow of 700 [kg/(m³·s)] and a hydraulic diameter of 1.2 [mm], as predicted by the discussed models.

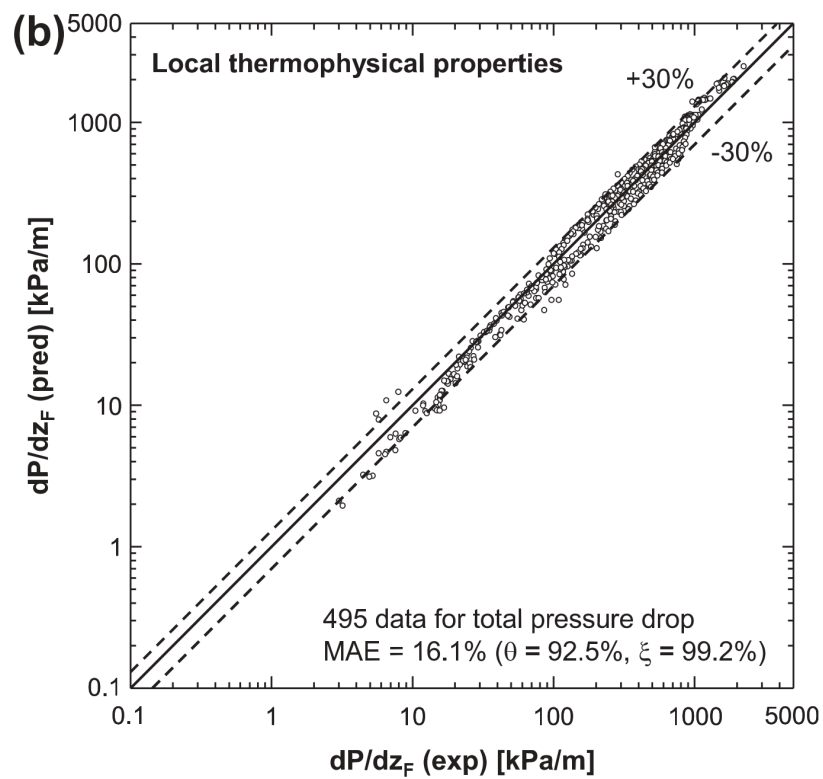


Figure 2.6: Plot from a Kim & Mudawar paper showing the accuracy of their new boiling flow pressure drop [26]

3

Research setup

The first step in performing a research study is defining a plan. At the end of the literature study report [4], a research objective was formed, from which a set of research questions were distilled. These were slightly refined after review of this report and are presented in sections 3.1 and 3.2. From these, a research plan was formulated, which is explained in section 3.3. Next, the two main resources that will be used in this study are presented. First, a short explanation will be given about the NLR two-phase demonstrator setup. This is an experimental prototype of a two-phase fluid loop cooling system that will be used to obtain experimental results for the validation of the final model, as explained in section 3.4. Finally, the existing numerical simulation model will be presented in section 3.5. This is the base program, which will be improved and expanded during this thesis.

3.1. Research Objective

To develop an all-encompassing numerical simulation that can predict the transient behaviour of two-phase pumped loop thermal control systems, by implementing existing steady-state correlations in a discrete numerical model.

3.2. Research Questions

The basis for this project is formed by an existing numerical simulation model for two-phase thermal control systems built by Van Gerner [27], which will be introduced in section 3.5. This model was only developed and tested for small systems using CO₂ as coolant and has some other limitations, so it needs to be expanded and improved in order to become the “all-encompassing” model stipulated by the objective. The main research question then becomes whether it is indeed possible to improve the model to such an extent that it can accurately predict the behaviour of any two-phase system.

To benchmark this accuracy, three parameters are chosen: The temperature, the pressure and the liquid level inside the accumulators. These parameters are important indicators of the system performance, while also being directly measurable in the setup. The goal is to reach an overall accuracy that is as close as possible to that of the individual correlations, thus using the same 30% error margins as found in the literature study.

It is hard to predict in advance which of the correlations will perform best in a numerical simulation with complex geometries, as this is not really what these equations were designed for. By testing all of them, the best ones can be selected for use in the final model. Similarly, there is no published research available on the development of numerical models for the simulation of two-phase loops (other than the papers and reports by Van Gerner and previous interns at the NLR). Moreover, there is no literature that discusses the discrepancies and inaccuracies caused by the (mis-)application of these correlations. Thus it is important to find out what are the largest causes of errors to determine the applicability of the correlations, discover areas of the code that need to be improved and as a starting point for future research.

Once the model is working and producing results within the required accuracy range, the limits of its validity and applicability need to be tested before it can be used by industry. The first step is to

determine the validity range of the model in the current setup. The second part is to determine how accurate the simulation is in predicting the behaviour of other coolants. These last two steps together will give an indication of how well the research goal has been met.

All of this work can be summarised in the five research questions below:

1. Can the existing numerical model be adjusted to predict the dynamic responses to changing heat input, with regards to temperature, pressure and accumulator liquid level with mean absolute errors less than 30 %?
2. Which of the proposed correlations provides the most accurate predictions of the performance of the demonstrator setup filled with R134a?
3. What are the leading causes of inaccuracies in the numerical results? (Inaccurate correlations, uncertainties in internal geometries, assumptions)?
4. What is the achievable accuracy and expected validity range of the final numerical model?
5. Can the resulting numerical model be used to predict the dynamic performance of different fluids, without any further adjustments other than the different input parameters?

3.3. Research Plan

After finding and choosing a set of correlations during the literature study [4], summarised in chapter 2, the first step is preparing the numerical model. A numerical representation of the geometric layout of the NLR demonstrator setup needs to be developed and the existing numerical model needs to be adapted and expanded to allow for implementation of the new correlations. These steps will be explained in chapters 4 and 5.

After the adaptations are complete, proper operation of the model will be verified. First any major errors and bugs that prevent the model from running will be investigated and addressed. Since the original model is in working order, any critical errors that come up will most likely be caused by the new implementations covered in this research project, and are therefore considered relevant for discussion.

Once the model is operational and able to function without errors, the second step of the verification process will consist of a sanity check of the results. This step is to check if the results are realistic and the model operates as expected. The output data will be examined and compared with the expected results and the (steady state) solutions found using some manual calculations.

Finally, the model will be validated using data to be gathered using the demonstrator setup. A series of tests will be run in the physical experimental setup and the same conditions will be simulated several times using different combinations of correlations in the numerical model. During this validation phase, the results will be checked against the research questions given above, the best combination of correlations will be selected and the final model accuracy will be determined.

3.4. Two-Phase Demonstrator setup

A two-phase cooling system demonstrator setup has been built at the NLR. This 'demonstrator' was developed with two goals in mind. First of all it can be used to produce experimental data that is not proprietary to a customer, making it freely available for any in-house developments. Of particular interest is the ability to use this data to verify the performance of the numeric model for fluids other than CO₂ (mainly R134a). Secondly, this setup can easily be reconfigured in the future to test new components, concepts and ideas.

The overall design was developed by van Gerner and colleagues in 2014 and the initial performance analysis was performed by J. Terpstra [8]. Figure 3.1 shows a photograph of the (almost) complete setup. In addition to the basic elements shown in the schematic drawing of figure 2.1, it includes several extra elements. All the way at the back of the setup (middle-left on the picture), the condenser is shown. In this case the condenser consists of a plate heat exchanger where the secondary side is cooled using a pumped water loop. At the top, three parallel evaporators are shown, heated by resistive heater pads. The accumulator in this setup consists of two communicating pressure vessels, connected both at the top and bottom to ensure equal pressure and liquid levels. This is a Heat-Controlled Accumulator (explained in section 2.1.5). Both vessels contain heaters, but only one can

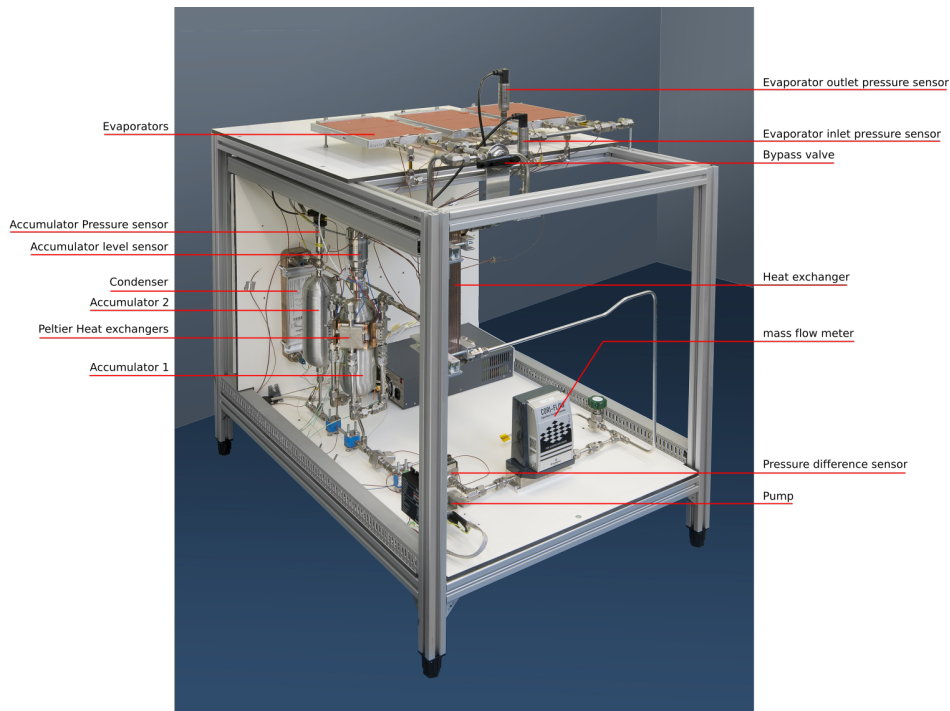


Figure 3.1: A picture of the demonstrator set-up with the most important components highlighted

be actively cooled, as can be seen in figure 3.1. The heat control uses two resistance heaters (with a maximum power of 200 [W]) inserted into the fluid at the bottom of each vessel and four Peltier coolers on the outside one of the vessel, near the top (where the vapour collects under gravity). The dissipative side of the Peltier elements is cooled using the two-phase flow in four extra evaporators, installed between the heat exchanger and the condenser. This is illustrated in figure 3.2 for clarification.

The demonstrator loop contains a number of sensors. Some of these are used in the control loop, but most were installed to measure the performance and gather data for model verification and validation purposes. All in all, there are 24 thermocouples, 3 pressure sensors, 1 ΔP sensor, a liquid level (height) sensor in the accumulator and a coriolis mass flow meter. The locations of the most important of these are shown in figure 3.1. More information on these elements can be found in appendix A.

As mentioned before, the demonstrator is mainly developed for use of R134a as refrigerant at a maximum of 35 [°C] (corresponding to a maximum pressure of around 8.5 [bar]). The hydraulic channel

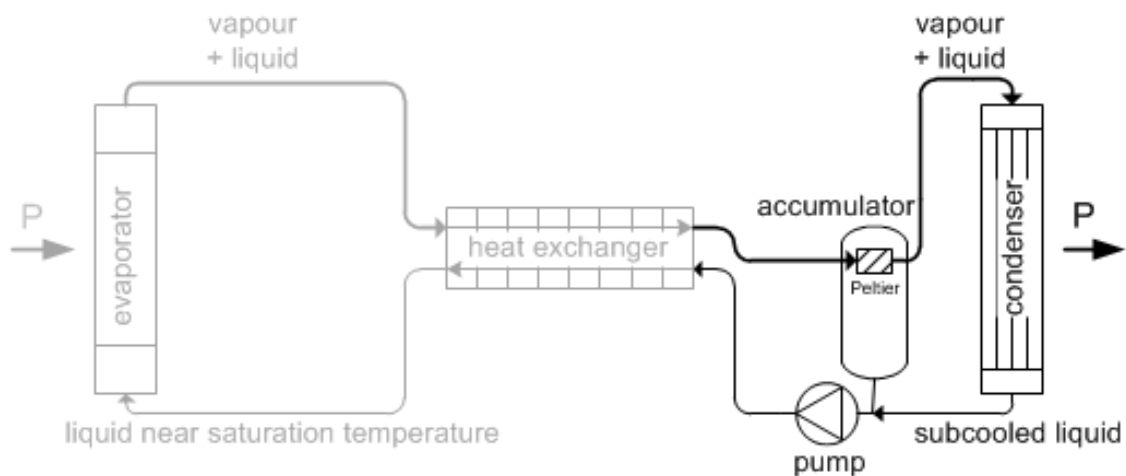


Figure 3.2: Adjusted version of figure 2.1 showing the location of the peltier-cooling evaporators in the flow schematic

diameters in each element of the demonstrator are listed in table 3.1, as well as the number of parallel channels. A lot of these values are assumptions, as the real number of channels is unknown (and hard to physically quantify) in the plate heat exchangers and the evaporators. The assumptions were made by Terpstra [8] by iteratively comparing the predicted pressure drops with the known quantities stated by the manufacturers.

Table 3.1: Tube diameters in the different elements of the demonstrator

Element	Hydraulic diameter	Number of parallel channels
Evaporator	1.2 mm (assumed)	3 x 38 (assumed)
Two-phase tubing	10 mm	1
Heat exchanger	3.4 mm (assumed)	13 (assumed)
Peltier coolers	2.2 mm	16
Condenser	4 mm (assumed)	13 (assumed)
Single-phase tubing	6 mm	1

3.5. Numerical model

The simulations will be done using an explicit one-dimensional finite-difference numerical model. As explained in section 3.1, the main goal of this thesis is to expand and improve an existing model. The original model is written in MATLAB by Van Gerner at the NLR between 2013 and 2015 [19, 28].

This model is based on the one-dimensional, time-dependant, compressible Navier-Stokes equations [19]. It was originally written to help in the initial designs of a series of two-phase systems using CO₂ as working fluid. The model can calculate mass flow, pressure, temperature and the heat transfer coefficient along the loop, which generally are the most important performance characteristics.

3.5.1. Structure

The program is organised into a set of nesting functions and sub-functions. This allows for a relatively coherent and uncluttered code. All input parameters, constants and settings are defined at the beginning of the main file (*DynamicModel.m*). This modular approach makes it easy to alter specific correlations or settings, without having to go through the whole code.

The geometry is implemented as a series of components. Each component is defined as a single tube or multiple parallel tubes of a specified length and diameter and saved in a MATLAB *'struct'*. This struct also contains the number of parallel tubes, the shape (round or square), the internal roughness, the orientation, thermal mass, and specific heat of the tubing, as well as the diameter and length of potential restrictions and the minor pressure loss coefficient due to other discontinuities in the geometry. The model further discretises each component into a series of elements of around 2 cm³ in volume. The exact numerical implementation of the physical layout will be explained in chapter 4.

The most important function called in the main file is the *CalcTimeLoop.m* code. After the input parameters are defined and the geometry is loaded, this function runs through the entire time-marching while-loop that is at the heart of the actual finite-difference numerical simulation. It does this by calling on a long list of subfunctions to perform the actual calculations. A list of all the calculation sets and the order in which they are executed for each time step can be found in appendix C.

3.5.2. Mathematical basis

The numerical fluid flow simulation is based on a simplified subset of the time-dependant 1-dimensional Navier-Stokes equations. Van Gerner [19, 28] developed these equations of state by rewriting the equations and eliminating terms using a set of assumptions discussed below. The original Navier-Stokes contains three equations, based on the conservation of mass, momentum and enthalpy respectively. After simplification, only the reduced mass and enthalpy equations remain as shown below. Eliminating the momentum equation has the disadvantage that pressure waves in the system cannot be simulated. But that also means that the size of the time steps is dependant on the fluid velocity instead of the speed of sound (which is the velocity of the pressure waves) [19]. The larger time steps that this results in, means a significant reduction in computation time.

$$\text{Enthalpy:} \quad \frac{\partial H}{\partial t} = -u \frac{\partial H}{\partial s} + \frac{Q}{\rho} \quad (3.1)$$

$$\text{Mass:} \quad \frac{\partial u}{\partial s} = -\frac{u \partial \rho}{\rho \partial s} + \frac{\partial \rho}{\rho \partial t} \quad (3.2)$$

In these simplified equations, the change in enthalpy H over time is only dependant on the change in enthalpy over distance, multiplied by the flow velocity and the heat input per unit mass. Similarly, the change in velocity over distance is also dependant on just two terms, relating to the change in density over distance and the change in density over time. By discretising these equations, they can be used to calculate the local enthalpy and velocity for each location in the system.

The enthalpy equation is discretised using the MacCormac predictor-corrector scheme as shown in equations (3.3-3.5). Here, n and i depict the current timestep and element and $n - 1$ and $i - 1$ the previous timestep and element, respectively. The local densities are not calculated, but instead looked up in the Reference Fluid Thermodynamic and Transport Properties Database (REFPROP) developed by the American National Institute of Standards and Technology (NIST). At the NLR, a (licensed) program is used that makes this database directly accessible in MATLAB using a simple function call [29]. This method is used twice, once between the predictor and corrector steps to find a 'temporary' value of the density based on the predicted enthalpy (ρ_i^p) and a second time after the averaging step to find the 'true' density based on the final result of the MacCormac scheme.

$$\text{Predictor:} \quad H_i^p = H_i^{n-1} - u_i^p (H_i^{n-1} - H_{i-1}^{n-1}) \frac{\Delta t}{\Delta s} + \frac{Q_i^{n-1}}{\rho_i^{n-1}} \Delta t \quad (3.3)$$

$$\text{Corrector:} \quad H_i^c = H_i^{n-1} - u_i^p (H_i^p - H_{i-1}^p) \frac{\Delta t}{\Delta s} + \frac{Q_i^{n-1}}{\rho_i^p} \Delta t \quad (3.4)$$

$$\text{Averaging:} \quad H_i^n = \frac{H_i^p + H_i^c}{2} \quad (3.5)$$

The velocity is determined using a single forward-differencing step as shown in equation (3.6). These are the only calculations that determine the change in state from one time step to the next. All other values are completely recalculated for each time step, based on the results of these equations.

$$u_i^n = u_{i-1}^n - \frac{u_{i-1}^n}{\rho_{i-1}^n} (\rho_i^n - \rho_{i-1}^n) - \frac{(\rho_{i-1}^n - \rho_{i-1}^{n-1}) \Delta s}{\rho_{i-1}^{n-1} \Delta t} \quad (3.6)$$

To summarise, a schematic overview of the steps described above is given in figure 3.3. As shown here, the first step is the MacCormac predictor step, which uses the 'old' value for the local density (from the previous timestep). Then, a new value for the fluid density (ρ_{pr}) is calculated with the enthalpy predicted by the first MacCormac step. Then the MacCormac equation is run again, but now using the new density to 'correct' the previous result. The final enthalpy is the average of these predictor and corrector steps. Following this, the density is recalculated using the new enthalpy value. And finally, the new flow velocity is calculated using the forward differencing scheme and the new density value.

The length of each time step is determined by the local velocities and the size of the discretised elements of the geometry. For the stability of the simulation it is important that during each individual time step, the fluid never travels further than the length of a single element. On the other hand, the time steps should be as large as possible for faster computation. To assure this, the optimal length of each new time step is recalculated, based on the results of the previous one. The traversing time of each element during the previous time step is calculated and multiplied by a Courant–Friedrichs–Lewy (CFL) parameter [30] of 0.85 to ensure that the traversed distance of the fluid is always smaller than the element length, even if the velocity increases (slightly) in relation to the previous time step. The process is shown in equations (3.7) and (3.8).

$$t_i = \frac{L_i}{u_i} c_{CFL} \quad (3.7)$$

$$t_n = \min\{t_i\} \quad (3.8)$$

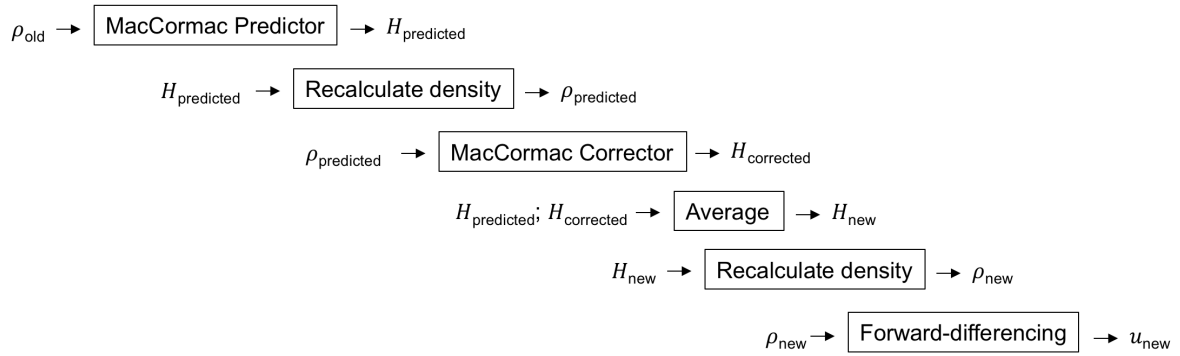


Figure 3.3: Schematic representation of the order of calculation steps required to calculate the local density and velocity values.

3.5.3. Assumptions

As mentioned above, the program relies on a series of simplifications and assumptions for several reasons, but most importantly to reduce the computation time and to manage development effort for the model [27]. Also, the original model was built for simulating loops containing CO₂ as a working fluid. So, the assumptions and most of the originally included correlations were chosen specifically with this fluid in mind, and might not be fully applicable to simulating loops with other working fluids. The most important of these will be discussed below.

- "It is assumed that the liquid and vapour in a mixed flow have the same temperature and velocity (i.e. the homogeneous flow model is assumed)." [19]

This assumption ensures that the equations of state and their discretisation remain relatively simple. The tests performed by Van Gerner [19] show that this assumption is valid for CO₂, but this might not be the case for other fluids, as discussed in chapter 2. As part of this thesis, the validity of this assumption with regards to R134a as a fluid will be tested and a few options for (partially) negating this assumption by implementing new void fraction models will be investigated.

- "Only the mass (or continuity) equation and enthalpy equation are initially solved. The momentum equation is not solved directly." [19]

This simplification has major impact on the length of each time step and therefore the computation time as a whole. The momentum equation is required to calculate the formation and progression of pressure waves. However, since these pressure waves travel at the speed of sound it means that the time steps also have to be limited by the local sound velocity. The other equations are dependant on the fluid velocity, which is generally several factors of magnitude lower than the sound velocity. Thus, by ignoring these pressure waves and the momentum equation, a small reduction in accuracy is traded in for much larger time steps and a significantly faster simulation. [19]

- Gravity is ignored [19].

In the original model, gravity is not taken into account. All the CO₂ loops that were simulated previously were prototypes that were built on a (mostly) flat, horizontal layout and thus inclusion of the gravitational effects was not required. This means that the gravity term in the original Navier-Stokes energy equation was taken out for simplification.

The new demonstrator setup, however, does have a three-dimensional geometry, including several tubes that span relatively large vertical distances (up to 1 [m]). This means that the original assumption is no longer completely valid. But, the effect of gravity is still assumed to be negligibly small in relation to the heat and velocity terms in the enthalpy equation. Therefore, it was chosen to not change the equations of state from the original model. Gravity will be included in the pressure drop equations, as will be discussed in chapter 5.

- The mass flow out of pump is assumed to remain constant.

In reality, the mass flow will fluctuate slightly during transient effects. The exact pump curve for R134a through this specific pump is not known, making it difficult to accurately simulate without significant additional work. During the experiments, the massflow meter and pump control loop are able to react fast enough to return the mass flow to the setpoint (15 g/s) within a fraction of a second. Therefore, the choice was made to keep this part of the simulation simple and set the pump outlet massflow as a constant.

3.6. conclusion

The goal of this thesis is to improve the existing numerical model and make it more broadly applicable. The most important step towards that goal is to implement the new pressure drop, heat transfer coefficient and void fraction correlations from the literature study. Additional improvements will be made along the way in two facets: Increasing the accuracy of the simulation and improving the 'control interface' of the model. This includes adjusting the equations of state to remove the homogeneous flow assumption, adding gravitational acceleration and minor pressure drop and relocating all control parameter definition to the first section of the code. Other improvements include adding save and load functionality to simulation runs and making sure the model stores all data when encountering an error.

Apart from these model improvements, the experimental setup will have to be prepared and its geometry needs to be implemented numerically. Finally, the model needs to be verified and validated. First by running tests and checking for errors or unexpected outcomes. Afterwards, the results will be compared to the experimental data and the accuracy of the model can be determined.

4

Numerical implementation of the demonstrator geometry

The demonstrator setup was hand-built by the engineers at the NLR. While most components were procured 'off the shelf', some of the parts were altered in-house or even made from scratch. This chapter will describe the methods used to determine the (internal) geometry of all components and how they were implemented numerically. Section 4.1 describes this process for the regular tubing and section 4.2 discusses the more complex components. Finally, section 4.3 describes how the geometry was simplified numerically, in order to achieve better model performance.

4.1. Tubing

All tubing was bought off-the-shelf from *Dockweiler* and was made-to-fit by the NLR engineers. Since the measurements, cuts and bends were all performed by hand, there are no exact drawings or documented set of dimensions available. Instead, all tubing was (re-)measured by hand, meaning that there is an expected error margin of around 2 [mm] for all the tube lengths and elevation heights. The internal surface roughness of all elements is estimated at $1 \cdot 10^{-6}$ m. This is a standard assumption used at the NLR, based on manufacturer data and experience in the NLR labs.

4.2. Special components

The evaporators, condenser, heat exchanger and massflow sensor are all commercial off-the-shelf units with complex interior geometry. Exact diagrams of the internal layout of these components is not publicly available. Therefore, Terpstra developed a simple piece of code that can predict an approximate geometry based on the figures for pressure drop and total heat exchanging surface area stated in the component data sheets [8].

The Peltier heat exchangers consist of four identical components which were designed and 3D-printed internally at the NLR. They have a very simple internal layout, consisting of 16 parallel, circular channels with a diameter of 2.2 mm. The inlet and outlet manifold are not directly simulated, but the kinetic losses in these elements will be accounted for by the minor pressure loss equations.

The accumulator is not defined in the geometry file, since it is not a flow-through element in the loop. Instead, it is treated as a single 'element', with its volume, diameter, height, empty mass and other parameters defined in the main model file (*DynamicModel.m*). The internal dimensions were approximated using the values and drawing given in figure A.4 in Appendix A. These values are used at the end of every loop in *CalcTimeLoop.m* to calculate the liquid level height from the liquid volume.

4.3. Simplified geometry

The initial geometry implementation defined each piece of tubing as a separate component. Each union, elbow, tee was considered a 'break' between components and every instance where the tubing changed direction from the horizontal to the vertical plane was considered as the start of a new component as

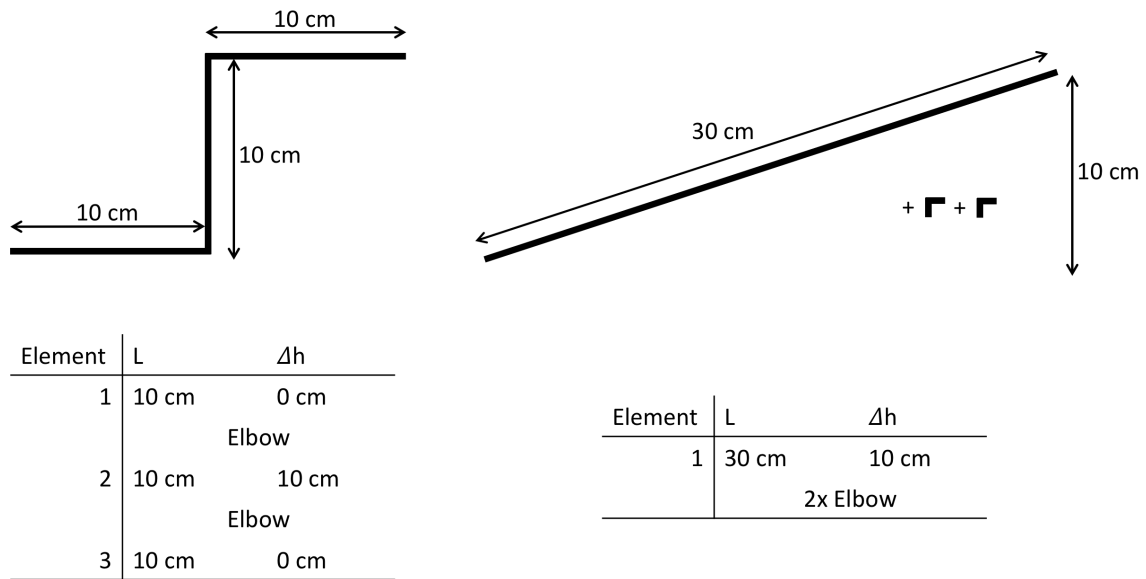


Figure 4.1: Example of the geometry simplification discussed in this chapter

well. This resulted in a very detailed description of the system, showing the exact local influences of gravitational and minor pressure drop. However, this also led to several very short components.

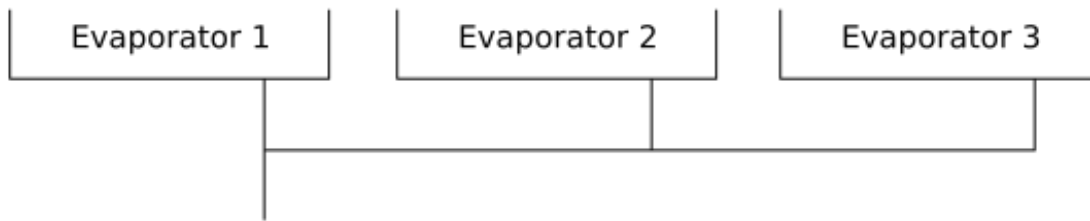
The numerical model requires a minimum of three elements per component. Because some of the components between the Peltier elements and around the evaporator manifolds were so short, the effective volume of each of the three elements in these components was reduced to fit three elements in the component. As the time step is calculated on the basis of the time it takes for the fluid to travel through an element, smaller elements will lead to smaller time steps for each loop iteration. Thus leading to more iterations and more calculations required in the simulation and a significantly slower model.

To solve this, the geometry file was simplified where possible by combining multiple tube sections in each component. Minor pressure drop elements are now grouped at the end of each component, and combinations of vertical and horizontal tube sections are now represented as sloping, meaning that the gravitational pressure change is spread out over the entire component instead of only the vertical section. A basic example of this simplification is shown in figure 4.1. This results in a slight reduction in resolution of the model, meaning that the numerical model no longer corresponds precisely to the layout of the real setup. Some equations, such as the gravitational and minor pressure drop calculations, lose some accuracy, since they are no longer calculated in the exact location where they occur in reality, meaning the flow characteristics at the point of calculation might be slightly off. The exact size of these induced errors is unknown, but assumed to be well within the error margin of the equations used to calculate these parameters.

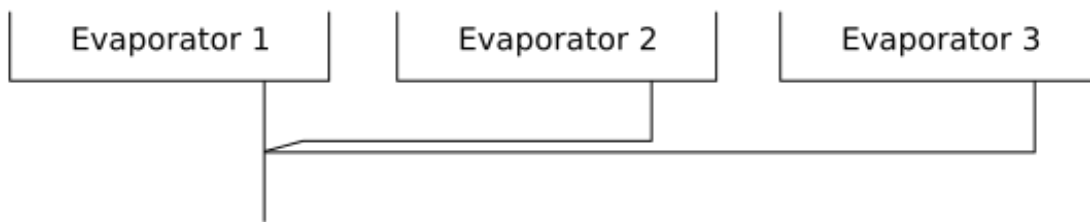
There are two places where the simulated (simplified) geometry could not exactly match the actual layout of the demonstrator setup. The connection between the evaporator inlet manifold and the second evaporator consists of a restriction tube and a single segment of 80mm in length, or about a single element in size. Since it sits between the manifold and the evaporator, it cannot be combined with any other element. To prevent this segment from causing slower calculations, its actual length was tripled in the simulation. This will lead to a slightly increased pressure drop, but the effect is insignificantly small compared to the error margins of the correlations (around 13 Pa compared to a 30 kPa total pressure drop at 1500W).

The other location where reality and the simplified geometry differ is at the evaporator outlet manifold. Unlike the inlet manifold, which consists of a four-way-connector in the middle near evaporator 2, with two symmetric tubes leading left and right to evaporators 1 and 3, the outlet is asymmetric. The outflow of evaporator 3 is combined with the evaporator 2 outflow in a t-connector and a single tube carrying the combined flow of these two evaporators combines with the outflow of the first evaporator

through a second t-connector. So there are effectively two staggered outflow manifolds, as shown schematically in figure 4.2a. For simplicity in the simulation, it was chosen to split the outflows from evaporators 2 and 3 and combine them with the evaporator 1 outflow in a single manifold as depicted in figure 4.2b. The most important consequence is that the frictional pressure in the 'split' section of tubing is not correct, but the difference is again only a couple of Pa, thus considered insignificant.



(a) Actual layout of the evaporator outlet manifolds



(b) Simplified outlet manifold layout assumed for simulation

Figure 4.2: Comparison between actual and simulated evaporator outlet manifolds

5

Numerical model adaptation

This chapter will describe the steps taken to expand and improve the existing model. Most of this work went into the implementation of the new correlations that were found during the literature study. Section 5.1 will describe the different elements that contribute to the local pressures and how these elements were adjusted or added to the code. Then, the same process will be discussed for the heat transfer coefficient calculations in section 5.2. Finally, section 5.3 will explain the adaptations that were required to include the void fraction correlations and enable the model to calculate non-homogeneous flows.

5.1. Local Pressure

As explained in section 2.2, there are four main causes of local pressure change. It is important to know the local pressure in order to determine the local (saturation) temperature and several other important parameters influencing the performance of the system, such as the latent heat and the heat transfer coefficient. The total pressure drop in the loop is also important for the performance of the pump. The implementation of the different equations will be discussed below.

While there are many things that influence the local pressures, the overall system pressure is controlled through the accumulators. Therefore, the accumulator pressure is taken as the reference point to calculate all other pressures in the system. This means that the local pressures in the sections between the pump outlet and the accumulator (i.e. practically the whole system) are calculated in reverse order (in the opposite direction of the fluid flow) from the accumulator to the pump outlet.

Before the pressure change throughout a section can be calculated, the pressure difference between that section and the previously calculated section needs to be found. These pressure differences can be caused by minor pressure drop contributions and restrictions as described in sections 5.1.1 and 5.1.2. When the pressure difference between the sections is calculated, the pressure gradient within a section can be calculated using. Implementation of the frictional, gravitational and momentum pressure effects will be discussed in sections 5.1.3 and 5.1.4 respectively.

5.1.1. Minor pressure loss

The first step in the pressure calculations is to determine the minor pressure loss in each component. To simplify the code, all the minor pressure loss contributions are lumped at the end of each section. It is also assumed that the momentum pressure changes due to changes in cross-section are incorporated in the minor pressure loss equations for sudden expansions or contractions. The equation used to calculate the minor pressure drop is given in (5.1) and the relevant minor loss factors (ξ or K_L) are given in figure 5.1.

$$\Delta p_{\text{minor}} = 0.5\xi\rho u^2 \quad (5.1)$$

5.1.2. Pressure drop in restrictions

The simulation time step is determined by the maximum fluid velocity in the system. Higher velocities lead to smaller time steps. The cross-sectional area of the restriction tubes is significantly smaller than

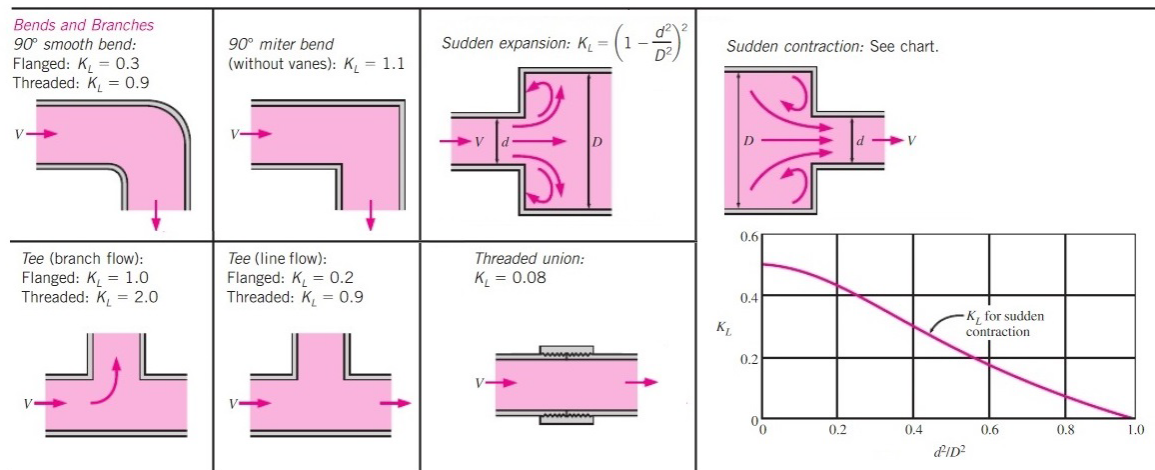


Figure 5.1: Table depicting various flow obstructions and their associated loss factor (here called K_L instead of ξ) according to Çengel [31].

any other element in the system. If they would be included like the rest of the tubing, they would reduce duration of the time steps by a factor of magnitude, directly increasing the calculation time by a factor 10. Therefore, they were not implemented as normal tubes, but as a separate type of element.

Similar to the connectors in the minor pressure drop function, only the pressure drop will be calculated in these sections. All other parameters, such as the temperature, density, and vapour mass fraction are expected to remain unchanged between the inlet and outlet of the restriction tubes. A new function was added that calculates the frictional pressure drop over the entire length of the restriction tube and adds the minor pressure drops of the contraction and expansion. This is illustrated in equation 5.2. The result is then added to the total pressure drop over the neighbouring section.

This implementation means that the stability criterion of section 3.5.2 is technically violated for this section. But the pressure drop is the only parameter affected and the effect is expected to be insignificantly small. On the other hand it will make the calculation a factor of magnitude faster, completely justifying this slight decrease in accuracy.

$$\Delta p_{\text{restriction}} = \Delta p_{\text{minor, inlet}} + \Delta p_{\text{friction, rest.}} + \Delta p_{\text{minor, outlet}} \quad (5.2)$$

5.1.3. Frictional pressure drop

For the frictional pressure drop calculations, a new piece of code (or 'function' as they are called in MATLAB) was written. This independent program (named *CalcDPfric.m*) requires a set of input parameters and outputs the frictional pressure drop values. Making this function independent from the main model keeps the code relatively uncluttered and makes it easy to change the pressure drop equations without having to alter the main code in multiple places, as explained in section 3.5.1.

The frictional pressure drop code is split in multiple parts. First, it is determined if the fluid is fully liquid, or in the two-phase regime. This is done by parsing the vector containing vapour mass fraction values for each element in that component using MATLAB's built-in 'find' function. Every value below 10^{-3} is considered to be in the single-phase flow regime.

Next, the program will calculate the frictional pressure drop of the single-phase and the two-phase elements separately. In the model settings, the different correlations to be used were defined using a set of 'indicators'. These indicators are part of the function inputs and the program chooses which correlation will be used to calculate each part based on the values in each of these indicators.

Single-phase flow For all single-phase elements, the friction factor is calculated using both the laminar-flow equation and the Haaland equation [7], as explained in chapter 2. As mentioned, the gap between the laminar and turbulent flows is bridged by a smoothing factor, which is given in equation 5.3, where Re_l is the Reynolds number of the liquid phase [8]. A continuous curve is then created by multiplying the laminar and turbulent single-phase friction factor with this smoothing factor, as shown

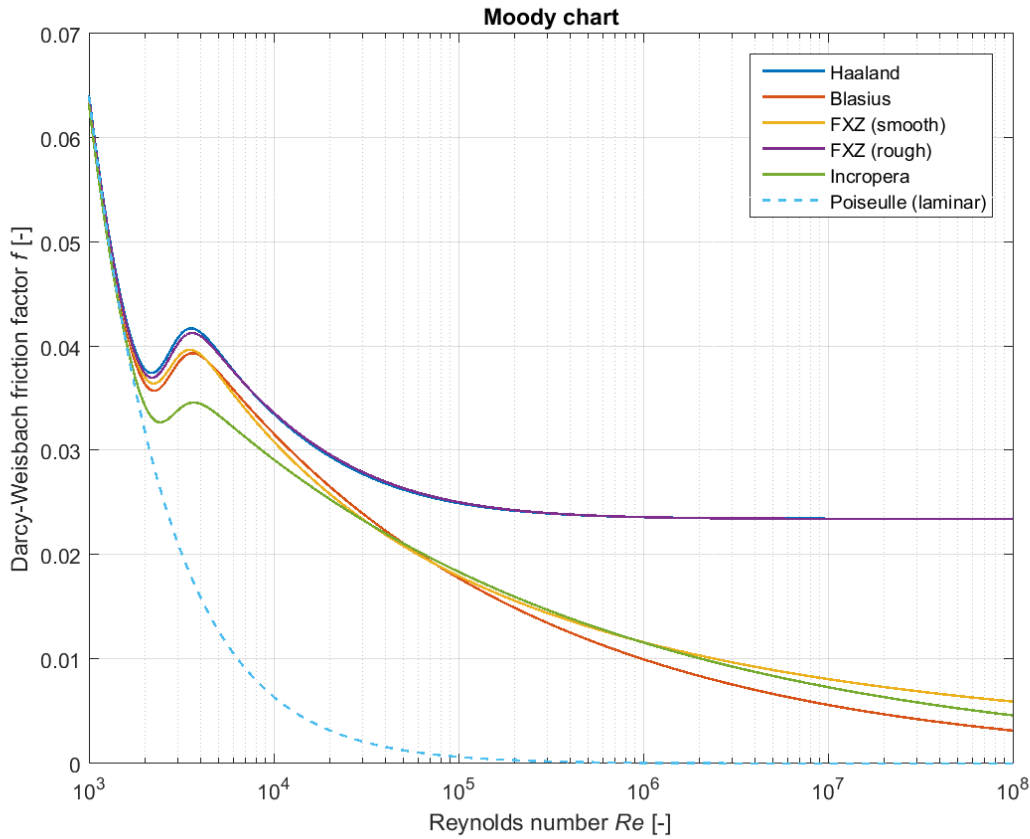


Figure 5.2: A so-called Moody chart showing the predicted friction factors of the different models against a range of Reynolds numbers. The Haaland and FXZ rough equations use a 10 [mm] diameter channel, with a roughness (ϵ) of $0.002d$ (corresponding to a relative roughness of 0.02) [4].

in equation 5.4. Figure 5.2, from the literature study report [4], shows the effect of this smoothing function on the single-phase friction factor correlations.

$$\zeta = \left[1 + e^{\left(\frac{-(Re-2400)}{450} \right)} \right]^{-1} \quad (5.3)$$

$$f = (1 - \zeta)f_{\text{laminar}} + \zeta f_{\text{turbulent}} \quad (5.4)$$

Two-phase flow The two-phase pressure drop requires the combination of a single-phase friction factor coefficient and a two-phase frictional pressure drop correlation. In the literature study, several different friction correlations were discussed.

Lockhart & Martinelli [13], Friedel [1] and Muller-Steinhagen & Heck [11] are all older, 'general' equations, that can be used both for adiabatic and diabatic flows. Kim & Mudawar have two sets of equations: the first are for adiabatic and condensing flows [3] and the second set are specifically derived for evaporating flows [26]. Finally Xu & Fang have developed two separate equations for evaporating [9] and condensing flows [32]. The full equations are shown in appendix B.1.

All of these equations were implemented as separate 'subfunctions' at the end of the *CalcDPfric.m* code. These subfunctions were then called individually based on the value of the correlation indicators defined in the model settings. This keeps the code clear and uncluttered, while allowing the end-user to easily select which correlations to use and making it simple to change them.

The numerical model allows complete freedom in mixing and matching friction factors and two-phase correlations. However, the correlations are all derived empirically using a specific friction factor

as explained in chapter 2. Using these correlations in combination with a different friction factor would likely result in significant errors. Therefore, in the final tests, these correlations will only be used in combination with their intended friction factor, which are shown in table 2.1.

Notes It is important to note that the 'Haaland' and 'Fang, Xu, Zhou' friction factors use both the Reynolds number and the so-called 'relative roughness'. This is the internal roughness of the pipe (in meters) divided by the total diameter. Since the roughness is not exactly known, it is estimated to be $1 \cdot 10^{-6}$ m for all tubing in the system. All the other friction factors are only based on the Reynolds number.

The Kim & Mudawar two-phase, evaporating flow correlation uses the wetted fraction of the tube as one of the parameters to calculate the two-phase pressure drop. It is, however, extremely difficult to accurately calculate the wetted fraction, since it is based on the flow pattern, which depends on so many variables, that there are no simple equations available to approximate it. During the first stages of evaporation, there is only liquid so the wetted fraction must be 1. Further along, more liquid evaporates, so the wetted fraction will undoubtedly slightly decrease, but it is not known by how much. *Therefore, the wetted fraction is assumed to always be equal to 1.* The validation tests will have to show validity of this this assumption.

5.1.4. Gravitational and momentum pressure change

The implementation of the gravitational and momentum effects on the pressure is relatively straightforward. They simply represent the potential and kinetic elements of the Bernoulli equation.

Because of the (numerical) geometry simplification described in chapter 4, the exact height change of each element is unknown, but the total change in elevation of the section is given. Thus the pressure difference due to the total elevation change is calculated and divided equally over all elements in that section.

The momentum or kinetic pressure difference between elements is calculated using the local velocity and density values calculated earlier in the same time step. This only applies to the momentum change between the discretised elements in each 'section'. The kinetic pressure change between sections is assumed to be covered by the minor pressure drop calculations.

$$\Delta p_{\text{gravity}} = \rho_{\text{tot}} g L \sin \theta = \rho_{\text{tot}} g h \quad (5.5)$$

$$\Delta p_{\text{momentum}} = \left(\frac{\rho_{\text{tot}} u_{\text{tot}}^2}{2} \right)_{\text{out}} - \left(\frac{\rho_{\text{tot}} u_{\text{tot}}^2}{2} \right)_{\text{in}} \quad (5.6)$$

5.2. Heat Transfer Coefficient

The Heat Transfer Coefficient (HTC) is an important parameter used in calculation of heat transfer between the tube wall and the fluid. For each part of the system, this parameter is calculated in a different way. The tubing transporting the fluid between the different heat-transferring elements is insulated and therefore assumed to be completely adiabatic. Similarly, the mass flow meter, pump and any other elements that are not specifically defined as heat-exchanging elements are assumed to be adiabatic (even though energy is being added to the system by the pump in the form of pressure and enthalpy).

The method in which the heat transfer in all diabatic elements is calculated will be discussed below. The most important of these are the evaporators, which are discussed in section 5.2.1. After that, section 5.2.2 will describe how the HTC in the condensers and other heat exchangers is defined.

5.2.1. Heat transfer in Evaporators

There are four locations in the geometry where evaporation can occur: The main heat exchanger, the evaporators, the Peltier heat exchanger and the accumulators. This section will only deal with the heat transfer in the evaporators and the Peltier heat exchangers. The heat transfer in the main heat exchanger will be discussed in next section.

The flow through the pump is always subcooled, as explained in chapter 2.1.3. The liquid flow must first reach its saturation temperature before it starts evaporating. Thus, until the liquid reaches its saturation temperature, the heat is transferred through pure forced convection. In most cases,

this happens in the heat exchanger, such that only saturated flow reaches the evaporator. However, in some cases, such as during startup and with low heat input, subcooled liquid can reach the evaporators. Specifically for this reason a single-phase HTC correlation is implemented. For the heat exchangers themselves, the HTC is determined in a different manner, as explained in the next section.

For the liquid-only heat transfer coefficient, a Nusselt number of 3.66 is assumed, in accordance with Incropera & DeWitt [6]. For turbulent flows, the Gnielinski correlation [14] is implemented, which uses the Haaland friction factor [7] (previously mentioned in section 2.2.2). To assure that the right friction factor is used, the Haaland equation is recalculated in the HTC subfunction, instead of relying on the output of the pressure drop function.

During the literature study, three evaporating flow HTC correlations were selected for use in the numerical model. The Gungor-Winterton [2], Kim & Mudawar [17] and the Fang R134a specific [15] correlations. The equations themselves are shown in appendix B.2. They were implemented in a similar manner as the frictional pressure drop equations, meaning that the full calculation was put in a separate function (called *CalcHTC.m*), with each equation in a separate subfunction for easy switching of correlations.

The Fang equation requires two separate viscosity values for the fluid as can be seen in equation (B.25). One at the mean fluid temperature and one at the inner wall temperature. Since this is a one-dimensional model, the temperature and viscosity values are assumed to be constant in radial direction. Therefore, the bulk viscosity of the fluid is used for both input values.

5.2.2. Heat transfer in Condenser and Heat exchanger

The heat exchanger and condenser are both plate heat exchangers built by SWEP. Since these have an unknown, complex internal geometry, and the heat transfer is dependent on the interaction between the two fluid flows (through the HX metal), any approximations using the correlations mentioned above would result in significant errors. Therefore the stated HTC in the manufacturer's Datasheets are used. These are $885 \frac{\text{W}}{\text{m}^2 \cdot ^\circ\text{C}}$ for the condenser and $504 \frac{\text{W}}{\text{m}^2 \cdot ^\circ\text{C}}$ for the heat exchanger See appendix A, figures A.2 and A.3.

5.3. Void fraction

As discussed in chapter 3, the original model assumed a fully homogeneous flow. However, in reality there are always velocity differences between the fluids. The literature study [4] showed that for most coolants, these velocity differences can be large enough to have an effect on the liquid level in the accumulators and the transient behaviour of systems. However, the size and significance of this effect is unknown. Thus, non-homogeneous void fraction models will be included both to test the significance of errors introduced by the homogeneous flow assumption and to (potentially) provide in more accurate simulation results.

As explained in chapter 3.5, the model is based on a simplified subset of the one-dimensional time-dependent compressible Navier-Stokes equations. One of the foundations of these simplifications is the assumption of homogeneous flow. Thus, fully switching to a non-homogeneous flow model would mean that the basic equations of state in chapter 3.5.2 would have to be replaced by new derivations of the Navier-Stokes equations. Having not one, but two independent phase velocities would make these derivations and the resulting equations significantly more complex.

All other parameters in the simulation are directly derived from the results of these equations of state. Thus, any errors in these new derivations would make the entire model invalid. Additionally, even though the pressure drop and HTC equations are not directly dependant on the void fraction, any errors in the void fraction calculations would indirectly reduce the accuracy of all flow parameters. And most importantly, this complete rewrite of the model would likely take more time than is available during this thesis.

Based on these considerations, it was decided to try and implement the void fraction calculations by building upon the existing equations of state, instead of rewriting the whole code. This means that more time can be spent improving and building the tested-and-proven numerical simulation and it corresponds best with the research questions and goals laid out in chapter 3. The process of implementing the void fraction correlations in the numerical model is described in this section. During this process, several major problems were encountered, which will be further discussed in section 5.3.2

5.3.1. Implementation

As discussed in the introduction of this section, it was decided to continue building upon the existing homogeneous-flow basis of the numerical model, instead of completely rewriting it for non-homogeneous flows. Thus, a way must be found to define the individual single-phase velocities as a function of the homogeneous two-phase velocity that is defined by the equations of state. This means a framework needs to be defined, along which the homogeneous density and velocity can be related to the non-homogeneous single-phase ones.

The framework in this case is chosen to be the fixed volume of each element in the geometry. Additionally, the mass flow through each element will be used as the reference parameter to relate between the homogeneous and non-homogeneous equations. The mass flow is driven by the pump, and should therefore be unaffected by the void fraction in steady state conditions. But during the transient phases, different void fraction correlations are expected cause different fluctuations in the mass flow, thus causing different system responses. This is where a more accurate void fraction model is expected to increase the accuracy of the whole simulation.

The correlations found in the literature study [4] (shown in appendix B.3) were implemented in a new sub-function, similar to those for the frictional pressure drop and HTC described before. Next, the *CalcTimeLoop.m* function was extended so that the vapour volume fraction and single-phase velocities in each element will be (re-)calculated at the end of each time step.

Based on the reference frame described above, the single phase velocities are calculated using equations (5.7) and (5.8), where G is the mass flux, x the vapour mass fraction, ε the vapour volume fraction, and ρ_l and ρ_v are the local liquid and vapour densities, respectively. These single-phase velocities are not used anywhere else in the model, but might be relevant outputs of the program. Additionally, they can be used for debugging and the verification and validation process.

$$u_g = \frac{Gx}{\rho_v \varepsilon} \quad (5.7)$$

$$u_l = \frac{G(1-x)}{\rho_l(1-\varepsilon)} \quad (5.8)$$

As discussed earlier, the mass flow parameter was chosen as the 'interface' between the homogeneous and non-homogeneous parts of the model. The mass flow is defined as the product of the total flow velocity u_{tot} , the total density ρ_{tot} and the channel cross section A_c , as shown in equation (5.9). In order to make this equation dependant on the vapour volume fraction, the underlying definitions of the density and total velocity were changed.

$$G = u_{tot} \rho_{tot} A_c \quad (5.9)$$

$$\rho_{tot} = (1-\varepsilon)\rho_l + \varepsilon\rho_v \quad (5.10)$$

Instead of looking up the homogeneous total density in REFPROP, as described in chapter 3.5.2, the total volumetric density will be calculated from the single-phase densities and the vapour volume fraction, as shown in equation (5.10). Similar to the original implementation, these single-phase densities are found using the REFPROP database. This new value for the total density is then used to calculate the velocity and finally the velocity and density are used to calculate the mass flow using equation (5.9).

This implementation was designed such that, when the homogeneous void fraction correlation is selected, the output of all parameters is equal to the results from before this model adjustment. Therefore, when the homogeneous equation is chosen, the model performs exactly as it did before the void fraction correlations were added.

5.3.2. Issues

Multiple problems were encountered during the implementation and testing of the void fraction models. Some of these were encountered early and could be solved or circumvented immediately, but others persisted all the way to the end of the verification and validation phases.

The Woldesemayat & Ghajar correlation could not be successfully implemented. This model uses the inclination angle of the flow (the angle of the tubing relative to the horizontal plane) as one of its

scaling parameters. Initially this could be (partially) implemented, as the flow direction in each element, from which an angle can be derived, is specified in the geometry file. However, after the simplification of the geometry described in section 4.3, this does no longer accurately represent the actual inclination of the tubing. Additionally, the complex geometry of the plate heat exchangers and the simplified way in which these are implemented also make it difficult to determine the actual inclination of the flow. Therefore, it was decided to leave this correlation out of the final model.

A relatively simple error in the code was found during the verification of the model. As explained in chapter 3.5.2 and illustrated in figure 3.3, the density is calculated twice. A first time between the MacCormac predictor- and corrector steps and a second time after the corrected enthalpy is found. However, during implementation, only the second iteration was replaced with method discussed in this chapter. Chapter 7.3 will explain how this error was found and what influence it had on the model and the research.

Another, much more fundamental, mistake was uncovered during the final stages of the validation process. At this point, it was found that the steady-state pressure drop between the homogeneous and non-homogeneous correlations differed significantly. This should not be the case and indicates a flaw in the implementation, as will be described described in chapter 8.5. The total volumetric density, which is used to calculate the gravitational and minor pressure drop, amongst other things, was found to differ significantly between the homogeneous and non-homogeneous versions, causing these large offsets. Thus, either the definition for volumetric density must be changed, or the other functions must be changed to use other variables. At this point in the project however, there was no time left to perform these adjustments, it was decided to abandon the attempts to include the void fraction and focus on validating the rest of the model instead.

6

Experimental setup

To prepare the demonstrator setup, described in section 3.4, for the verification testing, several actions were taken. First, adjustments and improvements were made to both the hardware and the control software, as described in sections 6.1 and 6.2, respectively. Next, section 6.3 will describe a series of experiments that were performed to test the functionality of the system and to calibrate some input parameters. Finally the test plan will be presented in section 6.4.

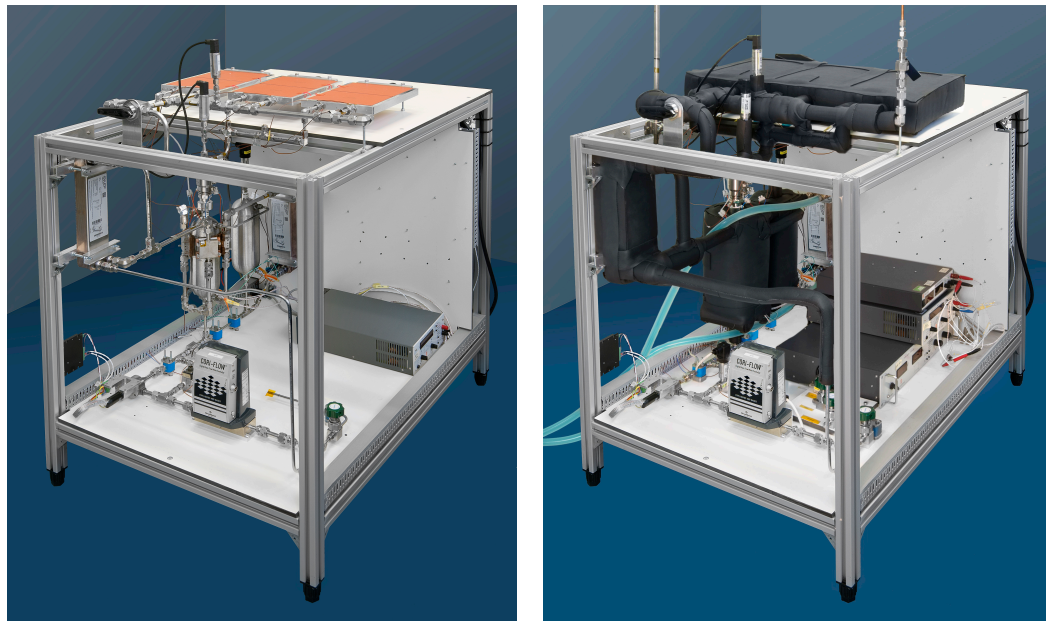
6.1. Hardware adjustments

In addition to the temperature sensors already present, four more were added. These were placed on the second accumulator vessel, one on the inlet/outlet tube of each accumulator vessel and the final one on the pump inlet.

The extra sensors on the accumulators were placed in an attempt to gain better knowledge on the performance of the accumulators. Since the Peltier cooling elements are mounted on the outside of the first accumulator vessel, they influence the temperature measured on the outside of this vessel (where the original sensor was placed). The second accumulator is not cooled, therefore the temperature measured on the outside of this vessel is expected to more accurately represent the fluid temperature on the inside. The sensors on the in/outlet tubes of the accumulators were placed in an attempt to analyse the flow direction, as will be discussed in section 7.1.

Afterwards, the complete two-phase part of the loop was insulated using Armaflex foam. This includes all components from the heat exchanger to the condenser and the two accumulators. It was decided not to insulate the single-phase portion of the loop for multiple reasons (condenser outlet, pump, mass flow meter, up to heat exchanger). First off, the temperature difference between the single phase fluid with the external temperature is relatively low (in the order of 5 °C), thus the expected amount of heat leak from the environment to the fluid is expected to be very limited. Secondly, single-phase fluid tubing is clamped and connected to the chassis in multiple locations, as is the pump and mass flow sensor. This means that most of the heat leak will be caused by conductive heat transfer through these clamps and connections, instead of convective heat transfer with the surrounding air (which would be limited by the insulating foam). Finally, the heat sink is provided by water circulation cooler, set at 15 °C, located in an adjacent room. The inaccuracies in this system, added to the thermal influence on the tubes connecting it to the condenser, the conductive coupling with the chassis and any other heat leaks mean that it is not worth the effort and materials required to fully insulate this part of the system.

After several tests, it was found that the thermostatic bath could not handle sufficiently high heat loads to allow the two-phase demonstrator to run at high vapour mass fractions. Therefore, cold tapwater (at around 15 °C) was used as a pre-chiller in what essentially formed a tertiary open-loop system. A small heat exchanger was placed between the condenser outlet and the thermostatic bath, exchanging heat from the (closed) secondary loop to the tapwater. This system was only used when the evaporator input power rose above 2000W.



(a) Without insulation

(b) After insulation is applied

Figure 6.1: Comparison between the demonstrator setup before and after installing insulation

6.2. Software adjustments

The software changes focused mainly on adding control functionality. The implementation of these changes was performed by Mr Gerrit van Donk. The two most important improvements were the ability to select which pressure sensor to use as the main control input and the option to switch the accumulator cooling control from PID to constant power. This last option was needed since the numerical simulation is not (currently) able to accurately simulate the Peltier behaviour. It was therefore decided to implement a constant cooling power instead of unnecessarily complicating the model.

The measured system pressure is used as the main temperature control variable. While it may seem strange to control temperature by measuring the pressure, it actually provides more accurate results. The temperature sensors in this system are all located on the outside of the hardware. This means that the thermal mass of the tube walls and the outside environment influence the temperature measurements, resulting in reduced accuracy. The pressure, on the other hand, is measured directly and results in much more accurate measurements.

Pressure and saturation temperature are directly related through well-documented curves in the REFPROP database [29], so the measured pressure can easily be converted into two-phase temperature by the control software. Not only does this provide very accurate control data, it also simplifies the start-up phase. The system will automatically regulate the pressure to the saturation pressure corresponding to the set-point temperature, even though the fluid is still fully liquid.

Originally the accumulator pressure was used as the control input. However, since controlling the temperature of the (potential) hardware mounted to the evaporators is the objective, the evaporator outlet pressure would be a better control parameter. These two pressures are similar, but the pressure drop between the evaporator and accumulator creates a pressure difference that can increase with increased input power and flow speed, thus causing fluctuating temperature offsets in the evaporator if the accumulator is chosen as control input.

6.3. Calibration

After the upgrades were performed a series of tests and calibrations was performed on the completed demonstrator setup to prepare for the upcoming numerical model validation and verification.

Accumulator level The accumulator level sensor was calibrated by using an ultrasonic measurement device and a ruler. Using the ultrasonic sensor on the outside of the accumulator vessel, the location

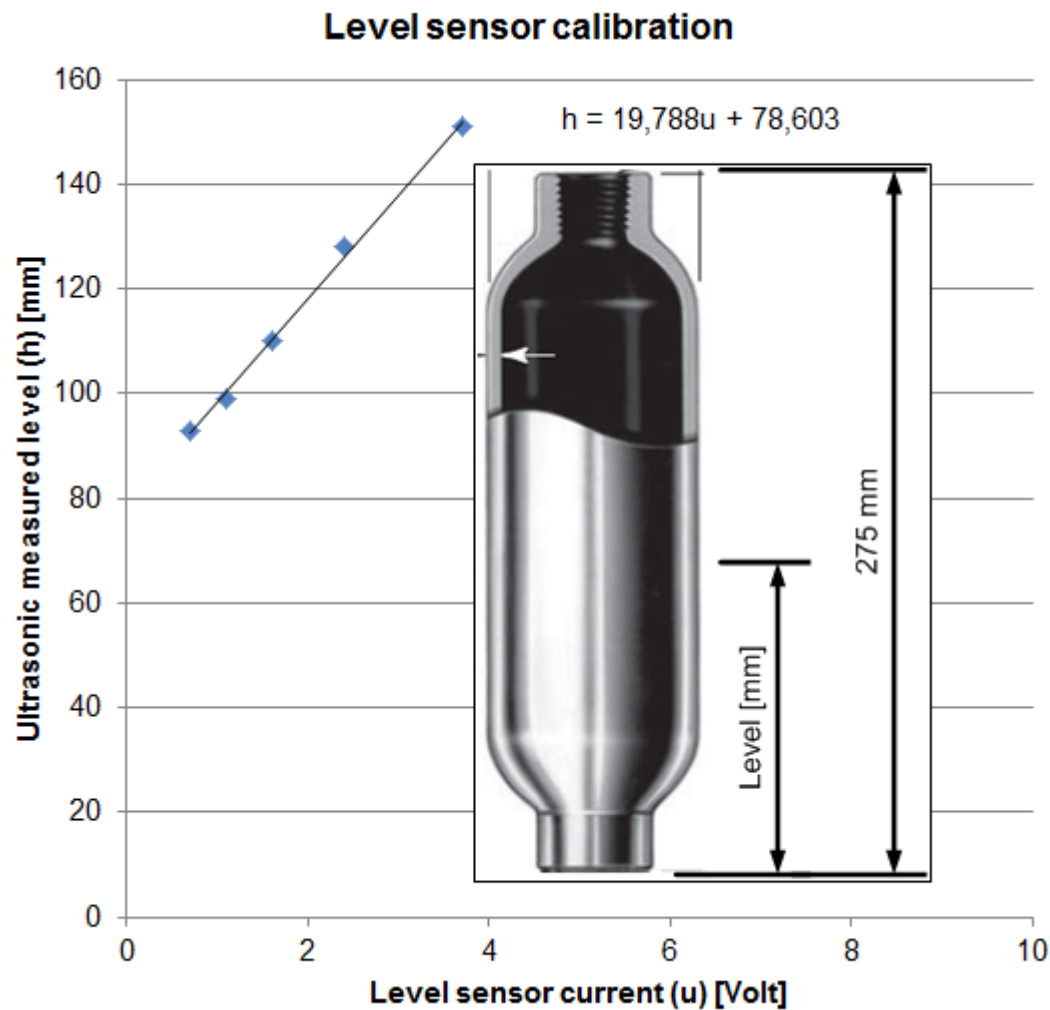


Figure 6.2: Calibration of the accumulator level sensor as performed by Van Donk, NLR (figure from Swagelok [33])

of the liquid surface was approximated and marked by hand. The distance between the bottom of the accumulator vessel and this mark was measured using a ruler and the voltage produced by the internal liquid level sensor was noted down. This experiment was repeated several times under different system operating conditions, resulting in a list of liquid levels and corresponding sensor voltage outputs. A simple linear trend line was found using Microsoft Excel and implemented in the data acquisition software.

Mass flow and Temperature setpoint To limit the scope of the final model verification, a single mass flow and temperature setpoint were chosen. The mass flow must be sufficiently high to allow large heat transport and create a measurable frictional pressure drop, while comfortably remaining within the performance boundaries of the pump and the mass flow meter. After some experimental tests, it was found that 15 gram per second, together with the chosen temperature setpoint, allows for high heat loads (approaching the limits of the heaters), while a higher mass flows the pump would start hitting its performance ceiling.

The temperature setpoint is limited by a larger set of constraints. First of all, the evaporator hardware has a maximum operating pressure of 10 bar [34]. To protect these expensive components, a 10 bar burst valve is implemented and the control software is programmed to shut down if pressure exceeds 9 bar. For R134a, 9 bar correlates with a saturation temperature of 35.5 °C.

The thermal bath used as heat sink for the secondary cooling loop works most efficiently at around 15 °C, meaning that it can remove the most heat at this temperature, around 2000 W according to its

specifications. Since the pump requires a significant amount of subcooling, the setpoint temperature should be as close to the maximum of 35.5 °C as possible.

Initially 35 °C was chosen, corresponding to 8.87 bar. However, tests with changing heat inputs showed that the transient responses caused pressure fluctuations large enough to surpass 9 bar and trigger the safety shutdown. Therefore a slightly lower temperature of 33 °C (8.39 bar) was chosen as setpoint.

Input power The research objective is to develop a model that can accurately predict the transient responses to changing heat input, thus a series of heat input settings need to be chosen for testing.

It would seem logical to start with 0 W as the minimum input power. However, that would mean that no liquid is evaporated and the fluid temperature would eventually reach a steady state at 15 °C (the setpoint temperature of the thermostatic bath). In other words, the system is not performing its main function (maintaining a specific temperature using two-phase flow). Therefore, system start-up (going from subcooled liquid-only state to two-phase flow at setpoint temperature) is not a case studied for model verification. The minimum input power is set at 100 W per evaporator.

To validate the operational range of the numerical model, the most extreme cases of the experimental setup are considered. The maximum power input is limited by the thermostatic bath used to cool the condenser. According to its specifications, this should be around 2000 W. Tests with 2100 W and 1800 W (3x700 W and 3x600 W respectively) showed that the external chiller was actually unable to reach its stated performance (probably due to its age), so the maximum power input was set at 1500 W (3x500 W).

As described at the end of section 6.1, extra cooling capacity was added to the secondary system by implementing a tapwater heat exchanger. This allows to increase the maximum power to 2100 W, but since the verification phase was already underway by this time, it was decided to keep 300 W and 1500 W as the main power settings for comparison.

For the final verification phase, 2100 W and 900 W (3x300 W) will also be used to test transient responses to 'extreme' power input and the effect of smaller steps in power change.

Accumulator control settings In the demonstrator setup, the accumulator heaters and Peltier coolers can be controlled through two separate PID control loops, each with their own sets of gains. Numerical implementation of the heaters is straightforward. It is assumed that all the electrical power used by the heaters goes directly in the accumulator liquid. The amount of heat transported by the Peltiers, however, is influenced by the so-called 'Peltier Coefficient'. This coefficient is very specific to the Peltier element itself and the environment it is operating in. Moreover, it is not a single value or linear relation, but follows an unknown curve. Proper numerical implementation would require a period of extensive testing and calibration.

Instead, the Peltier input current was kept constant at 2 A. The assumption is made that this will result in a constant 'cooling power'. At each of the power input settings described above, the accumulator heaters drew between 95W and 105W of power to keep the system in steady-state. The Peltiers needed around 25 V, of 50 W of power. Therefore, the accumulator cooling power is set at 100 W in the numerical model, while 37.5 W (150 W /4) of power is dissipated through each of the Peltier heat exchangers. The maximum accumulator heating power is set at 200 W. This is twice the cooling power, so with a constant cooling, the system has the same heating and cooling potential

Finally, the PID control gains of the accumulator heaters are selected. Since this tuning is done manually, it was decided to drop the derivative term as it makes tuning much more difficult. After a series of empirical tests, the best combination of parameters was found to be $K_p = 20$; $\tau_i = 6$, where K_p denotes the stiffness of the proportional term and τ_i the time constant for the integration step.

System fill level The system was initially filled with R134a by Mr. Gerrit van Donk. To fill the system, a tank of pressurised R134a was connected to a valve on the demonstrator setup and the pressure inside the tank was used to force the refrigerant into the system. The setup was cooled in several places to keep the fluid condensed and reduce the amount of back-pressure. The required amount of fluid was estimated by Mr. van Donk based on the approximate internal volume and his experience with similar systems. The fill level was controlled by placing the pressure vessel with R134a on a digital scale and controlling the valve until the desired fluid mass had left the vessel (and entered the demonstrator setup).

After the initial filling, a series of tests was performed to fine-tune the fill level. Experiments were done around the expected set points and the responses of the system were analysed. If the heaters inside the accumulators started overheating, it meant that the amount of fluid was too low and the heaters were 'standing dry'. On the other hand, too much fluid would mean that the accumulators were overfull and small increases in heat input would lead to drastic pressure rise. Thus, small amounts of fluid were added or bled off until a good balance was struck.

The disadvantage of this unscientific approach is that the exact fluid mass inside the demonstrator is unknown and must therefore be approximated for implementation in the numeric model. Another challenge is that the model always starts a new simulation at the heat sink temperature (15 °C in this case). The 'initial fill level' value that needs to be put into the simulation is therefore the liquid height in the accumulator in case the whole system is at this sink temperature. This is a boundary case that is never reached in reality, so it can not be measured directly.

Instead, the initial fill level was calibrated iteratively by running a series of experiments and simulations, comparing the results and adjusting the value of the initial fill level input until the resulting accumulator liquid levels of the simulation and the experiment matched up. The initial fill level in the simulation is implemented as the initial vapour *volume* fraction in the accumulators. The value that gave the best correlation between experiments and simulation was 0.7 (70% of the total volume).

Note that this is the only instance where one could say the model was '*tuned*'. In this step, special care was taken not to tune the fill level to one particular set of correlations as that would invalidate all final conclusions of this research project. Moreover, this calibration is done before the verification and validation phases, so it is not known yet if the results of the correlations can be trusted. And finally, this numerical model is built primarily to test rough estimates in the initial design steps of two-phase systems, when precise values are not yet available. In other words, the model should be able to produce valid results, independent of the accuracy of the input instead of having a very narrow bandwidth. Therefore, this calibration, or '*tuning*', was done by just comparing the graphs and adjusting the value by 0.05 at a time, leading to the final result of 0.7 mentioned above.

6.4. Test plan and procedures

The demonstrator setup that was described in chapter 3.4 is connected to a computer for control and data acquisition. This computer runs a LabView environment that was built by Van Donk that contains a control (input) panel, a monitoring screen and data acquisition and logging functionality. This program allows easy centralised control and monitoring of the whole system and also allows the user to pre-program test profiles and control inputs for automated control.

The calibration steps presented above did not follow specific test plans. Instead, the relevant parameters were adjusted manually until the required conditions were met. For the actual measurements, a small test plan was written, although it still remains relatively straightforward.

For all of the verification and validation tests, a simple simulation procedure is developed, so that the results of different tests can easily be compared. In this procedure all tests and simulations will cover a time span of exactly 10 minutes. During this time span, all parameters will remain the same, except for the evaporator input power, which will be changed once. This change will be in the form of a 'step function', instantaneously switching the power from the initial to the final power setting, at exactly 100 s after the start of the measurement. This allows comparison of the initial steady state values, and 500 seconds after the step change, covering the immediate transient responses.

In reality, the experimental measurements will have much larger time spans between measurements in order to allow the flow to fully stabilise before the next experiment is run. Similarly, the numerical simulations will span an extra 5 to 10 minutes before and after each simulation run to ensure the conditions are fully steady-state at the start of each comparison. These 'lead times' will not be shown in the comparisons, in order to make the plots clearer and focus on the most important parts.

The first two measurements are the reference baselines defined previously in the "Input power" section of this chapter. That means one for the step from 300 W to 1500 W heater input power and one for the reverse. The results of these two measurements will be used for most of the comparisons in the next two chapters. To perform this test, the system was started up and all the input parameters were checked and double checked to those selected in this chapter, summarised in table 6.1. Next, the three evaporator heaters are supplied with 100W each and the system is left running until a steady state is reached.

Table 6.1: Base control settings for experimental setup

Parameter	Evaporator temp.	Mass flow	Peltier current	Max. Accu heater power	K_p	τ_i
Value	33 C°	15 g/s	2 A	200 W	20 W/K	6 s

At this point a new measurement log file is initialised and the first 'automatic' program is started. This program waits for another 300 seconds, before it increases the power on each of the evaporators to 500 W simultaneously. Then, it waits another 1000 s before it is 'done'. Next, the operator looks at the graphs on the monitoring panel and waits another few minutes until it looks like all parameters have remained roughly stable around a constant value for several minutes (due to inherent noise in the measurements, it is difficult to exactly define the steady states). When the operator is confident that a steady state has been reached, a new program is started that waits another 500 seconds before switching the input power on all panels back to 100 W each. This ensures that the flow is truly stable at the start of the step function. After another 1000 seconds of measurement, the power is reduced to zero and the system is shut down.

For the final model validation, more data is required. Therefore more measurements will need to be performed. To do this, all of the power levels discussed in the "Input power" section of this chapter will be evaluated including the effect of the step changes between each of them. The full list of all twelve experiments can be found in table 6.2. These experiments are conducted in the same manner as the two before. Moreover, the two 'baseline' measurements are included in this second set of experiments for redundancy and for cross-comparison. All of these measurements are performed back-to-back during a single session in order to avoid errors limit external influences, such as changes in the experimental setup and variations in the environmental temperature. All the raw measurement data will be time-synchronised and saved in a single database for further analysis.

Table 6.2: Start- and end power settings for each of the 12 final validation experiments

300-900 W	900-300 W	900-1500 W	1500-900 W	1500-2100W	2100-1500 W
300-1500 W	1500-300 W	900-2100 W	2100-900 W		
300-2100 W	2100-300 W				

The numerical simulations will be run in a similar fashion as the experimental ones, where the actual simulations span a larger time frame than the selected window for comparison. A MATLAB program will be used to load and synchronise both the experimental and numerical data sets and make these comparisons. This program will look for the step function in the power input in both data sets, synchronise them and crop the data to the selected measurement window of 10 minutes.

In the next chapters the verification and validation process will be described. The verification is first in chapter 7. Here it will be determined if the model itself works as expected after the additions and adjustments from chapter 5 have been implemented. In the verification chapter, all issues that are encountered will be discussed, as well as how they are resolved. While the chapter mainly focuses on the verification of the numerical model, any unexpected results in the experimental measurements will also be discussed here.

The validation in chapter 8 encompasses the final step of this research project; Finding which of the correlations work best and determining the accuracy of numerical model, which will be the final product of this thesis. In order to do that, the results of the numerical simulations will finally be compared to the measurement data. This will be done in two steps. First a large number of possible correlations will be compared along the 'baseline' experiments (300 W - 1500 W and vice versa). And once the results have been analysed and the best set of correlations has been selected, the numerical results of this final set will be tested against the full range of measurements described in table 6.2.

7

Testing and verification

Once all correlations are implemented and all fatal errors are filtered out, the verification process starts. A series of tests is run on both the numerical model and the demonstrator setup. The results are analysed separately and run through a 'sanity check' to find any obvious implementation errors and unexpected behaviour. The different problems that were encountered during this process will be discussed below. After these last bugs have been filtered out, the model validation can start as described in chapter 8.

The first section of this chapter will describe some unexpected behaviour in the experimental setup, in particular the difference in temperature between the two accumulator vessels that was measured. The rest of the sections will focus on the behaviour of the numerical model. First of these are the flow reversals that cause the simulation to crash on occasion, which will be described in section 7.2. Next, the performance of the void fraction simulations will be described in section 7.3. Section 7.4 similarly analyses the performance of the heat transfer coefficient correlations and finally the overall discretisation errors are checked by determining the amount of mass that is lost or created during each time step in section 7.5.

7.1. Accumulator temperatures

The experimental measurements revealed that there were significant differences between the inlet temperatures of both accumulator vessels. Figure 7.2a shows the temperatures measured by the four sensors around the accumulators over the duration of a complete experiment series. It is interesting to see that during the periods of steady-state, the inlet temperature of vessel 2, which is closest to the condenser, trends towards that of the surrounding flow (from condenser to pump), while the inlet temperature of vessel 1 rises to the accumulator temperature.

This seems to indicate that in steady state, cold fluid is constantly flowing into accumulator vessel 2, while warm fluid is flowing out of vessel 1. A logical explanation is the lack of cooling in accumulator 2. Some amount of liquid is continuously evaporated in vessel 2, travels between the accumulator vessels through the connecting tube at the top, and condenses in vessel 1, creating a net inflow in vessel 1 and a net outflow from vessel 2. A simple drawing, illustrating this process is given in figure 7.1.

In figure 7.2b, the temperatures of the accumulator inlet tubes are compared to the changes of the liquid level in accumulator 1. The change in liquid level is found by subtracting the measured liquid level from the level measured a second earlier. The results were run through MATLAB's built-in Savitzky-Golay filter to filter out the measurement noise. The resulting plot shows that whenever the level sensor indicates a large rise in liquid level, the inlet temperatures of both accumulator vessels decrease, corresponding to a significant amount of cold fluid flowing in. Sharp decreases in liquid level correspond with rises in accumulator outlet temperatures, caused by warm fluid flowing out of the accumulator.

These measurements show that the sensors work as expected, but that some of the actual workings of the dual accumulator setup go beyond the capabilities of the numerical model. The model currently treats the two accumulators as a single entity with regards to heat control and mass in- or outflow. For the liquid level calculations the volumes and mass flows are simply divided by two.

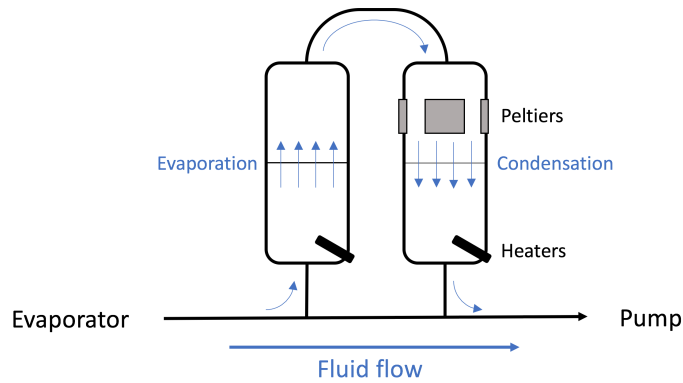
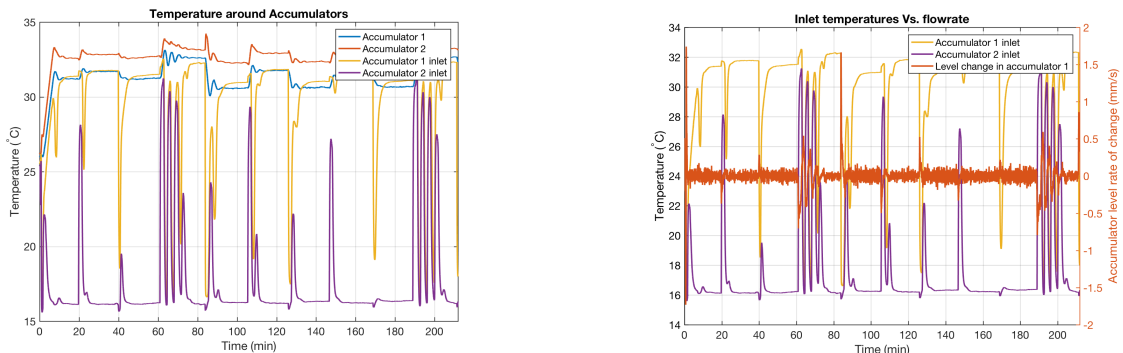


Figure 7.1: A simple drawing, showing the fluid flow interaction between the two accumulator vessels.



(a) Temperatures measured by the four sensors on the accumulators

(b) Comparison of inlet temperatures to changes in accumulator liquid level

Figure 7.2: Analysis of temperature measurements around the accumulators

The effect of hot fluid constantly flowing out of accumulator 2 means that the efficiency of the heaters is slightly decreased (or the cooling capacity slightly increased by the cold fluid flowing into vessel 1, depending on how you look at it). But this effect is already covered by the calibration done in chapter 6.3. Another consequence is that there might be a small difference in the liquid levels between the two vessels, due to them not being in perfect equilibrium. But the difference can only be very minimal and would fall well within the error margin of the measurements. Therefore, the liquid level measurements can be used directly for model validation purposes. Further analysis of the behaviour and interaction between the individual accumulator vessels is needed to fully understand its effect on the overall accumulator performance, but that goes beyond the scope of this thesis.

7.2. Negative flow velocity

Throughout the project, the most frequently encountered errors were caused by reversed flow. In some cases the simulated fluid flow would reverse direction, resulting in a negative value for the fluid velocity. This negative value caused a cascade of errors throughout the rest of the simulation before a 'fatal error' would occur that broke off the simulation.

It is technically possible for the flow direction to reverse in certain parts of the system under specific circumstances. The most likely case is when there is a relatively low pump speed and the heat input on the evaporator has a significant decrease. This means that the vapour mass fraction at the evaporator exit will decrease rapidly, leading to a very quick pressure drop. If this effect happens fast enough, it is possible that the sudden pressure drop can cause a local minimum significant enough that fluid further along in the tubing (at the end of the evaporator or the beginning of the tube leading out of it) will reverse direction due to the negative pressure potential.

While theoretically possible, it is unlikely to happen in practice. The thermal mass of the evaporator

will dampen the effects of changing heat inputs and the changes in power are not expected to be large enough to cause this effect. Therefore, the fact that these errors were occurring so regularly must mean that there were flaws in the code.

The code was checked multiple times, but no errors could be found in the equations or the implementation in the code that could cause this. Extensive testing showed that the negative flow errors would occur consistently with several of the void fraction equations as well as the Kim & Mudawar HTC correlation.

7.2.1. Implications

Under different conditions, the fatal errors would either show up in one of the REFPROP function calls or one of the interpolation functions (used for parameter table lookups). These cascading errors made it difficult to identify the root causes, which were finally found to be caused by diverging oscillations in the flow. Since the program is not set up to properly deal with these kind of negative values, they cause errors. Many frictional pressure drop correlations take a root of the velocity, resulting in complex numbers in their solutions. These are not only physically incorrect, but also incompatible with the REFPROP and other table-lookup functions used in other parts of the simulation, leading to the fatal errors.

Another problem is that many of the underlying principles of the simulation depend on the assumption that the simulation is marching forward along the velocity direction. When the flow changes direction, this assumption becomes invalid, causing additional inaccuracies. It was considered to rewrite all the functions that depend on the flow velocity to use only absolute velocity, store the direction in a separate parameter and adjust the outcomes according to the flow direction.

This idea was rejected because it would not solve the root cause of the errors, but only its symptoms. Moreover, it would violate the underlying model assumptions and singularities would occur at the points where the flow velocity is exactly zero. It was therefore considered more time-efficient to find the reason for the flow reversals instead of rewriting and debugging a large portion of the existing code. Sadly, as stated before, this underlying reason could not be found in the allotted time.

7.2.2. Solution

Since the exact cause is unknown, a real solution could not be formulated. The best option is therefore to ignore the correlations that seem to cause negative flow and only use the correlations that do not cause errors. This is of course not a perfect approach, as an underlying model or code error, and therefore a flaw in the simulation, cannot be ruled out with absolute certainty. Verification of the model must therefore continue with the following assumption:

- The negative flow errors are assumed to be caused solely by problems with the implementation of the individual correlations for which these errors occur and are not the result of a larger underlying flaw in the model architecture.

7.2.3. Potential cause

While the true cause of the negative flow could not be determined with absolute certainty, a hypothesis was developed during the report-writing phase. The tests showed that the point of negative flow incipience was usually preceded by a strong oscillation in flow velocities, diverging to the point at which the flow becomes (locally) negative. These instabilities occur immediately after the input power on the evaporators is changed. However, it is still unknown what the exact causes are for these oscillations and the eventual flow reversal. The most likely cause is the discontinuities when transitioning between correlations.

Take for example the frictional pressure drop: When the vapour mass fraction is lower than 0.1%, the flow is considered fully liquid and the liquid-only friction factor is used. However, when the amount of vapour rises above that fraction, the pressure drop will be calculated using the two-phase correlations instead, causing a small jump or discontinuity. Additionally, when using the Lockhart & Martinelli or Kim & Mudawar correlations, and part of the flow transitions between laminar and turbulent, there will be another discontinuity as different equations or multipliers are used in these cases. The same applies to the heat transfer and void fraction correlations.

It is theorised that these discontinuities contribute to the oscillations that eventually cause the simulated flow to reverse direction. The problem of discontinuities is well known for single-phase

flows. As explained in section 5.1.3, the NLR uses a specific smoothing curve for the transition between the laminar flow and turbulent flow in the single-phase friction factor correlations. For the two-phase friction correlations, however, such smoothing functions could not be found in literature.

At this point in the thesis project, it was deemed too late and too time consuming to start developing and implementing a new set of smoothing functions. Research, development, implementation, testing, and tuning of such a set of functions would take several months at least. Moreover, since it is unknown whether resolving these discontinuities would solve the 'negative flow' problem, it was decided not to invest the time at this point.

7.3. Void fraction

The void fraction is implemented as described in section 5.3. During test runs, the simulated steady-state vapour mass fraction values were different for each correlation, under identical conditions. In reality, only the vapour *volume* fraction should change between correlations, while the vapour *mass* fraction should remain constant under identical steady-state conditions, as explained in section 5.3.

$$x = \frac{P}{c_{l,@33^{\circ}\text{C}} \cdot m} = \frac{1500 \text{ W}}{170.16 \frac{\text{J}}{\text{g}} \cdot 15 \frac{\text{g}}{\text{s}}} = 0.588 \quad (7.1)$$

Equation (7.1) shows that when 1500 W of heat is applied, the vapour mass fraction should be just below 0.6. Figure 7.3 shows that when the simulations are run for the heat input increase from 300 W to 1500 W, (keeping all other parameters the same: Gungor-Winterton HTC, Xu & Fang frictional pressure drop) only the homogeneous and Smith void fraction models produce results that align with the calculated vapour mass fraction. Thus, it shows that there must be a fundamental error in the implementation of the void fraction.

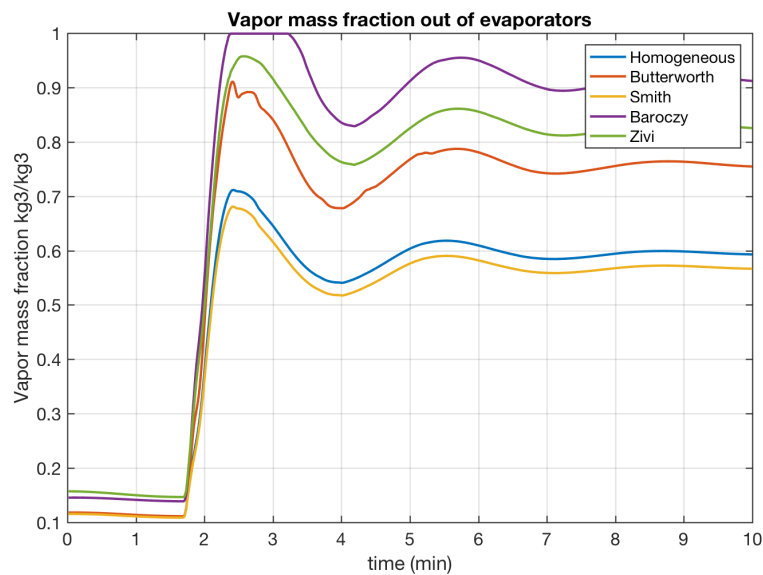


Figure 7.3: Simulated vapor mass fractions using different void fraction correlations

It took a while to find the cause of these errors. However, initial comparisons with measurement data did show that the results using the homogeneous flow assumption seemed to be quite accurate, more so than was initially expected. It was therefore decided to move forward with the verification phase in the meantime, using only the homogeneous flow. As explained in 5.3, use of the void fraction models is expected to lead to more accurate simulation of the transient responses and the accumulator liquid level, but their exclusion should not negatively influence the performance of any other parts of the correlation.

7.3.1. Error found

At the end of the verification phase, an error was found in the implementation of the void fraction into the mathematical basis of the model, as described in chapter 5.3. As explained in this chapter, part of the implementation process involved changing the equation that is used to calculate the fluid densities in the model. However, a mistake was made. While the density has to (re)calculated twice per time step, the changes were only applied to the second calculation, causing incorrect results.

This error was found and corrected at the end of the verification process. Further testing, however, showed that the majority of the correlations now produce negative flow. Only the Homogeneous and Baroczy correlations are able to run successfully. Figure 7.4 shows that after the adjustments, the steady state portions of both graphs now overlap and the values match with those produced by the experimental setup. Note that the void fraction values from the experimental setup are not directly measured, but the result of a calculation based on the pressure, mass flow and amount of heat input and can therefore only be used as an indication.

At this point, the rest of the project was already moving along through the validation phase. Since the Baroczy correlation now at least provided accurate vapour mass fraction values, it was decided to see what the effect of this void fraction correlation would be on the results. Assuming that this was the only error in the code, the void fraction correlation is still expected to make the simulation more accurate. Sadly, another implementation error was found during this process, as will be discussed in section 8.5.

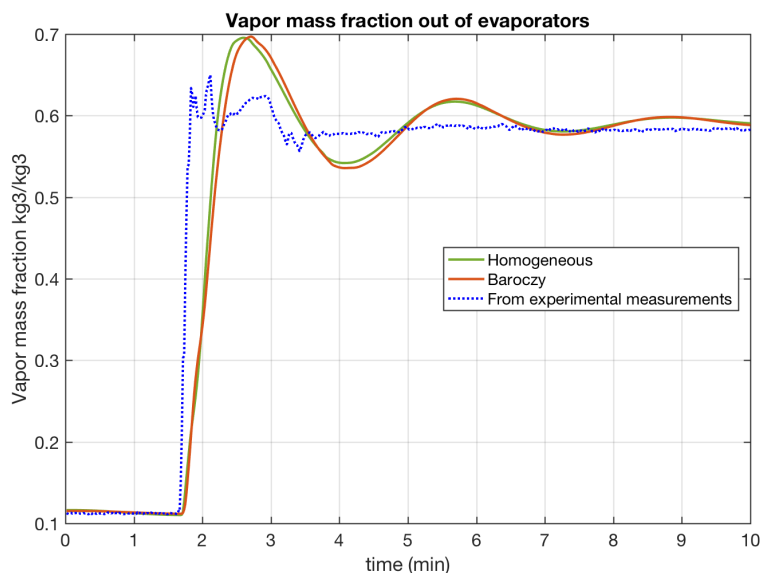


Figure 7.4: Comparison of the vapour mass fraction predicted by the Homogeneous and Baroczy void fraction correlations with the (calculated) experimental results.

7.4. Heat transfer coefficient

The three selected correlations for the heat transfer coefficient were tested under a series of different circumstances. The Kim & Mudawar has to be ruled out immediately, since it consistently leads to negative flow errors. Investigation showed no errors in the implementation. However, as noted in section 5.2, the dryout incipience was not included in the simulation, as there is no model readily available for the HTC behaviour during the stages of (partial) dryout. It is expected that this causes larger error margins at higher heat loads and vapour mass fractions, by overestimating the local HTC. This could be causing instabilities, leading to the negative flow conditions.

Experiments with the Fang R134a lead to strange results. It appeared that the transient reactions were extremely slow, much slower than expected and than the other correlations seemed to suggest. Further investigation showed that this equation in the simulation produced significantly lower HTC values than expected, which were indeed much lower than those produced by the Gungor-Winterton and Kim & Mudawar (before negative flow occurred). The most likely cause of the under-performance

of this equation is the fact that it requires two distinct dynamic viscosity values. As explained in chapter 5.2.1, the correlation requires values for both the liquid viscosity at the inner wall surface temperature and the mean fluid temperature. Since this is a one-dimensional model, these values are not defined separately and therefore assumed to be equal to each other.

Clearly this assumption is not valid. On the other hand, in a boiling flow, the bulk fluid temperature is expected to be at saturation temperature, while the wall is at a higher temperature. It is therefore impossible to define the *liquid* viscosity of the fluid at the local pressure and wall temperature, as required per Fang's paper [15], since the fluid should be fully evaporated at this point *above* the saturation temperature. A solution could not be found, and therefore the Fang correlation was scrapped as well.

Thus only the Gungor-Winterton equation remains. The initial tests show that this model performs reliably and the results are within the expected range. Considering the expected effort required to developing a remedy for the other two correlations, it was decided to continue with only the Gungor-Winterton equation in place. The performance and accuracy of this correlation will be tested and discussed further during the validation.

7.5. Conservation of mass

A numerical simulation method using discrete time steps and a series of fixed points, like the one employed in this project, has the disadvantage that it will always lead to discretisation errors. One important factor is the total fluid mass in the system. Due to small changes in velocity and density between nodes and between time steps, a small amount of mass can be 'lost' or 'created' throughout the simulation.

The total fluid mass in the system is calculated by the numeric model at the very start of the first simulation. Assuming the initial vapour volume fraction of 0.7 in the accumulator, the simulation consistently predicts that there is 2.5084 kg of R134a in the system. As described in section 6.3, the exact fluid mass in the system is not known, but after the tuning described there, this value is expected to be relatively accurate.

At the end of each time step, the fluid mass in the system is recalculated based on the predicted fluid masses in each element. This value is compared to the original mass and any offset is compensated by adding or removing that amount of fluid in the accumulator. This ensures that the total mass in the system will remain constant over time and the size of the error does not accumulate over time. These offsets, called the 'mass error' are also saved in a vector for future reference.

Figure 7.5 shows the size of the mass errors during a series of simulation runs with the different pressure drop equations. These simulations predict the behaviour of the system going from 300W to 1500W input power (similar to the simulations in figure 7.3). All these simulations are run under identical circumstances, using the homogeneous flow assumption and Gungor-Winterton HTC correlation.

As can be seen in figure 7.5, the maximum total mass error per time step is below 0.033 gram in this case and on average only about one tenth that size. Compared to the total fluid mass of 2.5 kg and the mass flow of 15 g/s, this value is small enough to be considered negligible.

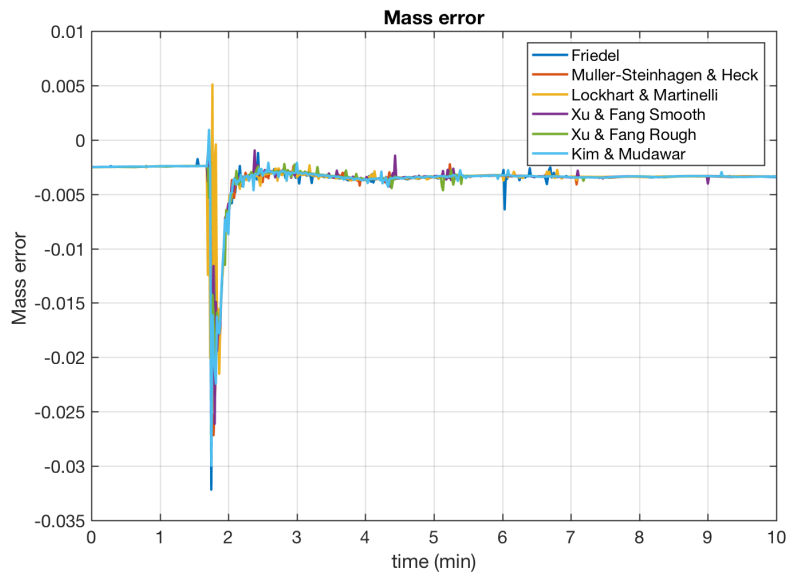


Figure 7.5: Error in calculated mass produced by the different two-phase pressure drop correlations

8

Model performance and validation

As the goal of this research project is to develop a working simulation model, the validation step is the final and most important step in the process. In this chapter, the results of the numerical simulation will be compared to the measurements obtained from the experimental setup. The accuracy and deviations between the modeled and measured results in different sections of the setup will be presented and discussed. Finally the best (combination of) correlations will be selected and the final accuracy of the numerical model simulations will be discussed.

8.1. Method of validation

The Mean Absolute Percentage Error (MAPE) is used to compare and decide whether the results fall within the 30% error bounds set out in the research questions. As illustrated in equation 8.1, the MAPE takes the absolute difference between the measured (M) and simulated (S) value in each time step and divides that by the measured value to get the absolute relative deviation. By summing these deviations over the entire period and dividing by the number of time steps, the mean is found and multiplication by 100 results in the percentage.

$$\text{MAPE} = \frac{100\%}{n} \sum_{i=1}^n \frac{|M_i - S_i|}{M_i} \quad (8.1)$$

In order to find the best configuration, or combination of correlations, these configurations must first be defined. Since a singular HTC equation remains after the previous chapter and it was decided to start the verification using the homogeneous flow assumption, only the different friction correlations remain to be tested. In most cases, there are different equations for the different flow phases. In the literature study [4], the Haaland friction factor was selected for the liquid-only flow, but there are different combinations of correlations for the two-phase flow. These combinations are shown in table 8.1.

As mentioned before, the homogeneous flow assumption is used, together with the Gungor-Winterton HTC correlation and the Haaland equation for all liquid-only flow. The two-phase flow can be differentiated into three different conditions: Evaporating flow, adiabatic two-phase flow and condensing flow. Since not all equations are suited for each condition, different combinations had to be selected. For each condition a combination of single-phase friction factor ($1-\phi$ ff) and two-phase multiplier ($2-\phi$ multi) had to be chosen.

The first three correlations of table 8.1 are older, well established models which were all initially developed for adiabatic flow, but regularly used for evaporating and condensing flows as well [1, 4, 11, 13]. The Kim and Mudawar model consists of a series of equations for different conditions. The numerical model automatically selects the appropriate ones for the specific local fluid conditions in each element. These work with the Blasius and Incropera equations for low and high Reynolds numbers respectively. The Xu and Fang correlations consist of two different equations, one for the evaporating and one for condensing flows. Since there is no model for adiabatic flow, Kim & Mudawar is used, as

it is the newest of the previous four. As explained in chapter 2, Fang, Xu and Zhou developed two new equations for calculating the single-phase friction factor [10], specifically for two-phase flows. One for rough and one for smooth tubes. Both of these will be tested in combination with the Xu & Fang two-phase equations.

Table 8.1: Used combinations friction correlations. The Haaland equation is used for the liquid-only flow in all cases.

Name in plots	Two-phase evaporating		Two-phase adiabatic		Two-phase condensing	
	2- ϕ multi	1- ϕ ff	2- ϕ multi	1- ϕ ff	2- ϕ multi	1- ϕ ff
Lockhart & Martinelli (L&M)	L&M	Blasius	L&M	Blasius	L&M	Blasius
Friedel (Fri)	Friedel	Blasius	Friedel	Blasius	Friedel	Blasius
Muller-Steinhagen & Heck (MSH)	MSH	Blasius	MSH	Blasius	MSH	Blasius
Kim & Mudawar (K&M)	K&M	Bla + In	K&M	Bla + In	K&M	Bla + In
Xu & Fang smooth (XFs)	X&F	FXZ (smooth)	K&M	Bla + In	X&F	FXZ (smooth)
Xu & Fang rough (XFr)	X&F	FXZ (rough)	K&M	Bla + In	X&F	FXZ (rough)

As explained in chapter 6, all correlations will initially be simulated with a change in evaporator power input from 300W to 1500W and back to 300W. Both the simulation and the measurement were run for 20 to 30 minutes between stepping the power up and back down, to let the system stabilize to a steady state. For clarity, the plots and comparisons in this chapter will only focus on the power change and its direct responses.

8.2. Pressure drop correlation

In chapter 7, the heat transfer and void fraction correlations were already discussed. In both cases, a single correlation was left for further testing. Thus the first step in the validation process is to find the best frictional pressure drop correlation.

8.2.1. Total pressure drop

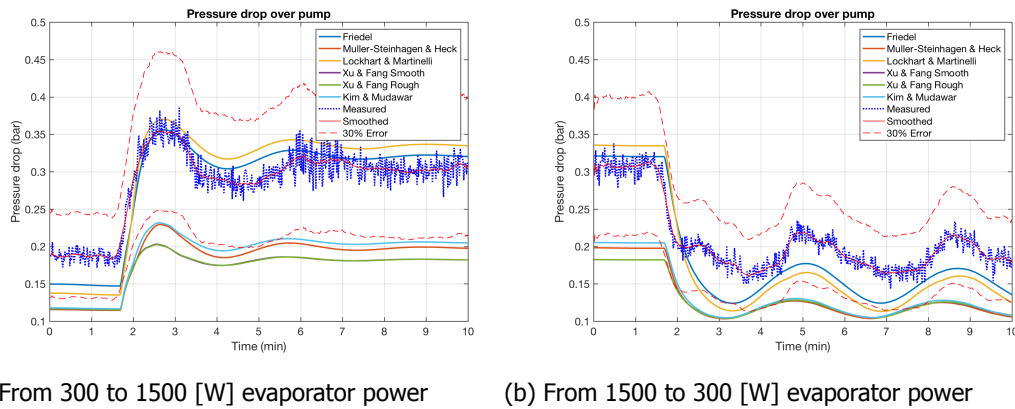
The most direct comparison that can be made for validation of the frictional pressure drop correlation is the total pressure drop. The difference in static pressure just before the pump inlet and directly after the pump outlet is measured directly using a differential pressure sensor. This difference amounts to the total pressure drop over the loop.

Since the measurement data contains a lot of noise, a smoothing function is used in the plots, allowing for clearer (visual) comparison of the results and cleaner 30% offset lines. The smoothing function uses a moving average filter with a span of 21 points (meaning that the filter takes the average of the 10 previous and 10 following data points). Each plot shows a snapshot of 10 minutes, containing 600 data points. The span of 21 points of the moving average filter proved to provide the best trade-off between smoothing out minor fluctuations and maintaining the overall trend. Figures 8.1a and 8.1b show the results of the simulations, the actual and smoothed measurement data and the 30% error margins (based on the filtered data).

Table 8.2 gives the MAPE values of each of the simulations. No smoothing is applied for these results. Of all correlations, only the Friedel and Lockhart & Martinelli equations provide results within the 30% error margin. All other correlations seem to significantly underpredict the total pressure drop. Of these two, Friedel achieves the highest accuracy with 9.05% and 16.92 MAPE respectively for the power increase and decrease.

Table 8.2: Mean Average Prediction Errors of total pressure drop using different correlations

	Fri (%)	MSH (%)	L&M (%)	XFs (%)	XFr (%)	K&M (%)
300-1500 W	9.05	35.84	13.05	39.87	39.87	33.79
1500-300 W	16.92	37.21	22.37	37.86	37.88	35.74



(a) From 300 to 1500 [W] evaporator power

(b) From 1500 to 300 [W] evaporator power

Figure 8.1: Pressure drop comparison between the 6 different correlations and experimental data

8.2.2. Local pressures

Apart from the pressure difference sensor, the demonstrator loop contains three absolute pressure sensors, as explained in chapter 3. One is located just before and one just after the evaporators, and one on top of the accumulator. Due to the simplified geometry, the location of these sensors in the simulation can only be approximated. Moreover, these sensors are less accurate than the pressure difference sensor used for the total pressure drop measurements. Therefore the total pressure drop is considered most important for determining the accuracy of the pressure drop correlations. However, the absolute pressure sensors can give some additional insight in the overall performance of the numerical model.

As explained in chapter 4.2, the accumulator is simulated as a single node, meaning that a uniform pressure is assumed. In reality, the pressure sensor is located at the top of accumulator 2. To have a fair comparison, the gravitational pressure difference has to be taken into account. The pressure difference is calculated using the distance between the accumulator inlet and the top of the vessel, the liquid height and the density of both the liquid and vapour phase. In this case, the difference amounts to between 0.031 and 0.036 bar, depending on the liquid level, or between 0.3 and 0.4% MAPE. This is certainly significant compared to a total pressure drop of between 0.15 and 0.35 as measured in the previous section.

The results of this comparison can be found in figures 8.2, 8.3, and 8.4 and table 8.3. The percentage errors are much smaller in this case, since the differences are now compared to the absolute pressure instead of the pressure drop.

Figure 8.3 shows that all correlations perform more or less the same in predicting the evaporator outlet pressure. This is not surprising, as this is the pressure sensor used as the main control input for the temperature and accumulator controls. Furthermore, the numerical model performs quite well in simulating the period and amplitudes of the oscillations in the dynamic response. However, it is not perfect.

Figures 8.2 and 8.4 do show a difference between the correlations. Like in the pressure drop comparison in the previous section, two correlations stand out: Friedel and Lockhart & Martinelli. However, in contrast to their good performance in predicting the overall pressure drop, they seem to give the least accurate predictions for the evaporator inlet pressures, especially at high power settings. On the other hand, the accumulator pressures are again best predicted by Friedel and Lockhart & Martinelli.

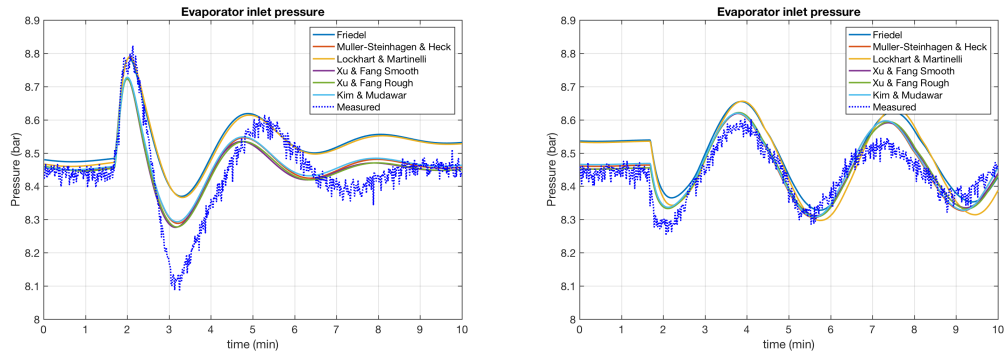
8.2.3. Pressure drop over evaporators

This leads to a more fundamental discovery: The pressure drop over the evaporator is *overestimated* by all correlations. By plotting the difference between the evaporator inlet and evaporator outlet pressures the pressure drop over this component can be measured. By subtracting the unfiltered data of these two sensors, the noise and error margins are doubled, resulting in the very noisy data in figure 8.5. Still, the experimental data shows that the pressure drop over the evaporator stays practically constant with changing heat inputs.

The Friedel and Lockhart & Martinelli correlations, however, predict that the pressure drop should

Table 8.3: Mean Average Prediction Errors of local static pressures using different correlations

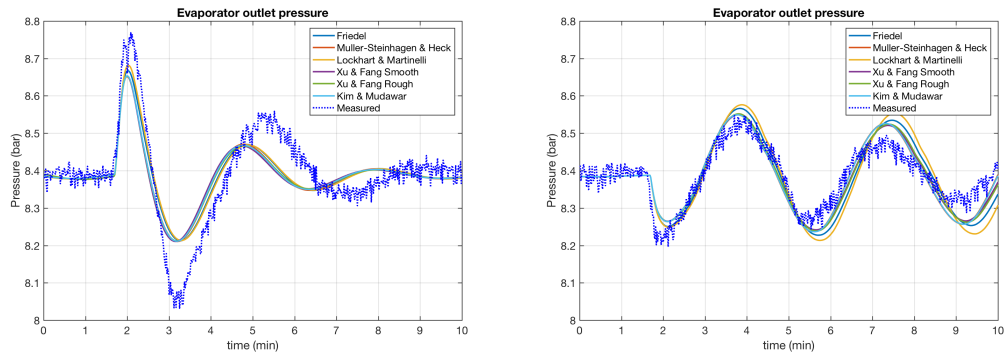
		Fri (%)	MSH (%)	L&M (%)	XF _s (%)	XF _r (%)	K&M (%)
Evaporator Inlet	300-1500 W	1.05	0.62	1.00	0.63	0.60	0.64
	1500-300 W	0.75	0.39	0.78	0.38	0.40	0.41
Evaporator Outlet	300-1500 W	0.58	0.63	0.56	0.65	0.63	0.64
	1500-300 W	0.44	0.36	0.54	0.35	0.37	0.36
Accumulator (corrected)	300-1500 W	0.86	1.23	0.75	1.29	1.28	1.21
	1500-300 W	0.72	0.85	0.74	0.87	0.87	0.84



(a) From 300 to 1500 [W] evaporator power

(b) From 1500 to 300 [W] evaporator power

Figure 8.2: Evaporator inlet pressure comparison between the 6 different correlations and experimental data



(a) From 300 to 1500 [W] evaporator power

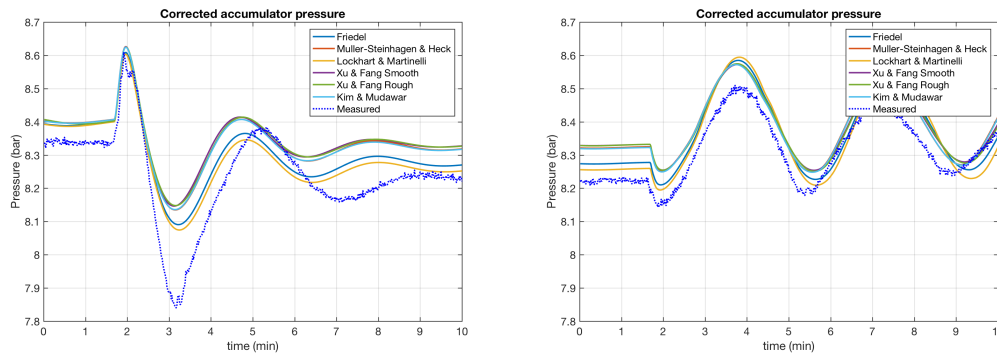
(b) From 1500 to 300 [W] evaporator power

Figure 8.3: Evaporator Outlet pressure comparison between the 6 different correlations and experimental data

rise with increasing heat input. Overestimating the pressure difference by a factor 3 at 1500W. The other correlations seem to do a much better job, but they still seem to slightly overestimate the pressure drop. Moreover the Kim & Mudawar and Muller-Steinhagen & Heck equations also suggest a small change in pressure drop with changing heat input, which is not clearly visible in the experimental data. Only the two Xu & Fang correlations (which perfectly overlap each other) seem to get this detail right.

A restriction (length of tube with a very small diameter) is placed at the start of each evaporator with the express intent to dominate the pressure drop over the evaporators. This is done in an effort to keep the fluid flow balanced over all three evaporators. The experimental measurements seem to indicate that this is indeed working as expected: Any variations due to changing heat inputs are insignificantly small in relation to the dominant constant pressure drop caused by the restriction.

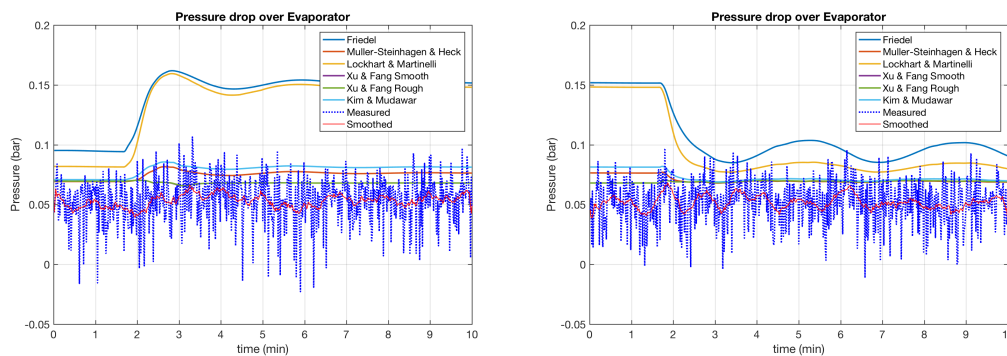
The fact that the simulations do not show the same result suggests that there are some discrepancies between the simulation and reality. The Friedel and Lockhart & Martinelli correlations are developed for adiabatic flows. It is therefore unsurprising that their performance is compromised for the evaporating



(a) From 300 to 1500 [W] evaporator power

(b) From 1500 to 300 [W] evaporator power

Figure 8.4: Corrected accumulator pressure comparison between the 6 different correlations and experimental data



(a) From 300 to 1500 [W] evaporator power

(b) From 1500 to 300 [W] evaporator power

Figure 8.5: Pressure drop over the evaporators, according to the 6 different correlations and experimental data (smoothing uses MATLABs built-in 'rlowess' filter)

flow. The other models are all designed specifically for evaporating fluid flow and indeed show better performance.

The individual pressure drop contributions for each element and each time step have not been logged in the numerical simulations, it is therefore impossible to make a breakdown of how each of these factors contributed to the final error. However, the values of the last time step of each simulation can still be found and compared to give some indication.

The simulated pressure drop due to the restrictions is around 58 mbar for all the correlations, independent of heat load. This is almost equal to the total measured pressure drop over the evaporators in the experiments and thus the leading contributor (as it should be, according to the theory). The minor and momentum pressure differences are consistently 1.0 and 0.9 mbar, respectively. Only in the frictional pressure drop can a large difference be seen between the correlation, ranging from just 3.2 mbar predicted by the XU & Fang correlations to 87 mbar computed by the Friedel correlation at 1500 W heat input.

This proves that the significant differences between the simulations and experiments are caused by the frictional pressure drop correlations. The fact that all simulations overestimate the total pressure drop likely has a multitude of causes. One important note is that the calculated pressure drop over the restrictions might be slightly too high, caused by inaccuracies in the exact length and diameter of the channel and overestimation of the 'minor' pressure losses for sudden reductions and expansions in channel diameter. Another likely option is that an inaccurate model of the evaporator geometry leads to incorrect friction values. As explained in chapter 4, the simplified geometry was determined empirically, based on data from the manufacturer's brochure.

Still, the most important differences lie between the frictional pressure drop correlations. Most notably, the Friedel and Lockhart & Martinelli equations, which severely over-predict the change in pressure. The most likely explanation for this error is that these equations were developed for steady,

adiabatic flow, instead of transient evaporating flows.

Taking into account this new information and looking back at figure 8.1 shows that the pressure drop over the evaporator takes up a significant portion of the whole pressure drop. But, the fraction of the total that is formed by the evaporator pressure drop differs significantly between the correlations. To better compare the influence this has on the validity of the previous results, a new set of plots has been made. Figure 8.6 is formed by subtracting pressure drop over the evaporator from the total for the experimental data and each of the correlations individually. In other words by subtracting the values in figure 8.5 from figure 8.1. The results show that, while Lockhart & Martinelli and Friedel still have the best performance, a large portion of the *perceived* accuracy of these correlations in section 8.2.1 was actually caused by these errors in the frictional pressure drop over the evaporators.

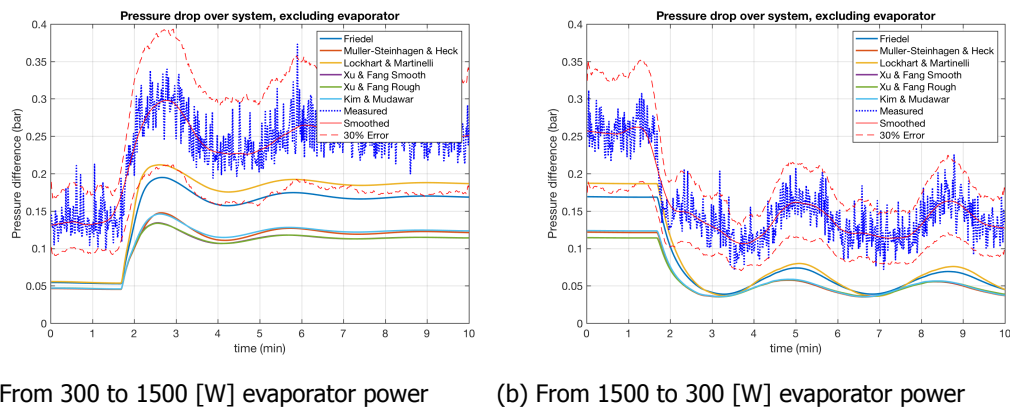


Figure 8.6: Total pressure drop minus the evaporator section, according to the 6 different correlations and experimental data (smoothing uses MATLABs built-in 'rlowess' filter)

This offset is most probably caused by incorrect assumptions about the internal geometry. As explained in section 4.2, the internal layout of the evaporators and some other off-the-shelf components was approximated using a tool developed by J. Terpstra [8]. This tool reverse-engineers a (simplified) layout, based on data and graphs, including the stated pressure drop, from the manufacturer. This was assumed to be sufficient, and as such outside the scope of this project, but that assumption now seems to be proven incorrect.

If this is indeed the source of this error, it means the inaccurate results are simply caused by incorrect inputs. Therefore, it has no direct impact on the validity of the numerical model. However, this error makes it impossible to truly gauge the total model accuracy.

8.3. Accumulator liquid level

The liquid level in the accumulator is an important parameter for a two-phase system. As explained in chapter 2, the accumulator simultaneously works as an expansion vessel and pressure control element in the system. For both functions, the amount of liquid present in the vessel is important for their performance. As an expansion vessel, the ratio of liquid-to-vapour determines the amount of dampening on the transient pressure variations. This effect is accounted for in the numerical model and it is therefore important that the accumulator levels are accurate, in order to get the most accurate transient pressure simulations.

For the heat control elements, the height of the liquid determines how efficient the heater and cooling work. When the level gets too low, the heaters will not be fully submerged and start to overheat. If the liquid level gets too high the cooling elements can become (partially) submerged, causing them to start subcooling the liquid instead of condensing the vapour. For simplicity, these last effects are not simulated in the numerical model. As this model is built specifically to aid the design and development of new two-phase systems, this is of lesser importance. Inversely, accurate approximations of the liquid levels in the accumulator can be used to decide the optimal placement of the heat control systems in the development phase.

This is, however, one of the hardest parts to validate since it is based on multiple assumptions and estimates. First of all, the internal shape of the accumulator is approximated from product drawings,

as explained in chapter 4.2. The fluid level at the start of the simulation is only an estimation as well, as explained in chapter 6.3. Both of these add an error margin to the simulated fluid level. Moreover, as explained earlier, calibration of initial fluid level setting involved a certain amount of tuning, which could add some bias to the simulation results as well.

The accuracy of the experimental liquid level is hindered by two assumptions as well. As explained in chapter 6.3, calibrating the liquid level sensor was quite a difficult task, and since it was executed by hand there is probably a relatively wide margin of error. Finally, the sensor is only installed in one of the two accumulator vessels. The simulation assumes that the liquid height is equal in both accumulators, but this might not be the case in reality, as is briefly discussed in chapter 7.1.

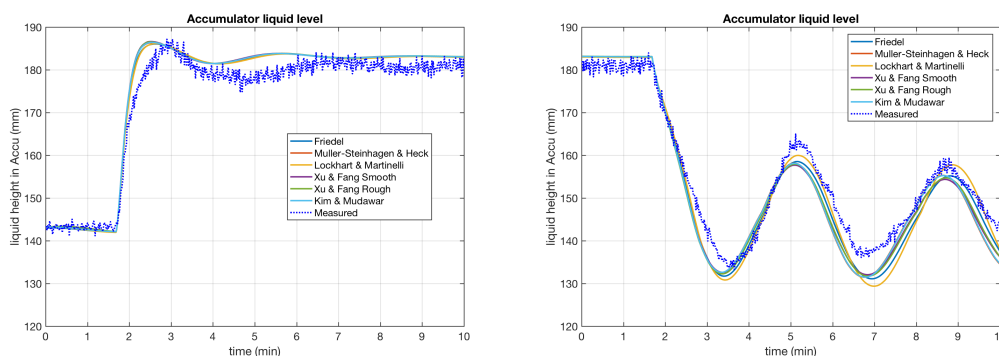
Figure 8.7 shows a comparison between the measured values and the simulation results using the different pressure drop correlations. The graphs show that all simulations perform extremely well in predicting the accumulator level. The steady state level at low heat input matches exactly, due to the calibration mentioned above, and the predicted level at high power input is only slightly higher than the experimental results. Moreover, while the real system seems to have a slightly slower response, the overall shape and size of the transient fluctuations is also identical.

The percentage errors of each simulation run are shown in table 8.4. As with most of the earlier steps, the Friedel and Lockhart & Martinelli correlations give the closest approximation, but only by a small margin. Theoretically, pressure drop should have little impact on the accumulator level, since they are not directly dependant on each other. Only in the transient phases, where changes in the pressure drop influence the local mass flows should any differences be visible between the correlations. This is indeed the case and therefore this implementation is deemed valid.

A more interesting point is the accuracy of the predictions since all of these simulations were done based on the homogeneous flow assumption. It was expected that the void fraction would have a major impact on the liquid level in the accumulator. The vapour volume fraction correlations directly influence the volumetric ratio of liquid and vapour in the whole system. The non-homogeneous correlations should predict smaller void fractions compared to the homogeneous case. In a closed system, less vapour in the 'loop' should mean that there should be more vapour (and thus less liquid) in the accumulator. Therefore, it was expected that the homogeneous model would result in poor liquid level predictions, where the void fraction correlations should perform much better. Instead, the results show the opposite. Very accurate predictions using the homogeneous model and a larger error when using the void fraction model, as shown in the next section.

Table 8.4: Mean Average Percentage Errors of Accumulator liquid level using different correlations

	Fri (%)	MSH (%)	L&M (%)	XF _s (%)	XF _r (%)	K&M (%)
300-1500 W	1.42	1.51	1.41	1.52	1.51	1.50
1500-300 W	2.07	2.35	2.06	2.28	2.28	2.32



(a) From 300 to 1500 [W] evaporator power

(b) From 1500 to 300 [W] evaporator power

Figure 8.7: Accumulator liquid height, according to the 6 different correlations and experimental data

8.4. Temperature

To answer the first research question in chapter 3.2, the accuracy of the calculated temperatures should be tested. However this is more difficult than it sounds. First and foremost, the temperatures in the experimental setup can only be measured using thermocouples stuck to the outside of the equipment, while the temperature calculations in the model mainly focus on the temperature of the fluid inside the tubes. Even though these thermocouples are applied directly to the metal, with a layer of insulation on the outside, there will still be a temperature gradient through the metal. Since these elements were assumed to be adiabatic, as noted in chapter 5.2, these temperature gradients are not calculated and it is therefore difficult to compare the measured temperatures to the results of the numeric model.

Determining the temperature is even more difficult in the evaporator, condenser and other heat-exchanging elements. The complex internal geometries of these elements will also lead to complex thermal gradients throughout the metal enclosures. Since the internal layout of these components is unknown, no attempt is made to model these gradients. Instead, the model only uses the total mass and specific heat capacity of the metal to approximate the thermal capacity of these elements and their influence on the transient responses. The effects of internal conductive heat transfer in these metal parts is ignored.

The location where temperature is the most important is considered to be at the evaporator interface, since this is where the (temperature-sensitive) payload will be installed. However, the model limitations discussed above make it unlikely that an accurate temperature prediction can be made for this point. Moreover, the temperature sensors can not physically be placed in this location, since it is completely covered by the heaters. Taking this into account, an attempt was made to compare the temperatures at the edge of the evaporator, where the outlet tube is connected. The results are shown in figure 8.8.

These results show that the temperature simulations remain within the 30% error margin around the measured values. Another point that can be observed is that there is very little difference between the simulations, and a much larger offset between the simulations and the real-world measurements. This offset can be explained by the fact that the internal condition of the metal is not simulated. Moreover, since these comparisons are performed on the temperatures at the edge of the evaporator instead of at the interface and all the simulation results practically overlap, it is unlikely that any useful information can be learned through further investigation. Therefore, the temperature simulations will not be taken into account for the final correlation selection.

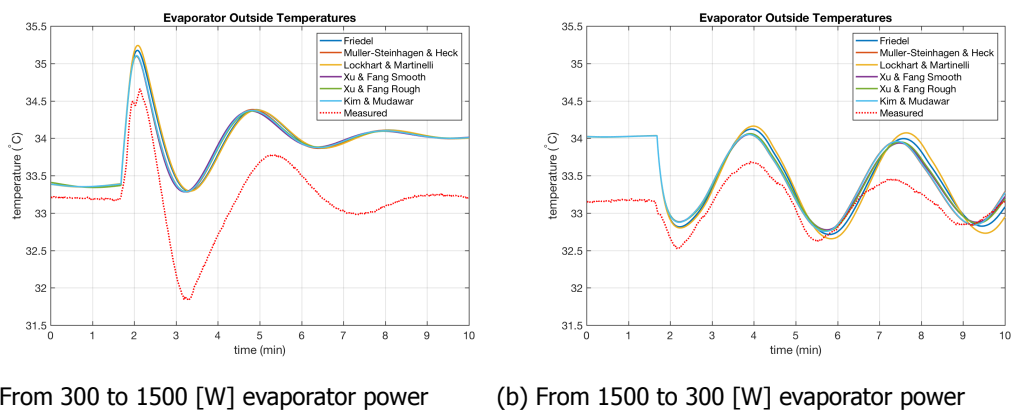


Figure 8.8: Temperature at the edge of the evaporator, comparison between the 6 different correlations and experimental data

8.5. Void fraction

As explained in chapter 7.3, the void fraction was not working initially and was therefore excluded from the first validation steps. An implementation error was eventually found and fixed during the validation phase. However, in the interest of time, it was decided to not completely restart the validation using all correlations, but only test the void fraction with the best combination of HTC and Pressure drop correlations.

All five of the implemented vapour volume fraction correlations were tested, using the Friedel and

Gungor-Winterton correlations for the pressure drop and HTC, respectively. Out of these 5, only the Baroczy correlation was able to run from 300 W to 1500 W and back to 300 W without a negative flow error. Thus only the Baroczy will be used in this validation effort.

8.5.1. Accumulator liquid level

The first check performed was the accumulator level. As mentioned in section 8.3, it is expected that the most obvious difference between the homogeneous and non-homogeneous void fraction models would be seen in the accumulator level. Specifically, it was expected that the void fraction correlations would result in accurate predictions of the liquid level inside the accumulator.

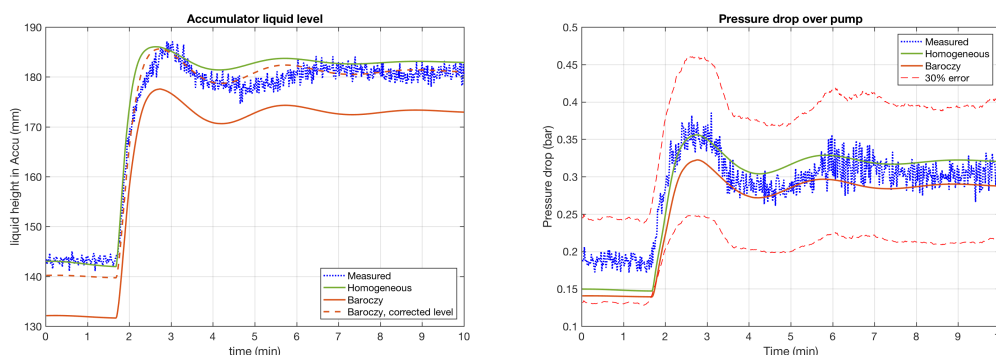
Figure 8.9a shows this comparison between the homogeneous and Baroczy void fraction equations using the Friedel pressure drop correlation, exactly as seen in figure 8.7a. This graph seems to show that, in contrast to what was expected, the Baroczy void fraction correlation performs much poorer than the homogeneous equation.

A probable cause for this under-performance is that the initial liquid level for the simulation was calibrated and essentially tuned for the homogeneous equation. The non-homogeneous void fraction models predict that the vapour phase would travel (much) faster than the liquid phase, increasing with the vapour mass fractions. Therefore, the local vapour volume fractions in the non-homogeneous models will be smaller than those in the homogeneous model, as could already be seen in figure 2.5. This difference increases with increasing heat load. In other words, at maximum heat load and assuming non-homogeneous flow, the overall vapour volume fraction in the loop would be much smaller than it would be with the homogeneous assumptions. Meaning that the total volume change in the loop, and therefore the level change in the accumulator, should be much smaller for non-homogeneous models than it is for the homogeneous model.

Since initial level setting is calibrated (or tuned) by essentially extrapolating the lowest liquid level based on measurements at higher power settings, as explained in chapter 6.3, the predicted initial level for homogeneous flow will be much lower than it would be if tuned for the Baroczy correlation. Thus it makes perfect sense that the liquid level as predicted by the Baroczy equation is significantly lower than the measured level. At this point in the validation, however, it was too late to try and re-calibrate the initial setpoint for the non-homogeneous void fraction models.

Instead, an attempt was made to check its performance by artificially 'correcting' for this difference in initial accumulator level. This was done by calculating the average difference between the measured and the calculated values and adding the difference to the latter. This attempt made was purely to visualise how the graphs would line up and to be able to better (visually) compare the transient responses.

Looking back at figure 8.9a, the corrected Baroczy results do not seem to perform significantly better than the homogeneous curve. To compare, the mean average percentage errors of the 'corrected' Baroczy results are shown in table 8.5. For a fair comparison, the homogeneous results have been 'corrected' in the same manner by subtracting the average offset to the measurements from the results.



(a) Accumulator liquid level

(b) Pressure drop

Figure 8.9: Comparison between the experimental results and the simulations using the Baroczy and Homogenous void fraction models

Table 8.5: Mean Average Percentage Errors of Accumulator liquid level showing both the 'corrected' homogeneous and Baroczy void fraction correlations.

	Homogeneous (%)	Baroczy (%)
300-1500 W	1.08	1.13
1500-300 W	1.61	2.35

From this comparison, there seems to be very little difference between the homogeneous and non-homogeneous equations in terms of performance. While the numbers suggest that the homogeneous model has a slightly better overall accuracy, the graph shows that the Baroczy equation seems to predict the transient response slightly better.

8.5.2. Pressure drop

Next, the pressure drop predictions were compared, as shown in figure 8.9b. In this graph, an important observation was made. While both the homogeneous and Baroczy correlations were tested using the same pressure drop correlations, the results for the steady-state pressure drop differ. Since the pressure drop correlations are not dependant on the void fraction, this should not be the case. In other words, there is still an error in the numerical implementation of the void fraction.

Looking back at the original implementation, the most likely cause of this is the way in which the void fraction results are implemented in the rest of the model. As explained in chapter 5.3, the results of the void fraction calculations are used to calculate the bulk fluid densities for the whole system. These values are subsequently used to calculate fluid velocity and the mass flux. However, it was not fully considered that the density and velocity values are also directly used in other correlations that are supposed to work only with homogeneous flow models. Using these non-homogeneous flow parameters therefore causes erroneous results in the pressure drop and HTC correlations. This means that the current void fraction implementation is invalid and cannot be used. Only simulations using the homogeneous flow correlation can therefore be used for validation.

8.6. Final Correlation selection

After analysing the results of all the tests performed in this chapter, a final selection can be made of the best combination of correlations to be used in the final model. First is the Gungor-Winterton HTC correlation [2]. Since both of the other HTC equations could not be used this was the only choice left.

As explained in section 8.4, the temperature results could not be directly compared and it is therefore hard to directly quantify the accuracy of the HTC correlations. Indirectly, the HTC has a dominant effect on the lag of the transient responses. Since this property of the responses fits the measurements well, the HTC equation is considered valid. However, these results cannot be compared to other HTC correlations, so the relative accuracy and influence of the HTC correlations can not be derived.

The void fraction models are another story. Because of the implementation errors discussed in section 8.5 only the homogeneous flow model could be used. But, in contrast to earlier expectations, this seems to have limited impact on the accuracy of the final simulations. Therefore, it is currently the only valid option.

Finally, the best frictional pressure drop can be selected based on the outcome of the previous two paragraphs. Paired with the homogeneous flow and Gungor-Winterton models, the Friedel correlation clearly performs best[1]. Even though some issues were found with simulating the pressure drop over the evaporator, it still shows the most consistent performance and most accurate overall results.

In order to fully validate the model using the selected correlations, more extensive testing is required. The first step is to perform simulations for all the baseline heat input power levels, selected in chapter 6.3. Tests were performed at each of these power levels as well as for all the step power changes between them. The plots comparing each of these simulation runs with the corresponding experiimental datasets can be found in appendix E. The mean average percentage errors of both the pressure drop and accumulator liquid level results for each of these tests is presented in table 8.6. Only the largest step power decrease led to a negative flow error, while all the others ran without issue. Combining all these results leads to an average MAPE of 7.71% for the pressure drop and 1.34% for the accumulator level.

Table 8.6: Mean Average Percentage Errors of the final selected correlation combination of Friedel and Gungor-Winterton, using the homogeneous flow assumption.

	Pressure drop (%)	Accumulator level (%)
300-1500 W	9.05	1.42
1500-300 W	16.92	2.07
300-2100 W	8.20	1.62
2100-300 W	Negative flow	
300-900 W	7.93	1.54
900-300 W	15.89	2.56
900-1500 W	5.56	1.12
1500-900 W	4.50	1.19
900-2100 W	3.53	1.09
2100-900 W	3.90	1.26
1500-2100 W	3.88	0.96
2100-1500 W	5.43	1.23

This shows that the numerical simulation and the selected correlations work well for the chosen input settings and a wide range of power levels. However, the power level is only one of the many input settings. In order to truly validate the model for a wider range of conditions, many more tests should be performed. Ideally the validity range or envelope should be determined (empirically) by repeating the test above for iterations in flow speeds, set point temperatures and eventually different fluid levels, working fluids and geometries. Additionally, the accuracy of the model could further be determined by performing sensitivity analyses. These are a series of tests performed by applying small changes to a single input parameter and analysing how these affect the results in order to determine the effect of uncertainties on the model accuracy and further define the validity range.

In appendix D, the results of a short sensitivity analysis around the pipe roughness and pipe diameter values is presented. These two parameters were considered most relevant as these are often based on the specifications given by a manufacturer and (especially for this setup) the accuracy of these values is not always exactly known. This short study showed that neither of these parameters is the sole cause of any of the offsets found between the measurements and simulations and are only small contributors to the total simulation errors. Sadly, performing a full sensitivity analysis on all parameters in the model as well as determine the complete validity range would require several months of additional work, which would take it beyond the scope of this thesis project. Therefore, the two tests are put in the appendix and the real sensitivity analysis is left for future research.

9

Conclusions

Now that the results are in, conclusions can be drawn. These conclusions will be linked to the research questions posed in chapter 3.2, repeated below for reference. The answers for these questions will be given systematically in the following paragraphs.

Research Questions

1. Can the existing numerical model be adjusted to predict the dynamic responses to changing heat input, with regards to temperature, pressure and accumulator liquid level with mean absolute errors less than 30 %?
2. Which of the proposed correlations provides the most accurate predictions of the performance of the demonstrator setup filled with R134a?
3. What are the leading causes of inaccuracies in the numerical results? (Inaccurate correlations, uncertainties in internal geometries, assumptions)?
4. What is the achievable accuracy and expected validity range of the final numerical model?
5. Can the resulting numerical model be used to predict the dynamic performance of different fluids, without any further adjustments other than the different input parameters?

Overall performance At first glance, it seems like the first research question can definitively be answered with a *yes*. However, there are some important limitations and nuances that need to be taken into account. Several unsolved errors remain in the model, limiting the functionality and allowing the opportunity of 'false positives' in the results, which will be discussed further in the following paragraphs. Another matter of note is that, while a short test of the temperature simulation showed that the results were within the 30% accuracy range for the selected location, the overall results were not useful enough to warrant further testing, investigation and validation, as explained in chapter 8.4.

Best combination of correlations The results of the validation show that the combination of Friedel (frictional pressure drop), Gungor-Winterton (HTC) and homogeneous flow (void fraction) correlations result in the best accuracy for the chosen demonstrator setup, which answers the second question. Using these equations, the prediction error for the total pressure drop is only 7.7% on average and the accuracy of the accumulator liquid level predictions is even better at 1.3% on average, according to the tests done in section 8.6. Here as well, it is important to take into account the limitations of the model discussed in the next paragraph.

Limitations and inaccuracies in the model It is slightly harder to answer questions 3, 4 and 5. There are several limitations and inaccuracies that can limit the applicability of the numerical model. These will be discussed in this paragraph in order to answer question 3. With this in mind, the last two questions can be answered in the following paragraph.

First off is the negative flow condition. As long as this is not solved, there might be configurations for which the simulation will not be able to resolve a solution (e.g. when switching from maximum to minimum power loads like the). As stated in chapter 7, it is not certain if these results are caused by an error in the code or actual occurrences in the flow. Although unlikely, it has not been proven conclusively that these local reversals in flow direction do not happen in the actual setup. On the other hand, a potential simulation error could be caused by the error margin in the correlations, artefacts of discontinuous transitions between the equations or plain errors in the code.

Second is the void fraction implementation. As concluded in chapter 8, it still contains an error that invalidates the results of all correlations except for the homogeneous one. This means that the initial hypothesis that non-homogeneous void fraction correlations will lead to more accurate simulation of the transient responses than when homogeneous flow is used, cannot be proven or disproven. What can be concluded however, is that the homogeneous flow condition does result in more accurate results than initially expected.

Similarly, of the three HTC equations to be implemented, only Gungor-Winterton could be used. Luckily, neither of these limitations seem to have had a major negative impact on the overall accuracy of the results. Thus, while solving the problems with flow reversal could significantly increase the applicability of the model and improving the void fraction implementation might lead to slightly better accuracies, these are currently not the major causes of inaccuracies in the model.

Finally, as shown in section 8.2.3, the pressure drop in the evaporators has a very high margin of error. In some cases the predicted pressure drop is almost three times as high as the measured value. Since the pressure drop in all other components is consistently under-predicted for this setup, this error actually causes the total offset to decrease, making it seem like the Friedel and Lockhart & Martinelli correlations perform much better than they actually do. While this works beneficially in this case, it is very misleading and can easily lead to large errors and false conclusions. This is therefore the most important of the inaccuracies and should be addressed first in future updates.

As noted in the previous chapter, this is probably caused by the way the evaporator geometry was approximated. It is therefore likely an external factor and therefore does not invalidate the numerical model per se. However, it does undermine the whole validation process and makes it harder to draw definitive conclusions.

Validity range Question 4 cannot be answered completely, since the validity range of this model is still unknown. Additional (extensive) tests are required to fully determine this margin. Similarly, it is hard to give a definitive answer to the last question. But the results of this thesis show that it is at least able to predict the transient behaviour of a two-phase system with R134a as working fluid at saturation temperatures around 33 °C. Combining this with the fact that the original version of this model was validated for CO₂ based simulations around 22 °C [19] and a different geometry, the model is expected to be valid for a range of similar working fluids and geometries at temperatures around room temperature at the very least.

Final remarks Overall, it can be concluded that the numerical model is valid and able to predict the transient behaviour of a two-phase system with a very high level of accuracy. It can therefore be extremely useful for initial design and prototyping phases. As such it can save time and effort by 'computationally' testing different potential designs and working fluids. But, in its current state it is unadvisable to base a final design purely on the results of this simulation. For that to happen, several of the unexpected errors and limitations need to be addressed first and more tests need to be performed with different setups, conditions and fluids to fully validate the model performance.

Finally, in what might seem a very obvious, but still insightful, conclusion from this thesis is that added complexity increases the risk of errors. In writing computer code, but also in developing empirical correlations and writing papers about these equations, as evidenced by the many erroneous notations of these equations found in the referenced papers, as discovered and discussed during the literature study [4]. Equations containing more parameters might seem to be more true-to-nature and result in more accurate predictions, but this usually only works under well controlled (steady-state) conditions in the lab. Especially when these correlations are used in a finite-difference model that will always have a certain margin of error due to discretisation, more parameters means that their individual error margins will accumulate into a larger total error.

10

Recommendations

Based on the conclusions, there are several opportunities for future research to broaden the applicability of the model and increase the accuracy. In this chapter, a selection of the most important recommendations will be given.

First and foremost, the frictional pressure drop in the evaporators needs to be addressed. The large error margins in this section of the model have significant impact on the total performance and can lead to misleading results. As discussed in the previous chapters, the error is probably caused by incorrect assumptions and approximations regarding the internal geometry of the evaporator. This has to be investigated and new method for approximating the internal geometry of 'complex' elements needs to be developed (probably). A good starting point for this could be to make the approximation part of the simulation, by 'reverse engineering' the geometry based on the manufacturer data and the conditions and correlations currently selected for each model run could make the results more accurate.

Just as important is the 'negative flow', which should be further investigated. If a definitive cause can be identified, it can hopefully be fixed, resulting in a more reliable model. One of the potential causes identified in chapter 7 is the occurrence of discontinuities in and between several of the correlations. When the flow transitions from laminar to turbulent or from single-phase to two-phase, it usually happens in a gradual manner, but in many cases, the simulation model will make a 'hard' switch from one equation to the other. This is especially evident when using the Kim & Mudawar equation for dryout incipience [16], which would cause a very large discontinuity when stepping from two-phase evaporating heat transfer to dried-out single-phase gas convection. Finding a good way to implement smoother transitions between the different correlations is therefore of prime importance.

Once these two major issues are addressed, a more intensive testing regime is required to truly define the validity range and error margins of the model. Preferably, this has to be done with a range of setpoint temperatures, working fluids, and system layouts. It would also be interesting to test the performance of the model for predicting the flow through the each evaporator, when the input power differs between the parallel evaporator panels. This is a case initially investigated by Terpstra [8] and one of the reasons for the specific design of the NLR demonstrator set up.

There are of course also some less urgent improvements that could be made to the model. Most obvious of these is fixing the void fraction implementation. While the results show that this model is able to reach high accuracy for R134a, it might not do so for all other fluids and it would be very interesting to define the exact influence and significance of the homogeneous flow assumption on the total model accuracy.

Another improvement that could be made is in the geometry inputs for the model. This would significantly increase the user-friendliness of the numerical model and, if executed well, reduce the chance of errors. The first step would be to develop a better approximation method to automatically define and implement the geometry of complex or 'black-box' commercial off-the-shelf components such as the evaporator. Next would be a graphical user interface, or at least a visual aid such as a render of the currently defined geometry to simplify the implementation process and make it easier to check errors. Finally, some code could be added to automatically 'simplify' the implemented geometry for faster calculations.

Similarly, the method in which the initial accumulator fill level is defined could be improved. As explained in chapter 6 this is defined at the heat sink temperature, a situation that in reality is never reached and can therefore not be measured. Thus, it now requires a process of iterative adjustment and 'tuning'. This makes it less accurate and harder to set up.

Finally, changes could be made to the code, to open up the potential for parallel-computing on computers with multi-core CPU's. This could potentially significantly reduce the computation time, thus making the model more useful. MATLAB provides this functionality and an attempt was made early on in the project to implement this. However, the parallel-computing functions do not work in combination with the 'struct' structure arrays that are currently used to store all variables and results in the numerical model. Thus, in order to implement this, a large portion of the code will have to be rewritten.

A

Hardware used in demonstrator

A.1. Evaporator

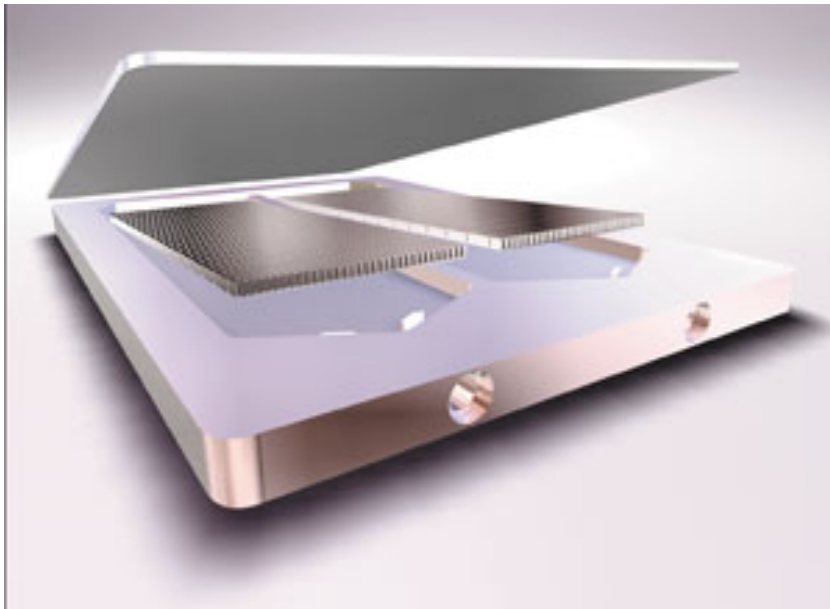


Figure A.1: Digital representation of the internal geometry of the Lytron CP 30 evaporator [34]

A.2. SWEP heat exchangers



SSP G7
(v 7.0.3.33)

CONDENSER - Rating Heat Exchanger : B8Tx14

Port	NND (mm)	Connection
F1	18	ISO-G 3/4" & SOLDER 16 [ArtNo:32835, H2O, SS]
F3	18	ISO-G 3/4" & SOLDER 16 [ArtNo:32835, H2O, SS]
F4	18	ISO-G 3/4" & SOLDER 16 [ArtNo:32835, H2O, SS]
F2	18	ISO-G 3/4" & SOLDER 16 [ArtNo:32835, H2O, SS]

Fluid Side 1 : R134a
Fluid Side 2 : Water

Flow Type : Counter-Current

DUTY REQUIREMENTS		Side 1	Side 2
Heat load	kW	2.000	
Inlet temperature	°C	40.00	20.00
Condensation temperature (dew)	°C	40.00	
Subcooling	K	10.00	
Outlet temperature	°C	30.00	30.00
Flow rate	kg/s	0.02078	0.04785
Fluid condensed	kg/s	0.01039	
Max. pressure drop	kPa	50.0	50.0
PLATE HEAT EXCHANGER		Side 1	Side 2
Total heat transfer area	m ²	0.276	
Heat flux	kW/m ²	7.25	
Mean temperature difference	K	13.97	
O.H.T.C. (available/required)	W/m ² ,°C	885/519	
Pressure drop -total*	kPa	0.247	0.734
- in ports	kPa	-0.0201	0.0188
- inlet connections	kPa	3.20e-3	1.55e-3
- outlet connections	kPa	219e-6	1.39e-3
Operating pressure - outlet	kPa	1020	
Number of channels		6	7
Number of plates		14	
Oversurfacing	%	71	
Fouling factor	m ² ,°C/kW	0.799	
Port diameter	mm	17.5	17.5
Recommended inlet connection diameter	mm	From 3.41 to 7.62	
Recommended outlet connection diameter	mm	From 1.52 to 4.80	
Reynolds number			210
Inlet port velocity	m/s	0.947	0.200

Figure A.2: Datasheet for the Condenser (SWEP heat exchanger with water in the secondary loop)



SSP G7
(v 7.0.3.33)

CONDENSER - Rating
Heat Exchanger : B8Tx14

Port	NND (mm)	Connection
F1	18	ISO-G 3/4" & SOLDER 16 [ArtNo:32835, H2O, SS]
F3	18	ISO-G 3/4" & SOLDER 16 [ArtNo:32835, H2O, SS]
F4	18	ISO-G 3/4" & SOLDER 16 [ArtNo:32835, H2O, SS]
F2	18	ISO-G 3/4" & SOLDER 16 [ArtNo:32835, H2O, SS]

Fluid Side 1 : R134a
Fluid Side 2 : R134a (Liquid)

Flow Type : Counter-Current

DUTY REQUIREMENTS		Side 1	Side 2
Heat load	kW	0.6766	
Inlet temperature	°C	40.00	16.68
Condensation temperature (dew)	°C	40.00	
Subcooling	K	0.00	
Outlet temperature	°C	39.97	39.00
Flow rate	kg/s	0.02078	0.02078
Fluid condensed	kg/s	4.156e-3	
Max. pressure drop	kPa	50.0	50.0
PLATE HEAT EXCHANGER		Side 1	Side 2
Total heat transfer area	m ²	0.276	
Heat flux	kW/m ²	2.45	
Mean temperature difference	K	6.84	
O.H.T.C. (available/required)	W/m ² , °C	504/358	
Pressure drop -total*	kPa	0.930	0.0983
- in ports	kPa	7.32e-3	2.96e-3
- inlet connections	kPa	3.20e-3	236e-6
- outlet connections	kPa	1.81e-3	226e-6
Operating pressure - outlet	kPa	1010	
Number of channels		6	7
Number of plates		14	
Oversurfacing	%	41	
Fouling factor	m ² , °C/kW	0.808	
Port diameter	mm	17.5	17.5
Recommended inlet connection diameter	mm	From 3.41 to 7.62	
Recommended outlet connection diameter	mm	From 4.28 to 13.5	
Reynolds number			412
Inlet port velocity	m/s	0.948	0.0723

SWEP International AB
Address :Box 105, SE-261 22 Landskrona, Sweden www.swep.net

Date
2014-12-08

Page
1(3)

Figure A.3: Datasheet for the Heat Exchanger

A.3. Accumulators

Sample Cylinders

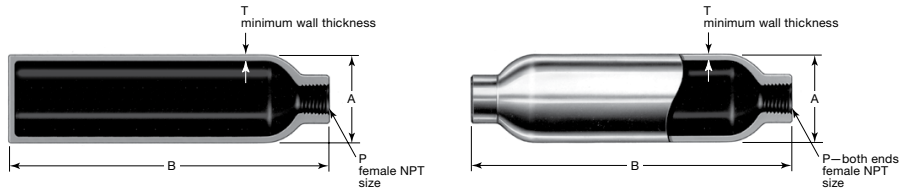
Ordering Information, Technical Data, and Dimensions

Select an ordering number.

Dimensions are for reference only and are subject to change.

Single-Ended Cylinders

Double-Ended Cylinders



Material Grade/ Cylinder Specification	Pressure Rating psig (bar)	Internal Volume cm ³ ± 5 %	P in.	Ordering Number	Dimensions, in. (mm)			Weight lb (kg)	
					A	B	T		
Single-Ended									
304L SS/ DOT-4B 500	500 (34.4)	150	1/4	304L-05SF4-150	2.00 (50.8)	4.88 (124)	0.093 (2.4)	1.1 (0.50)	
		300		304L-05SF4-300		8.62 (219)		1.8 (0.82)	
		500		304L-05SF4-500		13.6 (345)		2.7 (1.2)	
Double-Ended									
304L SS/ DOT-3E 1800 TC-3EM 124	1800 (124)	40	1/4	304L-HDF2-40	1.25 (31.8)	3.88 (98.6)	0.093 (2.4)	0.31 (0.14)	
		50		304L-HDF4-50	1.50 (38.1)	3.75 (95.2)		0.38 (0.17)	
		75		304L-HDF4-75		4.94 (125)		0.62 (0.28)	
		150		304L-HDF4-150	2.00 (50.8)	5.25 (133)		0.94 (0.43)	
		300		304L-HDF4-300		8.94 (227)		1.6 (0.73)	
		400		304L-HDF4-400		11.4 (290)		2.1 (0.95)	
500	304L-HDF4-500	13.8 (351)	2.6 (1.2)						
304L SS/ DOT-3A 1800 TC-3ASM 124	1800 (124)	1000	1/4	304L-HDF4-1000	3.50 (88.9)	10.9 (277)	0.180 (4.6)	6.5 (2.9)	
			1/2	304L-HDF8-1000					
		2250	1/4	304L-HDF4-2250	4.00 (102)	17.2 (437)	0.206 (5.2)	14 (6.4)	
			1/2	304L-HDF8-2250					
		3785 (1 gal)	1/4	304L-HDF4-1GAL		26.7 (678)		21 (9.5)	
316L SS/ DOT-3E 1800 TC-3EM 124	1800 (124)	150	1/4	316L-HDF4-150	2.00 (50.8)	5.25 (133)	0.093 (2.4)	0.94 (0.43)	
		300		316L-HDF4-300		8.94 (227)		1.6 (0.73)	
		500		316L-HDF4-500		13.8 (351)		2.6 (1.2)	
316L SS/ DOT-3A 5000 TC-3ASM 344	5000 (344)	150	1/4	316L-50DF4-150	1.90 (48.2)	8.00 (203)	0.240 (6.1)	3.0 (1.4)	
		300		316L-50DF4-300		14.5 (368)		5.6 (2.5)	
		500		316L-50DF4-500		23.5 (597)		9.1 (4.1)	
Alloy 400/ DOT- SP7458 1800	1800 (124)	150	1/4	M-HDF4-150	2.00 (50.8)	5.25 (133)	0.093 (2.4)	0.94 (0.43)	
		300		M-HDF4-300		8.94 (227)		1.8 (0.82)	
		500		M-HDF4-500		13.8 (351)		2.9 (1.3)	

SAMPLE
CYLINDERS



Figure A.4: Datasheet depicting dimensions of the accumulator vessels [33]

B

Implemented correlations

B.1. Pressure drop

Single-phase friction factor correlations:

Laminar flows: $Re < 2400$

$$f = \frac{64}{Re} \quad (\text{B.1})$$

Turbulent flows: $Re > 4000$

$$\text{Blasius} \quad f = \frac{0.3164}{Re^{0.25}} \quad (\text{B.2})$$

$$\text{Haaland} \quad f = \left[-1.8 \log_{10} \left(\left(\frac{\epsilon/d}{3.7} \right)^{1.11} + \frac{6.9}{Re} \right) \right]^{-2} \quad (\text{B.3})$$

$$\text{Fang, Xu, Zhou smooth} \quad f = 0.25 \left[\log \left(\frac{150.39}{Re^{0.98865}} - \frac{152.66}{Re} \right) \right]^{-2} \quad (\text{B.4})$$

$$\text{Fang, Xu, Zhou rough} \quad f = 1.613 \left[\ln \left(0.234 \left(\frac{\epsilon}{d} \right)^{1.1007} - \frac{60.525}{Re^{1.1105}} + \frac{56.291}{Re^{1.0712}} \right) \right]^{-2} \quad (\text{B.5})$$

For even higher Reynolds numbers ($Re \geq 20,000$)

$$\text{Incropera} \quad f = \frac{0.184}{Re^{0.20}} \quad (\text{B.6})$$

Two-phase frictional pressure drop correlations:

Lockhart & Martinelli	$\Delta p_{f,\text{tot}} = \Delta p_{f,l} \phi^2$	Where: $\begin{cases} \phi^2 = 1 + \frac{C}{X} + \frac{1}{X^2} \\ C_{\text{vw}} = 5 & C_{\text{vt}} = 12 \\ C_{\text{tv}} = 10 & C_{\text{tt}} = 20 \end{cases}$	(B.7)
Using Martinelli factor:	$X = \sqrt{\frac{\left(\frac{\Delta p}{\Delta L}\right)_l}{\left(\frac{\Delta p}{\Delta L}\right)_g}}$		(B.8)
Friedel	$\Delta p_{f,\text{tot}} = \Delta p_{l0} \left[A + \frac{3.24B}{Fr_{l0}^{0.045} We_{l0}^{0.035}} \right]$		(B.9)
	Where: $\begin{cases} A = (1-x^2) + x^2 \frac{\rho_l f_{g0}}{\rho_g f_{l0}} \\ B = x^{0.78} (1-x)^{0.224} \left(\frac{\rho_l}{\rho_g}\right)^{0.91} \left(\frac{\mu_g}{\mu_l}\right)^{0.19} \left(1 - \frac{\mu_g}{\mu_l}\right)^{0.7} \end{cases}$		(B.10)
Muller-Steinhagen and Heck	$\Delta p_{f,\text{tot}} = (\Delta p_{l0} + 2(\Delta p_{g0} - \Delta p_{l0})x) (1-x)^{\frac{1}{3}} + \Delta p_{g0} x^3$		(B.11)
Kim & Mudawar	$C_{\text{tt}} = 0.39 Re_{l0}^{0.03} Su_{g0}^{0.10} \left(\frac{\rho_l}{\rho_g}\right)^{0.35}$		(B.12)
	$C_{\text{tv}} = 8.7 \times 10^{-4} Re_{l0}^{0.17} Su_{g0}^{0.50} \left(\frac{\rho_l}{\rho_g}\right)^{0.14}$		(B.13)
	$C_{\text{vt}} = 0.0015 Re_{l0}^{0.59} Su_{g0}^{0.19} \left(\frac{\rho_l}{\rho_g}\right)^{0.36}$		(B.14)
	$C_{\text{vw}} = 3.5 \times 10^{-5} Re_{l0}^{0.44} Su_{g0}^{0.50} \left(\frac{\rho_l}{\rho_g}\right)^{0.48}$		(B.15)
Evap. flows, $Re_l < 2000$	$C = C_{\text{non-boiling}} \left[1 + 530 We_l^{0.52} \left(Bo \frac{P_F}{P_{\text{tot}}}\right)^{1.09} \right]$		(B.16)
$Re_l \geq 2000$	$C = C_{\text{non-boiling}} \left[1 + 60 We_l^{0.32} \left(Bo \frac{P_F}{P_{\text{tot}}}\right)^{0.78} \right]$		(B.17)
Xu & Fang evaporating	$\phi_{l0}^2 = \left(X^{*2} x^3 + (1-x)^{\frac{1}{3}} [1 + 2x(X^{*2} - 1)]\right) \left[1 + 1.54 \sqrt{1-x} Su^{1.47}\right]$		(B.18)
Condensing	$\phi_{l0}^2 = X^{*2} x^3 + [1 + 2x^{1.17} (X^{*2} - 1) + 0.00775 x^{-0.475} Fr_{\text{tot}}^{0.535} We_{\text{tot}}^{0.188}] (1 - x^{2.59})^{0.632}$		(B.19)

B.2. Heat transfer coefficient

$$\text{Gungor \& Winterton} \quad h_{\text{tot}} = h_{l,\text{db}} \left[1 + 3000 \text{Bo}^{0.86} + \left(\frac{x}{1-x} \right)^{0.75} \left(\frac{\rho_l}{\rho_g} \right)^{0.41} \right] \quad (\text{B.20})$$

$$\text{Kim \& Mudawar} \quad h_{\text{tot}} = \sqrt{h_{\text{nb}}^2 + h_{\text{cb}}^2} \quad (\text{B.21})$$

Where:

$$h_{\text{nb}} = \left[2345 \left(\text{Bo} \frac{P_H}{P_F} \right)^{0.70} p_r^{0.38} (1-x)^{-0.51} \right] h_{l,\text{db}} \quad (\text{B.22})$$

$$h_{\text{cb}} = \left[5.2 \left(\text{Bo} \frac{P_H}{P_F} \right)^{0.08} \text{We}_o^{-0.54} + 3.5 \left(\frac{1}{X_{\text{tt}}} \right)^{0.94} \left(\frac{\rho_g}{\rho_l} \right)^{0.25} \right] h_{l,\text{db}} \quad (\text{B.23})$$

$$\text{Fang} \quad \text{Fa} = \frac{(\rho_l - \rho_g)\sigma}{G^2 d} \quad (\text{B.24})$$

$$\text{Nu} = \frac{0.00061(A+B)\text{Re}_l P_l^{0.4} \text{Fa}^{0.11}}{\ln\left(1.023 \frac{\mu_{l,f}}{\mu_{l,w}}\right)} \quad (\text{B.25})$$

Where:

$$A = \begin{cases} 30000 \text{Bo}^{1.13} & \text{Bo} < 0.0026 \\ 36 & \text{Bo} \geq 0.0026 \end{cases} \quad (\text{B.26})$$

$$B = \left(\frac{x}{1-x} \right)^{0.95} \left(\frac{\rho_l}{\rho_g} \right)^{0.4} \quad (\text{B.27})$$

B.3. Void fraction

$$\text{Homogeneous} \quad \varepsilon = \left[1 + \left(\frac{1-x}{x} \right) \left(\frac{\rho_g}{\rho_l} \right) \right]^{-1} \quad (\text{B.28})$$

$$\text{Slip ratio} \quad \varepsilon = \left[1 + \left(\frac{1-x}{x} \right) \left(\frac{\rho_g}{\rho_l} \right) S \right]^{-1} \quad \text{where } S = \frac{u_g}{u_l} \quad (\text{B.29})$$

Slip ratio models:

$$\text{Zivi} \quad \varepsilon = \left[1 + \left(\frac{1-x}{x} \right) \left(\frac{\rho_g}{\rho_l} \right)^{\frac{2}{3}} \right]^{-1} \quad (\text{B.30})$$

$$\text{Baroczy} \quad \varepsilon = \left[1 + \left(\frac{1-x}{x} \right)^{0.74} \left(\frac{\rho_g}{\rho_l} \right)^{0.65} \left(\frac{\mu_l}{\mu_g} \right)^{0.13} \right]^{-1} \quad (\text{B.31})$$

$$\text{Butterworth} \quad \varepsilon = \left[1 + 0.28 \left(\frac{1-x}{x} \right)^{0.64} \left(\frac{\rho_g}{\rho_l} \right)^{0.36} \left(\frac{\mu_l}{\mu_g} \right)^{0.07} \right]^{-1} \quad (\text{B.32})$$

$$\text{Smith} \quad \varepsilon = \left[1 + \frac{\rho_g}{\rho_l} \left(\frac{1-x}{x} \right) \left(0.4 + 0.6 \sqrt{\frac{\frac{\rho_l}{\rho_g} + 0.4 \left(\frac{1-x}{x} \right)}{1 + 0.4 \left(\frac{1-x}{x} \right)}} \right) \right]^{-1} \quad (\text{B.33})$$

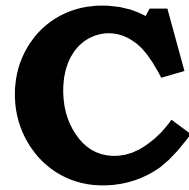
Drift flux models:

Woldesemayat & Ghajar:

$$\varepsilon = u_{s,g} \left[u_{s,g} \left(1 + \left(\frac{u_{s,l}}{u_{s,g}} \right)^{\left(\frac{\rho_g}{\rho_l} \right)^{0.1}} \right) + 2.9 \left[\frac{gd\sigma(1 + \cos \theta)(\rho_l - \rho_g)}{\rho_l^2} \right]^{0.25} (1.22 + 1.22 \sin \theta)^{\frac{p_{atm}}{p}} \right]^{-1} \quad (\text{B.34})$$

Rouhani & Axelsson:

$$\varepsilon = \frac{x}{\rho_g} \left[(1 + 0.12(1 - x)) \left(\frac{x}{\rho_g} + \frac{1 - x}{\rho_l} \right) + \frac{1.18(1 - x)}{G} \left(\frac{g\sigma[\rho_l - \rho_g]}{\rho_l^2} \right)^{0.25} \right]^{-1} \quad (\text{B.35})$$



Numerical code

C.1. CalcTimeLoop structure

1. Calculate length of timestep
2. Determine evaporator power
3. Look up new fluid properties
4. Determine parameters for each component between pump and accumulator
 - 4.1. Calculate heat transfer coefficients for diabatic components
 - 4.2. Find enthalpy at beginning and end of each component, as well as the inlet velocity
 - 4.3. Calculate new enthalpy, density and velocity values
 - 4.4. Calculate the temperature of the tubing (thermal mass)
 - 4.5. Recalculate values in the Heat Exchanger due to reciprocal heat-exchanging effect
5. Calculate pressure drop (reversely, from accumulator to pump outlet)
 - 5.1. Find the pressure at the inlet of component $i+1$
 - 5.2. Add the minor pressure drop between the two components
 - 5.3. Calculate pressure drop due to restrictions
 - 5.4. Calculate the frictional pressure drop throughout component
 - 5.5. Calculate gravitational pressure difference
 - 5.6. calculate momentum pressure change
 - 5.7. Smooth the pressure change
6. Calculate the behaviour inside the accumulators
7. Find fluid properties between accumulator and pump inlet
 - 7.1. Find enthalpy at beginning and end, as well as the inlet velocity
 - 7.2. Calculate new enthalpy, density and velocity values
 - 7.3. Calculate the temperature of the tubing (thermal mass)
 - 7.4. Find the pressure at the inlet of the next component and add minor pressure loss
 - 7.5. Calculate the frictional pressure drop throughout component
8. Calculate new values for the mass flow, vapour mass fraction and fluid temperature
9. Update the 'old' values with the 'new' values
10. Write data to save file (only once in each x timesteps)

C.2. Frictional pressure drop calculations

```
function [dP_fric] = CalcDPfric(x,m,d,L,rho_l,rho_v,mu_l,mu_v,sig,NE,e,...
    constant,Diab,P,Hlv,As)
```

```
#####
%#
%#          Calculate Frictional pressure drop          %#
%#
%#
%#
%#
%#
%#          [dP_fric] =
%#          CalcDPfric(X,m,d,L,rho_l,rho_v,mu_l,mu_v,NE,e,...
%#          constant,Diab,P,Hlv)
%#
%#-----#%
%#   Inputs:          Description:          Unit:          %#
%#   x                Vapour mass fraction (Quality)    [kg/kg]          %#
%#   m                Mass flow                        [kg/s]           %#
%#   d                Local tube diameter              [m]              %#
%#   L                Total length of component        [m]              %#
%#   rho_l            Density liquid phase             [kg/m3]          %#
%#   rho_v            Density gas phase                [kg/m3]          %#
%#   mu_l             Viscosity liquid phase           [kg/m/s]         %#
%#   mu_v             Viscosity gas phase              [kg/m/s]         %#
%#   sig              Surface tension                 [N/m]            %#
%#   NE              Number of elements in component  [-]              %#
%#   e                Surface roughness                [m]              %#
%#   f_cor            Friction factor correlation ind.  [-]              %#
%#                   1 = Haaland                      %#
%#                   2 = Blasius                       %#
%#                   3 = Fang (smooth)                 %#
%#                   4 = Fang (rough)                  %#
%#                   5 = Incropera (High Re)           %#
%#   dP_cor           Two-phase frictional PD corr. ind. [-]          %#
%#                   1 = Muller-Steinhagen & Heck      %#
%#                   2 = Friedel                       %#
%#                   3 = Kim & Mudawar                 %#
%#                   4 = Lockhart & Martinelli         %#
%#                   5 = Xu % Fang                     %#
%#   Diab             Diabatic component indicator     [-]              %#
%#                   0 = Adiabatic component           %#
%#                   1 = Evaporator                    %#
%#                   2 = Heat Exchanger                %#
%#                   3 = Condenser                     %#
%#                   4 = Single-phase component        %#
%#-----#%
%#   Output:
%#   dP_fric          Frictional pressure loss         [Pa]             %#
%#
%#
%#
%#-----#%
```

```
Xtreshhold=1e-3; % Treshhold for determining if coolant is considered fully liquid , or two-phase
```

```
% set initial parameters
x = min(x,1);
ind_tf=find(x>=Xtreshhold); % Determine if fluid is two-phase
ind_sf=find(x<Xtreshhold);

Ac=pi*d^2/4; %crosssectional area

if isempty(ind_sf)
    u_lo=m./(rho_l*Ac); % 'liquid-only' velocity
    Re_lo = m*d/(Ac*mu_l);
    f_lo_laminar=64./Re_lo;
    switch constant.f_cor_sf % Single-phase friction factor
        case 1
            f_lo_turbulent = Haaland(e, d, Re_lo);
        case 2
            f_lo_turbulent = Blasius(Re_lo);
```

```

    case 3
        f_lo_turbulent = Fang(Re_lo);
    case 4
        f_lo_turbulent = Fang2(e, d, Re_lo);
    case 5
        f_lo_turbulent = Blasius(Re_lo);
        ind_Re_lo = find(Re_lo>=20000);
        f_lo_turbulent(ind_Re_lo) = Incro(e, d, Re_lo(ind_Re_lo));
end
smooth_lo = 1./(1+exp(-(Re_lo - 2400)/450));
f_lo = (1-smooth_lo).*f_lo_laminar + smooth_lo.*f_lo_turbulent;
dPdx_lo_sf = f_lo*rho_l.*u_lo.^2/d/2;
else
    dPdx_lo_sf = m*0;
end

if Diab == 4 || isempty(ind_tf) % In case of liquid-only flow
    dPdx_fric = dPdx_lo_sf;
else
    if Diab == 0 % Adiabatic
        f_cor = constant.f_cor_adia;
        dP_cor = constant.dP_cor_adia;
    elseif Diab == 1 % Evaporator
        f_cor = constant.f_cor_evap;
        dP_cor = constant.dP_cor_evap;
    elseif Diab == 3 % Condenser
        f_cor = constant.f_cor_cond;
        dP_cor = constant.dP_cor_cond;
    elseif Diab == 2 % Heat Exchanger
        if x(end)>x(1) % Effectively an evaporator
            f_cor = constant.f_cor_evap;
            dP_cor = constant.dP_cor_evap;
        else % Assuming condensing flow
            f_cor = constant.f_cor_cond;
            dP_cor = constant.dP_cor_cond;
        end
    end
    else
        Diab
        error('Diab unknown/incorrect')
    end

    u_ls=m.*(1-x)/(rho_l*Ac); % Superficial liquid velocity
    u_vs=m.*x/(rho_v*Ac); % Superficial gas velocity
    u_lo=m./(rho_l*Ac); % 'liquid-only' velocity
    u_vo=m./(rho_v*Ac); % 'gas-only' velocity

    Re_ls=rho_l*u_ls*d/mu_l;
    Re_vs=rho_v*u_vs*d/mu_v;

    Re_lo = m*d/(Ac*mu_l);
    Re_vo = m*d/(Ac*mu_v);

%% Single-phase friction correlations
% Laminar flow
f_l_laminar=64./Re_ls;
f_v_laminar=64./Re_vs;
f_lo_laminar=64./Re_lo;
f_vo_laminar=64./Re_vo;

switch f_cor
    case 1
        f_l_turbulent = Haaland(e, d, Re_ls);
        f_v_turbulent = Haaland(e, d, Re_vs);
        f_lo_turbulent = Haaland(e, d, Re_lo);
        f_vo_turbulent = Haaland(e, d, Re_vo);
    case 2
        f_l_turbulent = Blasius(Re_ls);
        f_v_turbulent = Blasius(Re_vs);
        f_lo_turbulent = Blasius(Re_lo);
        f_vo_turbulent = Blasius(Re_vo);
end

```

```

case 3
    f_l_turbulent = Fang(Re_ls);
    f_v_turbulent = Fang(Re_vs);
    f_lo_turbulent = Fang(Re_lo);
    f_vo_turbulent = Fang(Re_vo);
case 4
    f_l_turbulent = Fang2(e, d, Re_ls);
    f_v_turbulent = Fang2(e, d, Re_vs);
    f_lo_turbulent = Fang2(e, d, Re_lo);
    f_vo_turbulent = Fang2(e, d, Re_vo);
case 5
    f_l_turbulent = Blasius(Re_ls);
    f_v_turbulent = Blasius(Re_vs);
    f_lo_turbulent = Blasius(Re_lo);
    f_vo_turbulent = Blasius(Re_vo);
    % find the high-Re numbers
    ind_Re_ls = find(Re_ls >= 20000);
    ind_Re_vs = find(Re_vs >= 20000);
    ind_Re_lo = find(Re_lo >= 20000);
    ind_Re_vo = find(Re_vo >= 20000);
    f_l_turbulent(ind_Re_ls) = Incro(Re_ls(ind_Re_ls));
    f_v_turbulent(ind_Re_vs) = Incro(Re_vs(ind_Re_vs));
    f_lo_turbulent(ind_Re_lo) = Incro(Re_lo(ind_Re_lo));
    f_vo_turbulent(ind_Re_vo) = Incro(Re_vo(ind_Re_vo));
end

%f = Incro(Re) %for high reynolds numbers...

smooth_l = 1./(1+exp(-(Re_ls - 2400)/450)); % smoothing function
smooth_v = 1./(1+exp(-(Re_vs - 2400)/450));
smooth_lo = 1./(1+exp(-(Re_lo - 2400)/450)); % smoothing function
smooth_vo = 1./(1+exp(-(Re_vo - 2400)/450));

f_l = (1-smooth_l).*f_l_laminar + smooth_l.*f_l_turbulent;
f_v = (1-smooth_v).*f_v_laminar + smooth_v.*f_v_turbulent;
f_lo = (1-smooth_lo).*f_lo_laminar + smooth_lo.*f_lo_turbulent;
f_vo = (1-smooth_vo).*f_vo_laminar + smooth_vo.*f_vo_turbulent;

dPdx_l=f_l*rho_l.*u_ls.^2/d/2;
dPdx_v=f_v*rho_v.*u_vs.^2/d/2;
dPdx_lo=f_lo*rho_l.*u_lo.^2/d/2;
dPdx_vo=f_vo*rho_v.*u_vo.^2/d/2;

dPdx_fric = dPdx_lo_sf;
%% Two-phase pressure drop calculations
Xtreshhold=1e-3; % Threshold for determining if coolant is considered fully liquid, or two-phase
ind_tf=find(x>=Xtreshhold);
if isempty(ind_tf)
    switch dP_cor
        case 1 % Muller-Steinhagen & Heck
            dPdx_fric(ind_tf) = MSH(dPdx_l(ind_tf),dPdx_v(ind_tf),x(ind_tf));
        case 2 % Friedel
            dPdx_fric(ind_tf) = Friedel(dPdx_lo(ind_tf),rho_l,rho_v,mu_l,mu_v,f_lo(ind_tf),f_vo(ind_tf));
        case 3 % Kim & Mudawar
            dPdx_fric(ind_tf) = KM(Re_ls(ind_tf),Re_vs(ind_tf),dPdx_l(ind_tf),dPdx_v(ind_tf),Re_lo(ind_tf));
        case 4 % Lockhart & Martinelli
            dPdx_fric(ind_tf) = LM(Re_ls(ind_tf),Re_vs(ind_tf),dPdx_l(ind_tf),dPdx_v(ind_tf));
        case 5 % Xu & Fang
            dPdx_fric(ind_tf) = XF(dPdx_lo(ind_tf),dPdx_vo(ind_tf),m(ind_tf),Ac,d,rho_l,rho_v,sig,Re_l);
    end
end
end

dPdx_fric=max(dPdx_fric,0);
dP_fric=cumsum(dPdx_fric);
dP_fric=dP_fric*L/NE*1.0;

end

%% Friction factor correlations

```

```

% Haaland
function f = Haaland(e, d, Re)
f = (-1.8*log10((e/d/3.7)^1.11+6.9./Re)).^(-2);
end
% Blasius
function f = Blasius(Re)
f = 0.3164./(Re.^0.25);
end
% Fang, Xu, Zhou (smooth pipes)
function f = Fang(Re)
f = 0.25.*(log10(150.39./(Re.^0.98865)) - 152.66./Re)).^(-2);
end
% Fang, Xu, Zhou (rough pipes)
function f = Fang2(rough, d, Re)
f = 1.613.*(log(0.234.*(rough./d).^1.1007) - 60.525./(Re.^1.1105)) + 56.291./(Re.^1.0712))).^(-2);
end
% High reynolds number (>20,000) from Incropera & DeWitt
function f = Incro(Re)
f = 0.184.*Re.^(-0.2);
end

%% Two-phase frictional pressure drop correlations

% Muller-Steinhagen & Heck
function dPdx = MSH(dPdx_l,dPdx_v,x)
A=dPdx_l;
B=dPdx_v;
G=A+2*(B-A).*x;
dPdx=G.*(1-x).^1/3+B.*x.^3;
end

%Friedel
function dPdx = Friedel(dPdx_lo,rho_l,rho_v,mu_l,mu_v,f_lo,f_vo,sig,x,g,d,m,Ac)
A=(1-x.^2)+x.^2.*rho_l.*f_vo./(rho_v.*f_lo);
B=x.^0.78.*(1-x).^0.224;
C=(rho_l./rho_v).^0.91.*(mu_v./mu_l).^0.19.*(1-mu_v./mu_l).^0.7;

G=m/Ac;
rho_h=rho_v.*rho_l./(rho_l.*x+(1-x).*rho_v);
Fr_lh=G.^2./(g.*d.*rho_h.^2);
We_lh=d.*G.^2./(rho_h.*sig);

dPdx=dPdx_lo.*(A+3.24.*B.*C./(Fr_lh.^0.045).*We_lh.^0.035));
end

% Kim & Mudawar adiabatic & condensing flow (mini-and micro-channels)
function dPdx = KM(Re_l,Re_v,dPdx_l,dPdx_v,Re_lo,Re_vo,sig,m,Ac,As,d,rho_l,rho_v,Diab,x,P,Hlv)
G=m/Ac;

We_vo=d.*G.^2./(rho_v.*sig);
Su_vo=We_vo/(Re_vo.^2);

ind_lowRe_l=find(Re_l<2500); ind_lowRe_v=find(Re_v<2500);
temp=zeros(1,length(Re_l));
temp(ind_lowRe_l)=1;
temp(ind_lowRe_v)=temp(ind_lowRe_v)+2;
ind_vv=find(temp==3);
ind_tv=find(temp==2);
ind_vt=find(temp==1);
ind_tt=find(temp==0);

Cf=zeros(1,length(Re_l));
Cf(ind_vv)=3.5e-5*Re_lo(ind_vv).^0.44*Su_vo^0.5*(rho_l/rho_v)^0.48;
Cf(ind_tv)=8.7e-4*Re_lo(ind_tv).^0.17*Su_vo^0.5*(rho_l/rho_v)^0.14;
Cf(ind_vt)=0.0015*Re_lo(ind_vt).^0.59*Su_vo^0.19*(rho_l/rho_v)^0.36;
Cf(ind_tt)=0.39*Re_lo(ind_tt).^0.03*Su_vo^0.10*(rho_l/rho_v)^0.35;

% Evaporators
if Diab == 1
    %Required values:

```

```

We_lh = d*(G.*(1-x)).^2/(rho_l*sig);
qfl = P/As*length(x); % (W/m2) heat flux
Bo = (qfl/G/Hlv); % Boiling number; % q''/(Gh_lat)
wet_frac = 1; % Wetted area/total area

Cf = Cf.*(1+60.*We_lh.^0.32).*(Bo.*wet_frac).^0.78);

if isempty(ind_lowRe_l)
    Cf(ind_lowRe_l) = Cf(ind_lowRe_l).*(1+530.*We_lh(ind_lowRe_l).^0.52).*(Bo(ind_lowRe_l).*wet_
end
end

X = sqrt(dPdx_l./dPdx_v);
dPdx = dPdx_l.*(1+Cf./X + 1./(X.^2));
end

% Lockhart & Martinelli
function dPdx = LM(Re_l,Re_v,dPdx_l,dPdx_v)
ind_lowRe_l=Re_l<2500;
ind_lowRe_v=Re_v<2500;
temp = ind_lowRe_l+2*ind_lowRe_v;
ind_vv=temp==3;
ind_tv=temp==2;
ind_vt=temp==1;
ind_tt=temp==0;

Cf = 5*ind_vv + 10*ind_tv + 12*ind_vt+20*ind_tt;

X = sqrt(dPdx_l./dPdx_v);
dPdx = dPdx_l.*(1+Cf./X + 1./(X.^2));
end

% Xu & Fang
function dPdx = XF(dPdx_lo,dPdx_vo,m,Ac,d,rho_l,rho_v,sig,Re_lo,Re_vo,x,Diab,g)

X_var = sqrt(dPdx_lo./dPdx_vo);

G = m/Ac;

if (Diab == 1) || ((Diab == 2) && (x(end)>x(1))) %(evaporating flows)
    We_lo = d.*G.^2./(rho_l.*sig);
    Su_lo = We_lo./(Re_lo.^2);

    A = X_var.^2).*x.^3 + (1-x).^1/3).*(1+2.*x.*(X_var.^2)-1));
    B = (1+1.54.*sqrt(1-x).*Su_lo.^1.47));

    dPdx = dPdx_lo.*A.*B;

elseif (Diab == 3) || ((Diab == 2) && (x(end)<=x(1))) %(condensing flows)
    rho_h = rho_v.*rho_l./(rho_l.*x + (1-x).*rho_v);
    Fr_lh = G.^2./(g.*d.*rho_h.^2);
    We_lh = d.*G.^2./(rho_h.*sig);
    C = 1 + 2*x.^1.17).*(X_var.^2)-1) + 0.00775.*x.^(-0.475).*Fr_lh.^0.535).*We_lh.^0.188);

    dPdx = dPdx_lo.*(X_var.^2).*x.^3 + C.*(1-x.^2.59)).^(0.632));
else
    error('Incorrect friction factor used')
end
end
end

```

D

Sensitivity analysis

At the end of the validation phase, a start was made on the sensitivity analysis. A true sensitivity analysis involves running the model for a large number of times to map the regression and behaviour of the results when small uncertainties in the inputs are introduced. Since each of the simulation runs takes approximately 2 hours, it would be extremely computationally expensive to do this. There was not enough time to run these simulations and properly evaluate the results during the project, therefore this is left as a recommendation for future work. The two short tests that were performed could not be considered a true sensitivity analysis and it was therefore decided that they should therefore not be presented as such in the main thesis, but presented in this appendix instead.

D.1. Pipe roughness

The pipe roughness values for this setup were based on the standard assumption within the NLR lab of $1\ \mu\text{m}$. Figure D.1 shows what happens if the roughness throughout the system would be doubled or even increased by a factor of magnitude to $10\ \mu\text{m}$. Note that this only affects the Xu & Fang and Kim & Mudawar frictional pressure drop equations. None of the other equations make use of this parameter. The Xu & Fang correlation ran into negative flow errors at the tenfold increase simulation.

Apparently, the effects of small changes in roughness is very minimal. Moreover, increasing the pipe roughness by a factor ten brings the Kim & Mudawar correlation to a MAPE of 28.42%. Which is just within the required error boundary of 30% but still significantly lower performance than the Friedel and Lockhart & Martinelli correlations. Thus, incorrect assumptions about the pipe roughness are definitively not the cause of the under-performance of these two correlations.

D.2. Pipe diameter

Another test was done to check the effect of changes in pipe diameter. Since the total pressure drop was under-predicted by many of the correlations, as discussed in chapter 8.2, a hypothesis was formed that this might be caused by some uncertainty in the pipe diameter. If the pipes are slightly narrower than was initially expected, this will lead to increased pressure drops, potentially explaining the under-predictions seen in the model. To tests this hypothesis, the diameter of all components was decreased by 10% in the numerical model.

The results for the Friedel and Kim & Mudawar pressure drop correlations are shown in figure D.2. As expected, the diameter has a significant effect on the pressure drop, as evidenced by the big change in the results. However, even with a 10 % smaller diameter, which falls way outside any realistic uncertainty margin on the tubing, the Kim & Mudawar still under-predicts the pressure drop. Thus the under-performance of these correlation is not due to an error in the tubing diameter and has to have an other cause.

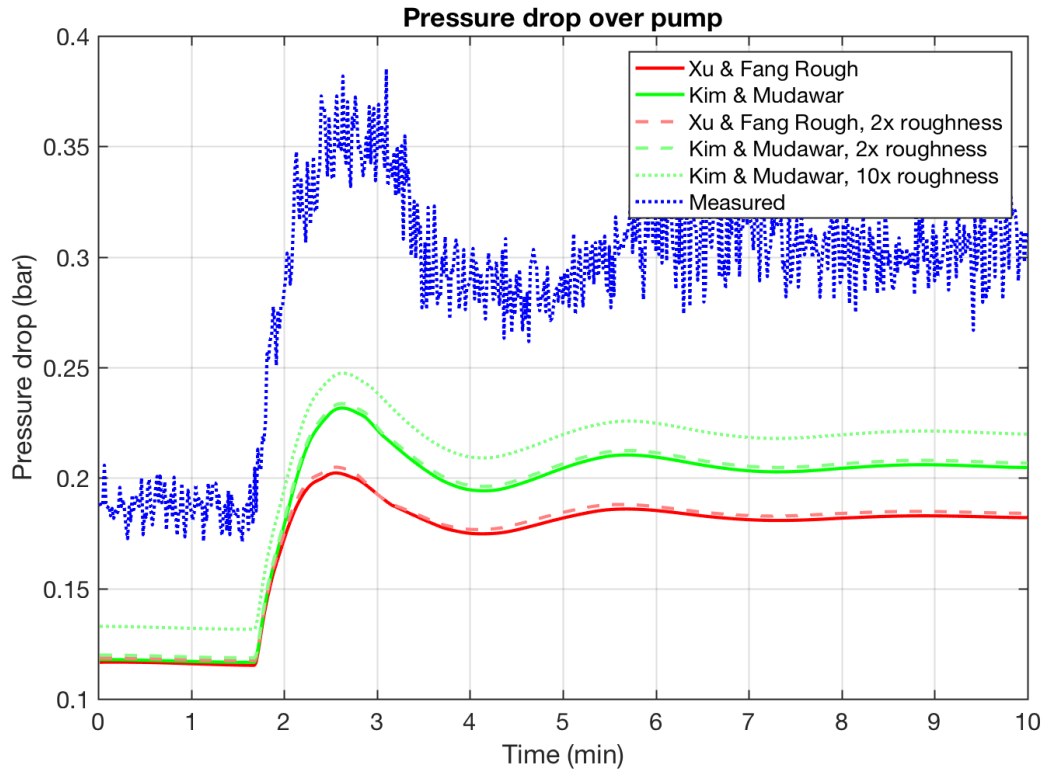


Figure D.1: Sensitivity of pressure drop prediction to changes in pipe roughness: doubled roughness

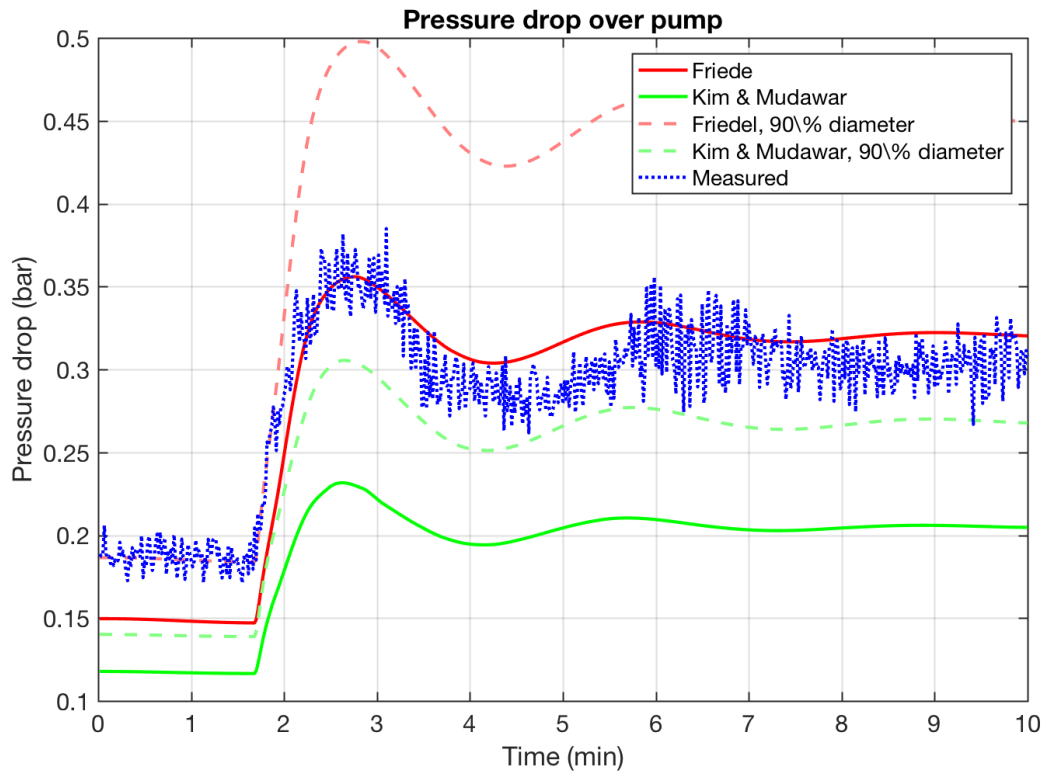
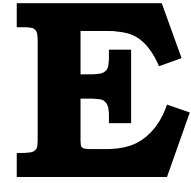
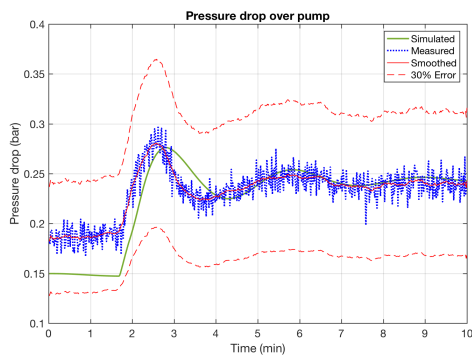


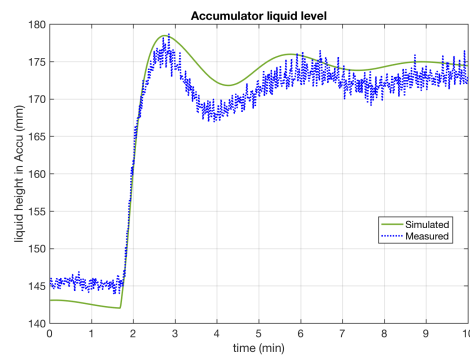
Figure D.2: Sensitivity to changes in pipe diameter: 10% smaller



Final correlation validation

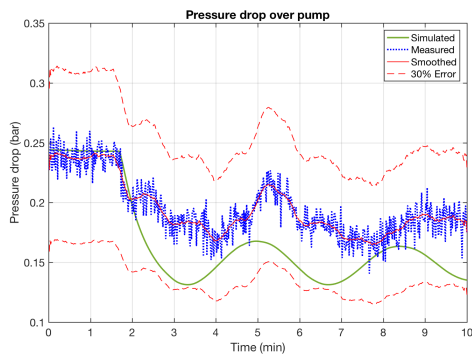


(a) Total pressure drop

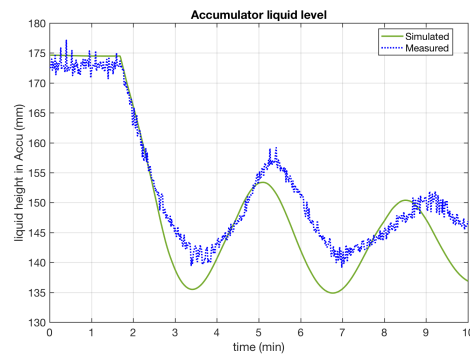


(b) Accumulator liquid height

Figure E.1: From 300 to 900 [W] evaporator power

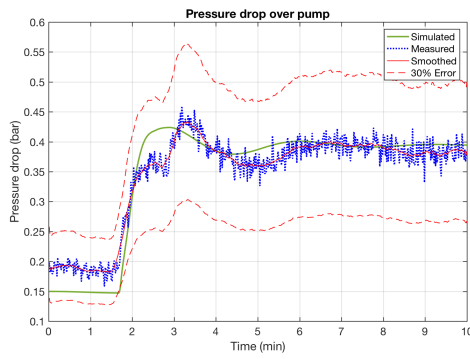


(a) Total pressure drop

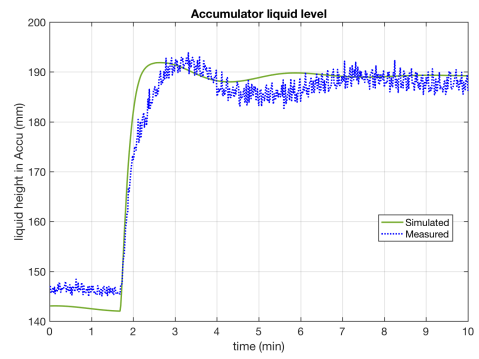


(b) Accumulator liquid height

Figure E.2: From 900 to 300 [W] evaporator power

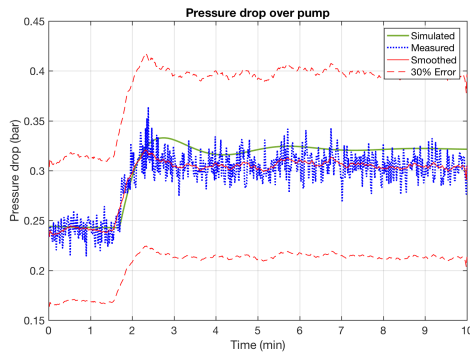


(a) Total pressure drop

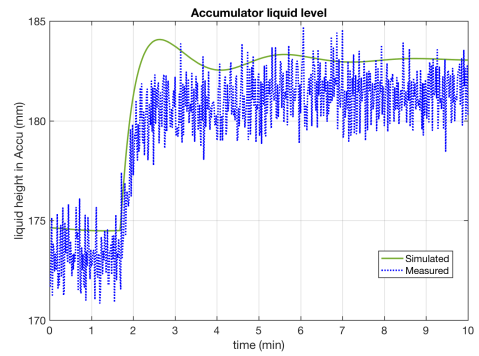


(b) Accumulator liquid height

Figure E.3: From 300 to 2100 [W] evaporator power

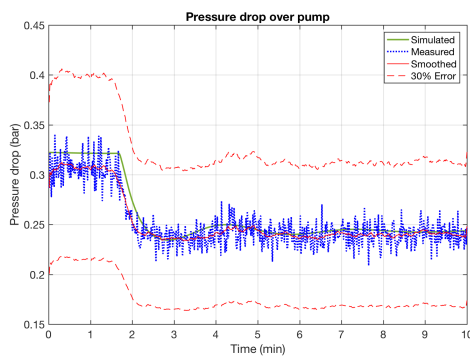


(a) Total pressure drop

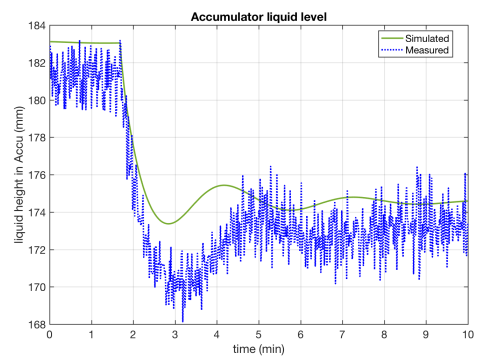


(b) Accumulator liquid height

Figure E.4: From 900 to 1500 [W] evaporator power

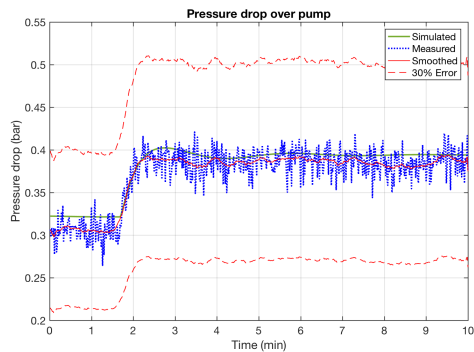


(a) Total pressure drop

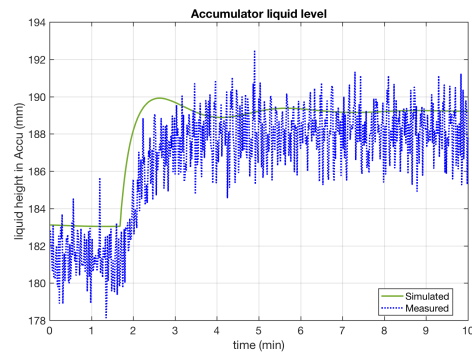


(b) Accumulator liquid height

Figure E.5: From 1500 to 900 [W] evaporator power

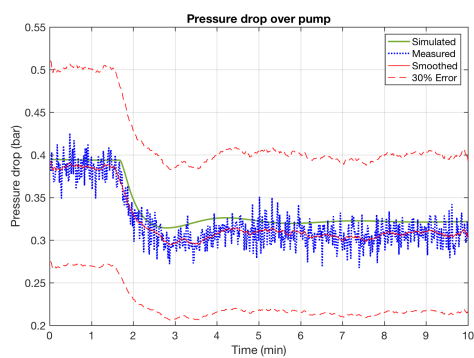


(a) Total pressure drop

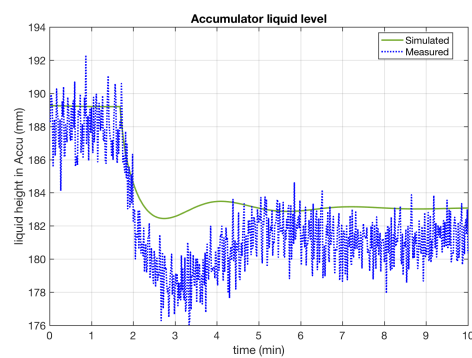


(b) Accumulator liquid height

Figure E.6: From 1500 to 2100 [W] evaporator power



(a) Total pressure drop



(b) Accumulator liquid height

Figure E.7: From 2100 to 1500 [W] evaporator power

Bibliography

- [1] L. Friedel, *Improved friction pressure drop correlation for horizontal and vertical two phase pipe flow*, in *European Two Phase Flow Group Meeting, Paper 18* (Ispra, Italy, 1979) p. 485–492.
- [2] K. Gungor and R. Winterton, *Simplified general correlation for saturated flow boiling and comparisons of correlations with data*, *The Canadian Journal of Chemical Engineering* **65**, 148 (1987).
- [3] S. M. Kim and I. Mudawar, *Universal approach to predicting two-phase frictional pressure drop for adiabatic and condensing mini/micro-channel flow*, *International Journal of Heat and Mass Transfer* **55**, 3246 (2012).
- [4] R. Bolder, *The complex correlations of two-phase flows*, (2016), literature study, Master thesis, Delft University of Technology.
- [5] H. J. van Gerner, *Time dependent behaviour of pumped two-phase cooling systems, experiments and simulations*, in *27th European Space Thermal Analysis Workshop* (ESA/ESTEC, Noordwijk, The Netherlands, 2013).
- [6] F. P. Incropera, D. P. DeWitt, T. L. Bergman, and A. S. Lavine, *Fundamentals of Heat and Mass transfer*, 6th ed. (John Wiley & Sons, 2007).
- [7] H. S. E., *Simple and explicit formulas for the friction factor in turbulent pipe flow*, *Journal of Fluids Engineering* **105**, 89 (1983).
- [8] J. Terpstra, *Modeling a two-phase mechanically pumped loop*, Internship Report (NLR, Netherlands Aerospace Centre, Marknesse, The Netherlands, 2015).
- [9] Y. Xu and X. Fang, *A new correlation of two-phase frictional pressure drop for evaporating flow in pipes*, *International journal of refrigeration* **35**, 2039 (2012).
- [10] X. Fang, Y. Xu, and Z. Zhou, *New correlations of single-phase friction factor for turbulent pipe flow and evaluation of existing single-phase friction factor correlations*, *Nuclear Engineering and Design* **241**, 897 (2011).
- [11] H. Muller-Steinhagen and K. Heck, *A simple friction pressure drop correlation for two-phase flow in pipes*, *Chemical Engineering and Processing* **20**, 297 (1986).
- [12] H. Blasius, *Das Ähnlichkeitsgesetz bei reibungsvorgängen in flüssigkeiten*, *Forsch. Gebiete Ingenieurw.* (1913).
- [13] R. W. Lockhart and R. C. Martinelli, *Proposed correlation of data for isothermal two-phase, two-component flow in pipes*, *Chemical Engineering Progress* **45**, 39 (1949).
- [14] V. Gnielinski, *New equations for heat and mass transfer in turbulent pipe and channel flow*, *Int Chem Eng* **16**, 359–368 (1976).
- [15] X. Fang, *A new correlation of flow boiling heat transfer coefficients based on R134a data*, *International Journal of Heat and Mass Transfer* **66**, 279 (2013).
- [16] S. M. Kim and I. Mudawar, *Universal approach to predicting saturated flow boiling heat transfer in mini/micro-channels - part I. dryout incipience quality*, *International Journal of Heat and Mass Transfer* **64**, 1226 (2013).
- [17] S. M. Kim and I. Mudawar, *Universal approach to predicting saturated flow boiling heat transfer in mini/micro-channels - part II. two-phase heat transfer coefficient*, *International Journal of Heat and Mass Transfer* **64**, 1239 (2013).

- [18] M. A. Woldesemayat and A. J. Ghajar, *Comparison of void fraction correlations for different flow patterns in horizontal and upward inclined pipes*, *International Journal of Multiphase Flow* **33**, 347 (2007).
- [19] H. J. van Gerner and N. Braaksma, *Transient modelling of pumped two-phase cooling systems: Comparison between experiment and simulation*, in *46th International Conference on Environmental Systems* (46th International Conference on Environmental Systems, Vienna, Austria, 2016).
- [20] L. Zhao and K. Rezkallah, *Pressure drop in gas-liquid flow at microgravity conditions*, *International Journal of Multiphase Flow* **21**, 837 (1995).
- [21] S. M. Zivi, *Estimation of steady-state steam void-fraction by means of the principle of minimum entropy production*, *Journal of Heat Transfer* **86**, 247 (1964).
- [22] C. J. Baroczy, *A systematic correlation for two-phase pressure drop*, in *Chemical Engineering Progress symposium series No. 64* (1966) pp. 232–249.
- [23] D. Butterworth, *A comparison of some void fraction relationships for gas-liquid flow*, *International Journal of Multiphase Flow* **1**, 845 (1975).
- [24] S. L. Smith, *Void fractions in two-phase flow: a correlation based upon an equal velocity head model*, *Proceedings of the Institution of Mechanical Engineers* **36**, 647– (1969).
- [25] S. Z. Rouhani and E. Axelsson, *Calculation of void volume fraction in the subcooled and quality boiling regions*, *International Journal of Heat and Mass transfer* **1**, 383 (1970).
- [26] S. M. Kim and I. Mudawar, *Universal approach to predicting two-phase frictional pressure drop for mini/micro-channel saturated flow boiling*, *International Journal of Heat and Mass Transfer* **58**, 718 (2013).
- [27] H. J. van Gerner, *Dynamic model for two-phase mechanically pumped fluid loops*, Tech. Rep. (NLR, Netherlands Aerospace Centre, Marknesse, The Netherlands, 2011).
- [28] H. J. van Gerner, *Dynamic model for two-phase mechanically pumped fluid loops*, Confidential Report (NLR, Netherlands Aerospace Centre, Marknesse, The Netherlands, 2011).
- [29] E. W. Lemmon, M. L. Huber, and M. O. McLinden, *NIST Standard Reference Database 23: Reference Fluid Thermodynamic and Transport Properties - REFPROP*, National Institute of Standards and Technology, Standard Reference Data Program, Boulder, Colorado, 9th ed. (2010).
- [30] N. Braaksma, *An experimental/numerical investigation on the transient behavior of two-phase cooling systems*, mthesis (NLR, ASML, Universiteit Twente, Marknesse, The Netherlands, 2013).
- [31] Y. A. Çengel, *Fundamentals of thermal-fluid Sciences* (McGraw-Hill, New York, 2012).
- [32] Y. Xu and X. Fang, *A new correlation of two-phase frictional pressure drop for condensing flow in pipes*, *Nuclear Engineering and Design* **263**, 87 (2013).
- [33] *Swagelok catalog: Sample cylinders, accessories, and outage tubes*, (Swagelok Company, USA 2017), Accessed 13/02/2017, <https://www.swagelok.com/downloads/WebCatalogs/EN/MS-01-177.pdf>.
- [34] *Lytron website*, (Lytron Inc., Woburn, MA, USA 2017), Accessed 19/09/2017, <http://www.lytron.com/Cold-Plates/Standard/Cold-Plates-Performance-Fin>.